



**HAL**  
open science

# Design of Coded Modulation Schemes Based on Non-Binary LDPC Codes

Asma Maalaoui

► **To cite this version:**

Asma Maalaoui. Design of Coded Modulation Schemes Based on Non-Binary LDPC Codes. Other [cs.OH]. Institut National Polytechnique de Toulouse - INPT, 2023. English. NNT : 2023INPT0044 . tel-04207433

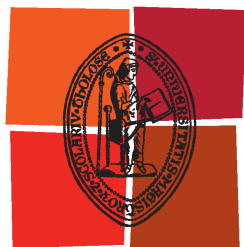
**HAL Id: tel-04207433**

**<https://theses.hal.science/tel-04207433>**

Submitted on 14 Sep 2023

**HAL** is a multi-disciplinary open access archive for the deposit and dissemination of scientific research documents, whether they are published or not. The documents may come from teaching and research institutions in France or abroad, or from public or private research centers.

L'archive ouverte pluridisciplinaire **HAL**, est destinée au dépôt et à la diffusion de documents scientifiques de niveau recherche, publiés ou non, émanant des établissements d'enseignement et de recherche français ou étrangers, des laboratoires publics ou privés.



Université  
de Toulouse

# THÈSE

En vue de l'obtention du

## DOCTORAT DE L'UNIVERSITÉ DE TOULOUSE

**Délivré par :**

Institut National Polytechnique de Toulouse (Toulouse INP)

**Discipline ou spécialité :**

Informatique et Télécommunication

---

**Présentée et soutenue par :**

Mme ASMA MAALAOUI

le vendredi 14 avril 2023

**Titre :**

Conception de schémas de modulation codés basés sur des codes LDPC  
non binaires

---

**École doctorale :**

Mathématiques, Informatique, Télécommunications de Toulouse (MITT)

**Unité de recherche :**

Institut de Recherche en Informatique de Toulouse (IRIT)

**Directeur de Thèse :**

M. CHARLY POUILLIAT

**Rapporteurs :**

M. FREDERIC GUILLOUD, IMT ATLANTIQUE

M. JEAN-PIERRE CANCES, UNIVERSITE DE LIMOGES

**Membres du jury :**

M. EMMANUEL BOUTILLON, UNIVERSITE DE BRETAGNE SUD, Président

M. CHARLY POUILLIAT, TOULOUSE INP, Membre

M. CHRISTOPHE JEGO, UNIVERSITÉ DE BORDEAUX, Membre

MME IRYNA ANDRIYANOVA, UNIVERSITE DE CERGY-PONTOISE, Membre



*“Daughter, never fall before receiving the blow...”*

Youssef Maalaoui, a loving father



# Abstract

This thesis addresses the coded modulation (CM) scheme based on quadrature amplitude modulation (QAM) signaling and low-density parity-check (LDPC) channel coding. It also focuses on time-invariant non-uniform signaling in combination with probabilistic amplitude shaping (PAS) and circular QAM (CQAM) modulations.

First, the thesis describes the main transmission components from the transmitter to the receiver over the physical channel. Then, some notions used as metrics for performance evaluation are analyzed, and we typically note the mutual information (MI). Also, relevant background materials on shaping techniques and LDPC codes are presented.

Second, the thesis focuses on optical networks' polarization-dependent loss (PDL) channels. Two previous precoding techniques, SB and NSB, are revised and analyzed for the CM and bit-interleaved CM (BICM) capacities. We also investigate the combination of the precoded PDL channel and probabilistic shaping (PS) encoding to enhance the system's performance. Furthermore, two new approaches based on non-binary information processing have been tested; the design of protograph non-binary codes under the NSB framework and the creation of a symbol interleaved CM (SICM) based on non-binary protograph LDPC codes.

Then, the thesis analyses existing geometric shaping (GS) schemes on the complex plane. We propose the construction of  $(c, p)$  CQAM constellations with equiprobable signaling that can approach the Gaussian capacity. In addition, we design simple non-binary protograph LDPC codes for GS constellations to show that we can operate close to the channel capacity. Finally, deploying the new CQAM constellations design, we offer how to combine non-binary LDPC codes with PAS. Compared to uniform signaling, significant performance gains are achieved on the AWGN channel for short block lengths.



# Résumé

Cette thèse aborde le schéma de modulation codée (CM) basé sur la signalisation de modulation d'amplitude en quadrature (QAM) et le codage de canal à contrôle de parité à faible densité (LDPC). Il se concentre également sur la signalisation non uniforme invariante dans le temps en combinaison avec la mise en forme d'amplitude probabiliste (PAS) et les modulations QAM circulaires (CQAM).

Tout d'abord, la thèse décrit les principaux composants de transmission de l'émetteur au récepteur sur le canal physique. Ensuite, certaines notions utilisées comme métriques pour l'évaluation des performances sont analysées, et on note typiquement l'information mutuelle (IM). En outre, des documents de référence pertinents sur les techniques de mise en forme et les codes LDPC sont présentés.

Deuxièmement, la thèse porte sur les canaux de perte dépendant de la polarisation (PDL) des réseaux optiques. Deux techniques de précodage précédentes, SB et NSB, sont révisées et analysées pour les capacités CM et CM entrelacées de bits (BICM). Nous étudions également la combinaison du canal PDL précodé et du codage de mise en forme probabiliste (PS) pour améliorer les performances du système. Par ailleurs, deux nouvelles approches basées sur le traitement de l'information non binaire ont été testées ; la conception de codes protographes non binaires dans le cadre du NSB et la création d'un CM entrelacé de symboles (SICM) basé sur des codes LDPC protographes non binaires.

Ensuite, la thèse analyse les schémas de mise en forme géométrique (GS) existants sur le plan complexe. Nous proposons la construction de constellations CQAM  $(c, p)$  avec une signalisation équiprobable pouvant approcher la capacité gaussienne. De plus, nous concevons des codes LDPC de protographe non binaires simples pour les constellations GS afin de montrer que nous pouvons opérer à proximité de la capacité du canal. Enfin, en déployant la nouvelle conception des constellations CQAM, nous proposons comment combiner des codes LDPC non binaires avec PAS. Par rapport à la signalisation uniforme, des gains de performances significatifs sont obtenus sur le canal AWGN pour les longueurs de bloc courtes.



# Acknowledgements

Avant d'orienter les audacieux lecteurs et lectrices à travers les dédales de mon manuscrit, je désire magnifier l'image d'une scientifique solitaire en l'entourant d'un éventail précieux et diversifié de soutiens. Je souhaite exprimer ma gratitude envers les personnes qui persévèrent dans les replis de ma mémoire pendant ces années de thèse, ainsi qu'envers celles qui continueront d'être présentes pour les chapitres à venir. Je suis parfaitement consciente d'avoir mené à bien une thèse dans une discipline offrant des conditions de travail confortables. Aussi, je tiens à exprimer mes sincères remerciements aux membres distingués de mon jury de thèse. Leur intérêt évident pour mon manuscrit, témoigné par leurs multiples questions pertinentes lors de la soutenance, est grandement apprécié.

Du fond du cœur, je tiens à remercier mon directeur de thèse, Charly, pour l'honneur qu'il m'a fait en me permettant de travailler à ses côtés. Merci pour ton soutien inestimable et tes précieux conseils qui ont été des piliers essentiels tout au long de ma thèse. Nous avons partagé des heures de réunions intenses, rentrant tard dans la nuit pour discuter et approfondir nos idées. Ton encouragement indéfectible lorsque je me sentais épuisée et accablée par le stress a été d'une valeur inestimable. Chaque échange avec toi était pour mon propre bien et m'a permis de grandir en tant que chercheur. Nous avons traversé ensemble des périodes éprouvantes où le sommeil était rare, mais je suis reconnaissante d'avoir pu compter sur ta présence et ton soutien constant, en particulier pendant la période difficile de la pandémie de COVID-19. Tu m'as régulièrement appelée pour t'assurer que j'allais bien, ce qui m'a apporté un réconfort immense. En somme, je suis profondément reconnaissante envers toi pour ta présence, ton soutien inconditionnel et tes conseils éclairés tout au long de ce parcours de recherche.

Je tiens à prendre un moment pour exprimer toute ma gratitude à mon père Youssef et ma mère Latifa et leur remercier du fond du cœur pour tout ce qu'ils ont fait pour moi, qui m'a permis d'atteindre ce stade important de ma vie. Leurs sacrifices, leur amour inconditionnel et leur soutien constant ont été les piliers solides sur lesquels j'ai pu construire mon parcours jusqu'à cette thèse. Je

suis fière d'avoir des parents comme vous à mes côtés. Votre dévouement, votre soutien indéfectible et votre encouragement m'ont donné la confiance nécessaire pour poursuivre mes rêves et atteindre mes objectifs. Vos aspirations et vos espoirs se sont entrelacés avec les miens, et chaque réussite que j'obtiens est également la vôtre. Votre amour et vos sacrifices ont forgé la personne que je suis aujourd'hui, et je vous suis infiniment reconnaissante pour cela. J'espère sincèrement que cette thèse vous rendra fiers.

Youssef, j'imagine tes paroles d'encouragement à chaque pas que je fais. Ta sagesse continue à m'inspirer et à guider mes choix. Tu es et resteras toujours mon super-héros, et je suis fière d'être ta fille « l3ssal » comme tu m'appelais affectueusement. Ya, tu es une force incroyable dans ma vie. Ta patience infinie, ta tendresse et ta compréhension ont été des piliers essentiels qui ont apaisé mes inquiétudes et allégé mon stress. Tu es plus qu'une mère pour moi, tu es aussi mon amie. Je vous aime profondément, et je suis honorée d'avoir les meilleurs parents du monde. Cette thèse est le fruit de notre collaboration et de notre dévouement collectif. Merci du plus profond de mon cœur.

Je souhaite aussi exprimer ma profonde gratitude à mes frères Bachar, Hamma, Welten et Zaair, pour leur soutien indéfectible et leurs blagues qui ont égayé mon parcours de recherche. Pour moi, vous êtes mes lions qui me donnent la force et le courage d'avancer. Je veux également remercier ma sœur Manel pour son soutien incommensurable et ses conseils inestimables. Tu es la personne qui me connaît le mieux dans la vie, et je suis extrêmement reconnaissante d'avoir une sœur aussi exceptionnelle que toi à mes côtés. Un petit remerciement spécial à mes adorables nièces Saroura, Yakouna et Joujou. Votre présence dans ma vie apporte tant de joie et d'amour. Je suis tellement chanceuse de vous avoir comme nièces et de voir grandir des petites merveilles comme vous.

Cher fiancé, je tiens à t'exprimer ma profonde gratitude et à te dédier ce remerciement empreint d'un amour indescriptible. Tu as été bien plus qu'un soutien constant, tu es l'essence même de mon inspiration. À chaque pas que j'ai franchi, tu étais là pour me soutenir et croire en moi. Ta présence inébranlable a été ma force, et ta patience infinie face à mon stress en dit long sur ton amour inconditionnel. Les nuits blanches que nous avons partagées, où tu t'es privé de sommeil pour être à mes côtés, témoignent de ton dévouement et de ton amour sans limites. Tu as été mon pilier dans les moments de doute et de fatigue, et je suis éternellement reconnaissante de ta présence rassurante. Les aventures que nous avons vécues pendant ces années de thèse resteront à jamais gravées dans ma mémoire comme des moments de folie et de complicité. Des

instants où nous avons ri aux éclats, exploré de nouveaux horizons et repoussé nos limites ensemble. Tu as su rendre cette période intense et mémorable. Je termine donc en te remerciant une fois de plus pour tout ce que tu as fait et pour l'amour profond que je ressens pour toi. Avec mon doctorat en poche, nous sommes fiers de dire haut et fort: "Crazy cat lady with a doctorate". C'est grâce à toi, à ton soutien inébranlable et à ton amour inégalé que j'ai pu atteindre ce niveau d'accomplissement. Habibi, mon amour pour toi est indescriptible, et chaque jour à tes côtés est une bénédiction. Je suis excitée et curieuse à l'idée des aventures et de la vie qui nous attendent encore ensemble.

Je souhaite remercier les permanents de l'équipe SC que j'ai pu côtoyer tout au long de ma thèse au laboratoire IRIT-N7. En particulier, j'aimerais adresser un merci spécial à André luc, responsable du site N7 de l'IRIT qui est une personne à la fois professionnelle et sympathique, et à Marie, une chef de l'équipe SC à la fois talentueuse dans sa capacité de leadership et créative. Je souhaite également remercier Cédric, Emmanuel, Marie Laure, Mathieu et Nicolas. Un merci tout particulier à Nathalie, qui a joué un rôle clé dans mon parcours d'enseignement. Merci, Nathalie, pour ton soutien constant et tes précieux enseignements. Je veux aussi exprimer ma gratitude spéciale envers Annabelle Sansus, ancienne secrétaire de l'équipe SC, ainsi que Vanessa Adjeroūd du secrétariat de l'équipe SC, et Sylvie Armengaud Metche (connue sous le nom de SAM) du secrétariat de l'équipe RMESS, pour leur gentillesse, leur accueil chaleureux et leur soutien constant tout au long de ces années de thèse.

Je souhaite également exprimer ma sincère gratitude envers les doctorants Arthur, Jocelyn et Leila, qui font partie de mon bureau. Leur soutien inestimable, nos discussions animées et nos moments de partage sur les joies et les difficultés de la thèse ont été d'une grande valeur pour moi. Je tiens également à remercier mes anciens co-bureaux, Sixin, Serdar et Dana, pour leur contribution et leur soutien précieux. Un merci spécial à Vinicius, mon ancien co-bureau et ami, pour son soutien inconditionnel, en particulier pendant la période difficile de la pandémie de COVID-19. Il a été à mes côtés tout au long de cette période. Merci cher ami brésilien pour tout ce que tu as fait pour moi. Je veux aussi exprimer ma profonde gratitude au chercheur Daniel ainsi qu'aux doctorants de l'équipe RMESS, Firmin, Mohamed, Justin, Fransisco, ainsi qu'à tous ceux et celles que j'oublie, pour leur amitié précieuse.

Je tiens à adresser mes remerciements les plus chaleureux à mon amie très chère, Amoul, qui a partagé avec moi la période de nos thèses. Amal, je suis infiniment reconnaissante pour les moments inoubliables que nous avons vécus

ensemble au laboratoire. Ta présence à mes côtés est d'une valeur inestimable, et notre amitié sincère est une source de soutien et de réconfort indéfectible. Je me considère extrêmement chanceuse de t'avoir dans ma vie, Amoul. Merci d'être cette amie exceptionnelle et précieuse qui a su rendre cette période de thèse encore plus spéciale. Je tiens également à te remercier pour les moments précieux que nous avons partagés, emplis d'humour et de complicité.

Je tiens à exprimer ma profonde gratitude envers mes amies les plus chères, Manou, Safa, et Jamoul. Je suis vraiment reconnaissante d'avoir chacune d'entre vous à mes côtés. Un merci spécial également à mes amies d'enfance Zohra et Mariem pour notre amitié qui traverse le temps. Votre présence dans ma vie est une bénédiction. Merci à toutes d'être des amies si merveilleuses. Un grand merci à Dhoudhou et Firas pour leur précieuse amitié.

Je tiens à exprimer ma profonde reconnaissance à une personne très chère à mon cœur, mon amie algérienne Ahlem. Si j'ai réussi à atteindre ce stade aujourd'hui, c'est grâce à ton soutien indéfectible et à ton précieux appui. Je t'adresse mes remerciements les plus sincères et du fond du cœur, ma chérie.

Je tiens aussi à exprimer ma profonde gratitude envers mes professeurs de l'école d'ingénieur, en particulier Messieurs Yahya et Ridha. Leur soutien indéfectible, leur précieuse aide et tout ce qu'ils ont fait à mes côtés ont grandement contribué à mon parcours académique et professionnel.

Un immense merci du fond du cœur à toutes les personnes qui ont semé une petite graine dans ma vie. Votre présence, votre soutien et votre influence ont eu un impact significatif et je vous en suis profondément reconnaissante.

# Contents

<b>Abstract</b>	<b>v</b>
<b>Résumé</b>	<b>vii</b>
<b>Acknowledgements</b>	<b>ix</b>
<b>1 Introduction</b>	<b>1</b>
<b>2 Fundamentals</b>	<b>7</b>
2.1 Coded Modulations: System Model . . . . .	7
2.1.1 System Model at the Emitter . . . . .	7
2.1.2 Transmission over Multiple Antennas . . . . .	9
2.1.3 Information Rate for Coded Modulations . . . . .	10
2.2 Geometric and Probabilistic Shaping . . . . .	12
2.2.1 Geometric Shaping . . . . .	13
2.2.2 Probabilistic Shaping . . . . .	14
PS Principle . . . . .	14
Probabilistic Amplitude Shaping (PAS) . . . . .	15
Non-uniform CCDM . . . . .	19
2.3 LDPC Codes . . . . .	19
2.3.1 Binary LDPC Codes . . . . .	19
2.3.2 Non-binary LDPC Codes . . . . .	21
2.3.3 Protograph-based LDPC Codes . . . . .	26
2.4 Asymptotic Analysis of LDPC Codes using EXIT Charts . . . . .	28
2.4.1 EXIT Charts for Unstructured Ensembles . . . . .	28
2.4.2 Protograph EXIT Charts for Structured Ensembles . . . . .	30
2.5 Application: SICM with Non-binary LDPC . . . . .	32
<b>3 Precoding and Non-binary Coding for Optical MIMO</b>	<b>37</b>
3.1 Introduction . . . . .	37
3.2 PDL Channel Model . . . . .	38
3.2.1 The Lumped PDL Channel . . . . .	38

3.2.2	The Spatially Balance Signalling . . . . .	39
3.2.3	The New Spatially Balance Signalling . . . . .	40
3.2.4	Zero Outage Capacity for DP and NSB . . . . .	42
3.3	Optimization over SB and NSB Schemes . . . . .	44
3.3.1	Worst BICM and SICM Optimization in the SB . . . . .	45
3.3.2	Worst BICM and SICM Optimization in the NSB . . . . .	48
3.4	Binary PAS for the Optical Channel . . . . .	52
3.5	Non-binary Coding for Optical MIMO . . . . .	55
3.5.1	CM Schemes . . . . .	56
3.5.2	BICM/SICM Schemes . . . . .	58
3.6	Conclusion . . . . .	60
<b>4</b>	<b>Circular QAM Signals and Non-binary Coding</b>	<b>61</b>
4.1	Introduction . . . . .	61
4.2	From Gaussian Shaping to CQAM Signals . . . . .	62
4.2.1	GS-QAM Signals . . . . .	62
4.2.2	GS-APSK Signals . . . . .	63
4.2.3	Achievable Capacities . . . . .	64
4.2.4	Link to Existing Shaping Strategies . . . . .	65
4.3	$(c, p)$ -Circular QAM Signals . . . . .	66
4.3.1	$(p, p)$ CQAM . . . . .	66
4.3.2	New $(c, p)$ -Circular QAM Signals . . . . .	67
4.3.3	Capacity Analysis . . . . .	70
4.4	Design of Non-binary Protograph Codes for Geometric Shaping	73
4.5	Conclusion . . . . .	74
<b>5</b>	<b>PAS with Non-binary LDPC Codes for CQAM Signals</b>	<b>77</b>
5.1	Introduction . . . . .	77
5.2	Preliminaries . . . . .	78
5.2.1	Distribution Matching . . . . .	78
5.2.2	Sphere Shaping . . . . .	78
5.2.3	Comparison: Finite Length Rate Loss . . . . .	79
5.3	PAS with Non-binary Codes for CQAM . . . . .	79
5.3.1	PS Performance . . . . .	81
5.3.2	CQAM with Non-binary Codes . . . . .	81
5.3.3	Coding Rates Equal To $\log_2 c / (\log_2 c + \log_2 p)$ . . . . .	82
5.3.4	Coding Rates Bigger Than $\log_2 c / (\log_2 c + \log_2 p)$ . . . . .	83
5.3.5	PAS Receiver . . . . .	84
5.4	Finite Length Simulations . . . . .	84

5.5 Conclusion . . . . .	87
<b>6 Conclusions and Perspectives</b>	<b>89</b>
<b>A Extended PAS for (c, p) CQAM</b>	<b>91</b>
<b>Bibliography</b>	<b>93</b>



# List of Figures

2.1	Simplified model of a coded transmission system over the additive Gaussian noise channel. . . . .	8
2.2	Capacity of uniform M-QAM formats. . . . .	13
2.3	The constellation diagram of PS-16QAM. . . . .	15
2.4	Block diagram of PAS. . . . .	17
2.5	Optimal operating points of 8-ASK for PAS ( $R_c = 2/3$ ) and extended PAS ( $R_c = 3/4$ ). . . . .	18
2.6	Bipartite graph of the family of regular non-binary codes (2,3). . . . .	22
2.7	Tanner graph of the family of regular non-binary codes (2,3). . . . .	23
2.8	Operations for parity check nodes in the Fourier domain. . . . .	26
2.9	Tanner graph of the family of regular non-binary codes (2,3) with the update of the check nodes by Fourier. . . . .	27
2.10	SICM model based on q-ary LDPC code and M-QAM. . . . .	33
2.11	CM, SICM and BICM capacities for $q^2$ -QAM with natural binary and binary Reflected Gray mappings. . . . .	34
2.12	CM, SICM and BICM capacities for 64-QAM using Binary Reflected Gray mapping and channel codes over GF(4). . . . .	34
2.13	Examples of studied QAM constellation diagrams. . . . .	36
2.14	CM, SICM, and BICM capacities for 16, 64, and 256-QAM constellations built by superposition. . . . .	36
3.1	SB-QPSK rate as a function of $\alpha$ at an SNR of 11 dB and for $\Lambda = 6$ dB compared to the one of DP-QPSK. . . . .	41
3.2	DP-QPSK rate as a function of the two angles $\alpha$ and $\beta$ for $\Lambda = 6$ dB at an SNR of 11 dB. . . . .	41
3.3	Numerical evaluation of worst rate overall channel SOPs ( $\alpha, \beta$ ) for DP-QPSK encoded with the $f_{(\eta, \nu)}$ function for a PDL $\Lambda = 6$ dB at an SNR of 11 dB. . . . .	44
3.4	ZOCs of the non-precoded and NSB QPSK schemes vs. SNR for $\Lambda = 6$ dB (where the SICM scheme coding is defined over a field of order $Q = M$ ). . . . .	45

3.5	SB-QPSK CM, BICM and SICM as a function of the two angles $\alpha$ and $\beta$ for $\Lambda = 6$ dB at an SNR of 11 dB. . . . .	46
3.6	SB-QPSK CM, BICM and SICM as a function of the two angles $\alpha$ and $\beta$ for $\Lambda = 6$ dB at an SNR of 6 dB. . . . .	47
3.7	Worst CM and BICM rates for the SB and DP schemes as a function of SNR for $\Lambda = 6$ dB. . . . .	47
3.8	SB's worst CM and BICM rates as a function of $\eta$ at different SNRs for $\Lambda = 6$ dB (the solid and dashed lines represent the CM and BICM capacities, respectively). . . . .	48
3.9	NSB-QPSK CM, BICM and SICM as a function of the two angles $\alpha$ and $\beta$ for $\Lambda = 6$ dB at an SNR of 11 dB. . . . .	49
3.10	NSB-QPSK CM, BICM and SICM as a function of the two angles $\alpha$ and $\beta$ for $\Lambda = 6$ dB at an SNR of 6 dB. . . . .	49
3.11	Worst CM and BICM rates for the NSB and DP schemes as a function of SNR for $\Lambda = 6$ dB. . . . .	50
3.12	NSB's worst CM and BICM rates as a function of $\eta$ and $\nu$ for $\Lambda = 6$ dB at an SNR of 6 dB. . . . .	51
3.13	DP-16QAM and SB-16QAM MI in a 6dB-PDL channel as a function of SNR . . . . .	51
3.14	DP-16QAM and SB-16QAM MI in a 6dB-PDL channel as a function of SNR . . . . .	52
3.15	Optical communication system with binary PAS. . . . .	53
3.16	CM performance of different schemes when using QAM signals. . . . .	55
3.17	SICM performance of different schemes when using QAM signals. . . . .	57
3.18	BER versus SNR for protograph based codes using $H_{B_1}$ and $\tilde{H}_{B_1}$ . . . . .	59
4.1	Three different GS-QAM. . . . .	63
4.2	Three different GS-APSK. . . . .	64
4.3	Comparison between the GS-QAM and GS-APSK . . . . .	65
4.4	GS-APSK observed as rotated GS-PAM. . . . .	66
4.5	Types of CQAM-like constructions. . . . .	67
4.6	Information rate as a function of SNR over the linear AWGN channel for a constellation size $M = 64$ . . . . .	68
4.7	The different studied 64-CQAM constellation diagrams. . . . .	69
4.8	The different studied 256-CQAM constellation diagrams. . . . .	69
4.9	CM capacity for the stretched $(8 \times 8)$ CQAM at 11 dB SNR as a function of the stretching parameters. . . . .	70

4.10	CM capacity performances estimated from a white Gaussian noise channel, as a function of the SNR for uniform 64-sized constellations. . . . .	71
4.11	CM capacity performances estimated from a white Gaussian noise channel, as a function of the SNR for uniform 256-sized constellations. . . . .	72
4.12	SICM capacity performances estimated from a white Gaussian noise channel as a function of the SNR for 64-sized constellations.	72
4.13	SICM capacity performances estimated from a white Gaussian noise channel as a function of the SNR for 256-sized constellations.	73
5.1	Comparison of constant composition and sphere codes regarding rate loss. The target shaping rate is $R_s = 1.75$ bit/amp. with 8-ASK. . . . .	80
5.2	System model of PAS with non-binary $\mathbb{F}_q$ codes. . . . .	81
5.3	Illustration how the codeword symbols of a $\mathbb{F}_4$ code are associated with amplitudes and parity symbols for $(16 \times 4)$ CQAM with PAS.	83
5.4	FER vs SNR for $(8,8)$ CQAM at transmission rate $R_t=4$ and shaping blocklength $n = 96$ . . . . .	85
5.5	FER vs. SNR for $(16,4)$ CQAM at transmission rate $R_t=4$ and shaping blocklength $n = 96$ . . . . .	86



# List of Tables

3.1	Optimal shaping schemes in the PDL channel. . . . .	56
4.1	SNR thresholds in dB for different non-binary constellations over $q = M = 64$ and regular $(2, d_c)$ non-binary protograph codes. . . . .	74
4.2	SNR thresholds in dB for 64-GS APSK and QAM constellations over $q = \sqrt{M} = 8$ for different protographs. The left column in blue corresponds to punctured variable nodes. . . . .	75
5.1	Gain in dB of PS for circular constellations: (8,8)-CQAM, (4,16)-CQAM and (16,4)-CQAM. . . . .	81
5.2	Gain in dB of PS for circular constellations: (16,16)-CQAM, (8,32)-CQAM and (32,8)-CQAM. . . . .	82



# List of Abbreviations

<b>APP</b>	<b>A</b> <b>P</b> osterioui <b>P</b> robability
<b>AWGN</b>	<b>A</b> dditive <b>W</b> hite <b>G</b> aussian <b>N</b> oise
<b>APSK</b>	<b>A</b> mplitude <b>P</b> hase <b>S</b> hift <b>K</b> eying
<b>BMD</b>	<b>B</b> it <b>M</b> etric <b>D</b> ecoding
<b>BER</b>	<b>B</b> it <b>E</b> rror <b>R</b> ate
<b>BICM</b>	<b>B</b> it <b>I</b> nterleaved <b>C</b> oded <b>M</b> odulation
<b>BP</b>	<b>B</b> elief <b>P</b> ropagation
<b>CCDM</b>	<b>C</b> onstant <b>C</b> omposition <b>D</b> istribution <b>M</b> atcher
<b>CM</b>	<b>C</b> oded <b>M</b> odulation
<b>CQAM</b>	<b>C</b> ircular <b>Q</b> uadrature <b>A</b> mplitude <b>M</b> odulation
<b>DM</b>	<b>D</b> istribution <b>M</b> atcher
<b>DVB</b>	<b>D</b> igital <b>V</b> ideo <b>B</b> roadcasting
<b>EXIT</b>	<b>EX</b> trinsic <b>I</b> nformation <b>T</b> ransfer
<b>ESS</b>	<b>E</b> numerative <b>S</b> phere <b>S</b> haping
<b>FER</b>	<b>F</b> rame <b>E</b> rror <b>R</b> ate
<b>FEC</b>	<b>F</b> orward <b>E</b> rror <b>C</b> orrection
<b>FFT</b>	<b>F</b> ast <b>F</b> ourier <b>T</b> ransform
<b>GF</b>	<b>G</b> alois <b>F</b> ield
<b>GS</b>	<b>G</b> eometric <b>S</b> haping
<b>LDPC</b>	<b>L</b> ow <b>D</b> ensity <b>P</b> arity <b>C</b> heck
<b>LLR</b>	<b>L</b> og <b>L</b> ikelihood <b>R</b> atio
<b>MAP</b>	<b>M</b> aximum <b>A</b> <b>P</b> osteriori
<b>MIMO</b>	<b>M</b> ultiple <b>I</b> nput <b>M</b> ultiple <b>O</b> utput
<b>MLC</b>	<b>M</b> ulti <b>L</b> evel <b>C</b> oding
<b>MB</b>	<b>M</b> axwell <b>B</b> oltzmann
<b>MI</b>	<b>M</b> utual <b>I</b> nformation
<b>NSB</b>	<b>N</b> ew <b>S</b> patially <b>B</b> alanced
<b>PS</b>	<b>P</b> robabilistic <b>S</b> haping
<b>PEXIT</b>	<b>P</b> rotograph <b>EX</b> trinsic <b>I</b> nformation <b>T</b> ransfer
<b>PAS</b>	<b>P</b> robabilistic <b>A</b> mplitude <b>S</b> haping
<b>PAM</b>	<b>P</b> ulse <b>A</b> mplitude <b>M</b> odulation

<b>PDL</b>	<b>P</b> olarization <b>D</b> ependent <b>L</b> oss
<b>QAM</b>	<b>Q</b> uadrature <b>A</b> mplitude <b>M</b> odulation
<b>QPSK</b>	<b>Q</b> uadrature <b>P</b> hase <b>S</b> hift <b>K</b> eying
<b>SMD</b>	<b>S</b> ymbol <b>M</b> etric <b>D</b> ecoding
<b>SICM</b>	<b>S</b> ymbol <b>I</b> nterleaved <b>C</b> oded <b>M</b> odulation
<b>SNR</b>	<b>S</b> ignal-to- <b>N</b> oise <b>R</b> atio
<b>SB</b>	<b>S</b> patially <b>B</b> alanced
<b>SC</b>	<b>S</b> patially <b>C</b> oupled
<b>WDM</b>	<b>W</b> avelength <b>D</b> ivision <b>M</b> ultiplexing
<b>ZOC</b>	<b>Z</b> ero <b>O</b> utage <b>C</b> apacity

# Chapter 1

## Introduction

Modern communication and storage systems attempt to achieve reliable and efficient transmission/storage. Forward error correction (FEC) is among the most potent techniques to improve reliability. By adding some redundancy to the information bits, FEC reduces the number of transmission errors, extends the operating range, and reduces the power requirements for communication systems [1]. In 1948, Shannon demonstrated that error-free transmission could be realized for every noisy channel through FEC codes with any code rate up to the channel capacity. This is called the Shannon theory [2]. Thus, the channel capacity determines the maximum amount of redundancy that is used to guarantee error-free decoding. The Hamming code was the first FEC code, invented in 1950 [3]. Then, the low-density parity check (LDPC) code was proposed by Gallager in his doctoral dissertation [4]. However, researchers ignored LDPC codes and their variants in the subsequent 35 years because they needed to be more practical to implement.

In 1993, the turbo code was invented by Berrou et al. [5]. It shows an error performance approaching the channel capacity over the additive white Gaussian noise (AWGN) channel. After the notable success of turbo codes, LDPC codes have been revised by Mackay et al. [6–8] and attracted significant attention over the past two decades. They have been shown to reach low bit-error rates (BERs) or frame error rates (FERs) at signal-to-noise ratios (SNRs) very close to the Shannon limits on many engaging channels and applications such as wireless communication systems [9], optical communication systems [10], and magnetic recording systems [11]. Moreover, they outperform turbo codes when the block length of the code is enormous, even though the decoder complexity can be less than that of turbo codes. LDPC codes are widely spread in communication studies such as digital video broadcasting (DVB), 5G, WiFi, and WiMAX. They

are among the three most potent error-correcting code families (turbo, polar, and LDPC).

The present thesis addresses the coded modulation (CM) schemes based on high-order modulation (e.g., quadrature amplitude modulation, QAM) signaling and LDPC channel coding. This is one of the most studied wireless and optical communication schemes. In this perspective, the bit-interleaved coded modulation (BICM) is among well-known bandwidth-efficient CM [12, 13]. The encoded bits in BICM are interleaved and mapped to a particular constellation using some binary labeling/mapping, usually Gray mapping. The BICM does not achieve the highest AWGN capacity but can operate very close to the CM capacity for some coding rates or when using geometric shaping (GS) or probabilistic shaping (PS) [14–16]. The latter has received the most attention from the optical community thanks to its performance gains in spectral efficiency. Different shaping methods involving multi-dimensional geometric considerations have been conceived in the past, and we note, for example, shell mapping [17], and trellis CM [18] for wire-line communications. This thesis focuses on time-invariant non-uniform signaling in combination with probabilistic amplitude shaping (PAS) [14, 19] and circular QAM (CQAM) modulations [16]. Moreover, this thesis addresses the symbol-interleaved coded modulation (SICM) framework [20]. The motivation for the SICM scheme within this thesis stems from the fact that non-binary coding systems are better for vector channels, i.e., for channels where symbols carry vectors of bits such as QAM and MIMO. In recent years, the interest has focused on using LDPC codes over non-binary alphabets thanks to their excellent performance compared to their binary counterparts at finite lengths and in the context of vector channels. Non-binary LDPC codes are believed to be a suitable solution for transmission scenarios that require high spectral efficiency and low error rates. Some exciting designs based on non-binary codes have been proposed; see, for instance, [21–23].

The contents and contributions of the thesis chapters are summarized as follows.

Chapter 2 discusses the fundamentals of wireless or wired communication systems. First, it describes the main transmission components over the physical channel from the transmitter to the receiver side. Next, some notions used as metrics for performance evaluation are analyzed, and we typically note the mutual information (MI). Afterward, relevant background materials on geometric and probabilistic shaping techniques are presented. The last part of Chapter 2 focuses on the LDPC codes and their asymptotic analysis before concluding with an application concerning the SICM scheme combined with the non-binary

LDPC code. The presented background in this chapter helps develop the coded modulation (CM) schemes in the following chapters.

Chapter 3 focuses on the polarization-dependent loss (PDL) channel in optical networks. A  $2 \times 2$  optical MIMO system is considered with two polarization inputs and two polarization outputs. An optical scheme is qualified as one that maximizes the MI in the worst case, or equivalently the throughput, on all possible unitary methods. Two previous precoding techniques, SB and NSB, which improve the worst case, are revisited and analyzed for the CM and BICM capacities. More detail about the optimization over the two schemes is provided next in Chapter 3. Furthermore, the chapter investigates the combination of the precoded PDL channel and PS encoding to enhance the system's performance. In the last part of the chapter, two new approaches based on non-binary information processing have been tested : (i) the design of protograph non-binary codes under the NSB framework and (ii) the design of a SICM based on non-binary protograph LDPC codes.

After studying and designing some schemes in the optical MIMO channel, Chapter 4 focuses on analyzing and designing shaped modulation schemes on the complex plane. First, we propose the construction of  $(c, p)$  CQAM constellations with equiprobable signaling that can approach the Gaussian capacity. Then, we design simple non-binary protographs for GS constellations to show that we can operate close to the capacity of the underlying modulations.

Chapter 5 proposes combining non-binary LDPC codes with PAS when deploying the CQAM constellations. In this context, we discuss when PS using non-binary LDPC codes can bring extra performance improvement. Our proposed scheme achieves significant performance gains on the AWGN channel for short block lengths compared to uniform signaling.

Finally, Chapter 6 summarizes the main results and states possible directions for future research.



# List of Publications

## Journal Articles

- A. Maalaoui and C. Poulliat: **Probabilistic shaping and precoding for dual-polarization optical MIMO**. – *To be submitted to Elsevier Physical Communications*.

## Conference Papers

- A. Maalaoui, C. Poulliat, and I. Andriyanova: **Circular QAM with sphere shaping and non-binary LDPC codes in the finite length regime**. – *IEEE Int. Symp. Topics Coding*, September 2023, Brest, France.
- A. Maalaoui, C. Poulliat, and I. Andriyanova: **Geometric versus Probabilistic Shaping for Circular-QAM with Nonbinary LDPC Codes**. – *IEEE Int. Symp. Inf. Theory*, June 2022, Aalto, Finland.
- G. Rezgui, I. Andriyanova, A. Maalaoui, and C. Poulliat: **A class of non-binary doubly-generalized LDPC codes for moderate and high code rates**. – *IEEE Int. Symp. Inf. Theory*, July 2021, Melbourne, Victoria, Australia.
- G. Rezgui, A. Maalaoui, I. Andriyanova, C. Poulliat, and C. Méasson: **NB-LDPC codes with high rates achieving low BER over the AWGN channel with QAM signaling** – *IEEE Int. Symp. Inf. Theory Appl.*, October 2020, Kapolei, Hawai'i, USA.



## Chapter 2

# Fundamentals

In this chapter, we review at first some essential concepts about the achievable information rates over single and multiple antennas and the different CM designs, such as the BICM and the SICM schemes. Secondly, we overview the shaping techniques, GS and PS, which are the key technologies to approach the Shannon limit. Then, we discuss the design of LDPC codes that have attracted much attention over the past two decades since they can asymptotically approach the Shannon capacity in various data transmission and storage scenarios. Finally, we end up applying the SICM scheme with non-binary LDPC codes.

## 2.1 Coded Modulations: System Model

### 2.1.1 System Model at the Emitter

Most wireless communication systems incorporate FEC codes, often combined with multiple antennas and link adaptation. In information theory and coding theory, FEC is widely used to control errors in data transmission over noisy or unreliable communication channels. Shannon's central theme was that if the signaling rate of the system is less than the channel capacity, reliable communication can be achieved if one chooses convenient encoding and decoding techniques.

For transmission over the physical channel, Fig. 2.1 shows a simplified model of a coded system. Let  $\mathbb{F}_q = \{0, \dots, q-1\}$  denote the Galois finite field (GF) of order  $q$ . The raw information data is represented as a message sequence  $\mathbf{u} \in \mathbb{F}_q^K$ , of length  $K$ , which consists of bits if  $q = 2$  or symbols if  $q > 2$ . By adding redundant data, the FEC encoder maps the message  $\mathbf{u}$  into a codeword  $\mathbf{c} \in \mathbb{F}_q^N$  of length  $N > K$ . In this perspective, we should mention two structurally

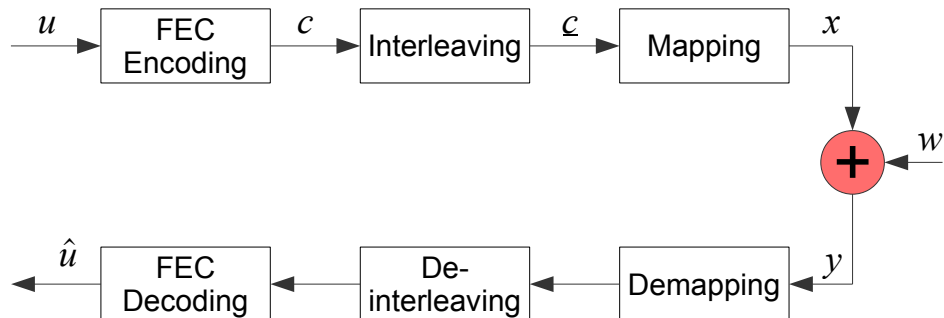


FIGURE 2.1: Simplified model of a coded transmission system over the additive Gaussian noise channel.

different FEC codes commonly used nowadays: block and convolutional. In this thesis, we mainly consider a block structure. The ratio  $R = K/N$  is called the code rate. We talk here about either binary FEC if  $\mathbf{c}$  consists of bits or non-binary FEC if  $\mathbf{c}$  consists of non-binary symbols. The codeword  $\mathbf{c}$  is passed via a bit or a symbol-wise interleaver to obtain the message  $\underline{\mathbf{c}}$ . Before entering the noisy or unreliable channel, the message  $\underline{\mathbf{c}}$  has to be mapped, for example, to  $M$ -ary symbols, where  $M$  is a power of two, for example,  $M \in \{4, 16\}$  for 4-QAM and 16-QAM.

In the general case, we can define a bijective mapping that maps  $m_1$  code bits or symbols to  $m_2$   $M$ -ary symbols such that  $q^{m_1} = M^{m_2}$ . We denote the  $M$ -ary alphabet by  $\mathcal{X} \subset \mathbf{C}$ , and the mapping function by  $\mu : \mathbb{F}_q^{m_1} \rightarrow \mathcal{X}^{m_2}$ . For example, in a BICM scheme based on  $M$ -QAM, we have  $q = 2$ ,  $m_1 = \log_2(M)$ , and  $m_2 = 1$ . Let  $\mathbf{c} = [\mathbf{c}_0, \dots, \mathbf{c}_{N_s-1}]$ , where  $N_s = N/m_1$  and we assume that  $m_1 | N$ . Then,  $\forall n \in \llbracket 0, N_s - 1 \rrbracket$ , we can define  $\underline{\mathbf{c}}_n = (\underline{c}_1^n, \dots, \dots, \underline{c}_{m_1}^n)$ . These  $q$ -ary  $m_1$ -tuples are finally mapped to a vector of  $M$ -ary symbols,

$$\mathbf{x}_n = (x_1^n, x_2^n, \dots, x_{m_2}^n)^T = \mu(\underline{\mathbf{c}}_n) \in \mathcal{X}^{m_2}. \quad (2.1)$$

In this thesis, we will employ LDPC codes, a class of highly efficient linear block codes. Using an iterated soft-decision decoding approach, they can keep performance close to the theoretical limit given by the channel capacity. More details about the LDPC codes are reviewed in section 2.3.

### 2.1.2 Transmission over Multiple Antennas

This thesis will mainly consider single-input single-output (SISO) systems and multiple-input multiple-output (MIMO) systems over the memoryless additive white Gaussian noise (AWGN) channel. Thus, we will consider the following generic model with  $n_T$  transmit, and  $n_R$  receive antennas given by

$$\mathbf{y}_n = \mathbf{H}\mathbf{x}_n + \mathbf{w}_n, \quad (2.2)$$

where  $\mathbf{w}_n \sim \mathcal{CN}(0, N_0\mathbf{I}_{n_R})$  is the complex circular AWGN noise signal, and  $\mathbf{H} \in \mathbb{C}^{n_R \times n_T}$  is the channel matrix, which will be considered constant for a given codeword in our context. Moreover, as we will see in the next chapter, we will have  $n_T = n_R$  and by construction  $m_2 = n_T$ . The transmit power per antenna is  $E_s = \mathbb{E}[|x_i|^2]$ , and hence the SNR is given by  $\text{SNR} = \frac{n_T E_s}{N_0}$ .

At the receiver, the soft demapper computes the a posteriori probability (APP) log-likelihood values ( $\mathbf{L}$ -values), which constitute a sufficient statistic of the received signal  $\mathbf{y}_n$  and form the input of the FEC decoder. This allows to compute  $\forall n \in \llbracket 0, N_s - 1 \rrbracket$  and  $\forall i \in \llbracket 1, m_1 \rrbracket$ , the corresponding APP  $\mathbf{L}$ -vector  $\mathbf{L}(\underline{c}_i^n)$ , whose components are given by

$$L_{k,i}^n \triangleq \ln \left( \frac{P[\underline{c}_i^n = k | \mathbf{y}_n]}{P[\underline{c}_i^n = 0 | \mathbf{y}_n]} \right), \quad (2.3)$$

for  $k \in \mathbb{F}_q \setminus \{0\}$ . The  $\mathbf{L}$ -vector for binary codes reduces to a scalar L-value. In our work, we consider the setting where  $n_T = n_R = 2$ . This means that  $\mathbf{x}_n \in \mathcal{X}^2$  contains 2  $M$ -ary symbols. Besides, we consider the following two scenarios:

- **1<sup>st</sup> scenario ( $\mathbf{q} = \mathbf{M}$ ):** In this case, the Galois field (GF) order is adapted to the size of the constellation  $\mathcal{X}$ . Thus, we have  $m_1 = m_2 = 2$ . Using Bayes' theorem and exploiting the independence of  $x_1^n, x_2^n$ , we can write the soft output value in (2.3) as

$$L_{i,k}^n = \ln \left( \frac{\sum_{\mathbf{x} \in \mathcal{X}^2: \mu_i^{-1}(\mathbf{x})=k} P(\mathbf{y}_n | \mathbf{x}_n)}{\sum_{\mathbf{x} \in \mathcal{X}^2: \mu_i^{-1}(\mathbf{x})=0} P(\mathbf{y}_n | \mathbf{x}_n)} \right) \quad i = \{1, 2\}, \quad k \in \mathbb{F}_q \setminus \{0\}, \quad (2.4)$$

where  $\mu_i^{-1}(\cdot)$  is the inverse mapping function that gives the component  $\underline{c}_i^n = \mu_i^{-1}(\mathbf{x}_n)$  and  $P(\mathbf{y} | \mathbf{x}) \propto \exp \left( - \frac{\|\mathbf{y} - \mathbf{x}\|^2}{N_0} \right)$ .

- **2<sup>nd</sup> scenario ( $\mathbf{q} = \mathbf{M}^2$ ):** In this case, the GF order is adapted to the size of  $\mathcal{X}^2$ , i.e., the number of all possible transmitting symbol vectors in

the MIMO system. Thus, we have  $m_1 = 1$  and  $m_2 = 2$ . The soft output value in (2.3) can be written as

$$L_k^n = \ln \left( \frac{p(\mathbf{y}_n | \mathbf{x}_n = \mu(\mathcal{C}_n = k))}{p(\mathbf{y}_n | \mathbf{x}_n = \mu(\mathcal{C}_n = 0))} \right), \quad (2.5)$$

for  $k \in \mathbb{F}_{M^2} \setminus \{0\}$ .

### 2.1.3 Information Rate for Coded Modulations

We first consider the memoryless single-input single-output AWGN case. For the sake of clarity, the time index is omitted here. Let  $X$  denote the random variable associated with emitted symbols  $\mathbf{x}$  and  $Y$  the random variable associated with the observation  $\mathbf{y}$ . The average mutual information (MI) between a sent symbol  $X$  and a received symbol  $Y$  is denoted by  $\mathbb{I}(X; Y)$ , and it is defined as

$$\begin{aligned} \mathbb{I}(X; Y) &= \mathbb{H}(X) - \mathbb{H}(X|Y) \\ &= - \sum_{x \in \mathcal{X}} P_X(x) \log_2 P_X(x) \\ &\quad + \sum_{x \in \mathcal{X}} P_X(x) \int P_{Y|X}(y|x) \times \log_2 \frac{P_{Y|X}(y|x) P_X(x)}{\sum_{x' \in \mathcal{X}} P_{Y|X}(y|x') P_X(x')} dy, \end{aligned} \quad (2.6)$$

where  $P_X(x)$  is the probability of the discrete channel input and  $x \in \mathcal{X}$ . This quantity operationally corresponds to the so-called CM *information rate*  $C_{\text{CM}} \triangleq \mathbb{I}(X; Y)$ , which represents the maximum rate at which we can communicate. For practical systems, we may operationally refer to the achievable rate associated with the conventional estimation of the representation letter, which can be either a bit or a symbol. This quantity corresponding to bit or symbol maximum a posteriori (MAP) estimation coincides with the classical BICM framework [12, 13, 24–26] or with the SICM, and is a particular case of generalized MI [27, 28]. We first consider the case of a BICM scheme. For such a scheme, assuming that each symbol is equivalently represented by a binary tuple  $(B_1, \dots, B_\ell)$ , with  $\ell = \log_2(|\mathcal{X}|)$ , the BICM information rate is then given as

$$\begin{aligned} C_{\text{BICM}} &\triangleq \mathbb{H}(B_1, \dots, B_\ell) - \sum_{i=1}^{\ell} \mathbb{H}(B_i|Y) \\ &= \sum_{i=1}^{\ell} \mathbb{I}(B_i; Y), \end{aligned} \quad (2.7)$$

where the last equality holds when the  $B_i$  are independent. This can be generalized to a symbol vector representation for which the symbol  $X$  can be equivalently represented by a vector of symbols  $(S_1, \dots, S_m)$ , where  $\forall i = \llbracket 1, m \rrbracket$ ,  $S_i \in \mathcal{S}^i \subset \mathbb{N}$  and with the constraint that  $\prod_i |\mathcal{S}^i| = |\mathcal{X}|$ . As a simple example, we can consider the decomposition of a  $M$ -QAM modulation as the Cartesian product of two independent  $\sqrt{(M)}$ -PAM constellations. The SICM information rate is then given as

$$\begin{aligned} C_{\text{SICM}} &\triangleq \mathbf{H}(S_1, \dots, S_m) - \sum_{i=1}^m \mathbf{H}(S_i|Y) \\ &= \sum_{i=1}^m \mathbf{I}(S_i; Y), \end{aligned} \quad (2.8)$$

where again, the last equality holds when the  $S_i$  are independent. In practice, simple Riemann-based or Monte-Carlo integration methods compute the different information rates. Using the chain rule, and because conditioning reduces entropy, it is quite straightforward to see that

$$C_{\text{CM}} \geq C_{\text{SICM}} \geq C_{\text{BICM}}. \quad (2.9)$$

For an ergodic MIMO channel (i.e., the channel varies from one MIMO symbol to another), and assuming the knowledge of the probability distribution of  $\mathbf{H}$ , the so-called ergodic channel capacity is defined as

$$\bar{C}_H = \mathbb{E}_{\mathbf{H}} \left[ \log_2 \left( \det \left( \mathbf{I}_{n_R} + \frac{\text{SNR}}{n_T} \mathbf{H}\mathbf{H}^H \right) \right) \right], \quad (2.10)$$

where  $\cdot^H$  holds for the conjugate and transpose operator. The above expression holds for transmitting signals that are complex Gaussian distributed. When the channel remains constant over the transmission (i.e., a quasi-static channel), this expression reduces to

$$C(\mathbf{H}) = \log_2 \left( \det \left( \mathbf{I}_{n_R} + \frac{\text{SNR}}{n_T} \mathbf{H}\mathbf{H}^H \right) \right). \quad (2.11)$$

In our case, we deal mainly with constant channels over the transmission. We will also consider symbols that independently sampled belong from a constellation  $\mathcal{X}$  of size  $M$ , i.e.,  $\in \mathcal{X}^{N_t}$ . Let us denote by  $R_q = \log_2(M)$  the number of bits per  $M$ -ary symbol. So, the number of transmitted bits per channel use, denoted by  $R_0$ , equals  $R_0 = n_T R_q$ . Hence we define the set  $\mathcal{X}_M$  of all possible

transmit vectors, of cardinality  $|\mathcal{X}_M| = 2^{R_0}$ . The CM capacity is then given by [26, 29, 30]

$$C_{\text{CM}} = R_0 - \mathbb{E}_{\mathbf{x}, \mathbf{y}} \left( \log_2 \frac{\sum_{\mathbf{z} \in \mathcal{X}_M} p(\mathbf{y}|\mathbf{z})}{p(\mathbf{y}|\mathbf{x})} \right). \quad (2.12)$$

In contrast, the BICM capacity holds for binary processing. If we define with  $\{\mathcal{X}_M\}_k^j \subset \mathcal{X}_M$  the subset that contains all the transmit vectors whose correspondent binary vectors has the value  $j \in \{0, 1\}$  in its  $k$ th position, the BICM capacity is given by [26, 29, 30]

$$C_{\text{BICM}} = R_0 - \sum_{k=1}^{R_0} \mathbb{E}_{\mathbf{x}, j, \mathbf{y}} \left( \log_2 \frac{\sum_{\mathbf{z} \in \mathcal{X}_M} p(\mathbf{y}|\mathbf{z})}{\sum_{\mathbf{z} \in \{\mathcal{X}_M\}_k^j} p(\mathbf{y}|\mathbf{z})} \right). \quad (2.13)$$

From Eq. 2.12 and Eq. 2.13, we should mention that only the BICM capacity but not the CM capacity depends on the labeling. We can also define the SICM scheme as another CM design at this stage. If we define with  $\{\mathcal{X}_M\}_k^s \subset \mathcal{X}_M$  the subset that contains all the transmitting vectors whose correspondent QAM symbol vectors has the value  $s \in \{0, 1, \dots, M-1\}$  in its  $k$ th position ( $k = 1, \dots, n_T$ ), the SICM capacity is given by

$$C_{\text{SICM}} = R_0 - \sum_{k=1}^{n_T} \mathbb{E}_{\mathbf{x}, s, \mathbf{y}} \left( \log_2 \frac{\sum_{\mathbf{z} \in \mathcal{X}_M} p(\mathbf{y}|\mathbf{z})}{\sum_{\mathbf{z} \in \{\mathcal{X}_M\}_k^s} p(\mathbf{y}|\mathbf{z})} \right). \quad (2.14)$$

## 2.2 Geometric and Probabilistic Shaping

Although uniform QAM formats are usually deployed for the ease of generation and detection, there is an asymptotic loss of  $\pi e/6 \approx 1.53$  dB towards the Shannon limit, as shown in Fig. 2.2. According to information theory, this loss can be reduced by the shaping gain if the modulation format gives up a Gaussian distribution. It is worth catching that both coding and shaping are the leading solutions to approach the Shannon limit. However, they perform operationally differently. Coding aims to maximize the distance between the code vectors. In contrast, shaping intends to minimize the average symbol energy and obtain a more considerable Euclidean distance among constellation points at the same power level. As a result, GS or PS can realize shaping gain. The constellation points for the standard QAM formats are located on a uniform Cartesian grid and sent with equal probabilities. In contrast, GS-QAM grants a non-equidistant constellation distribution, while the constellation points in a

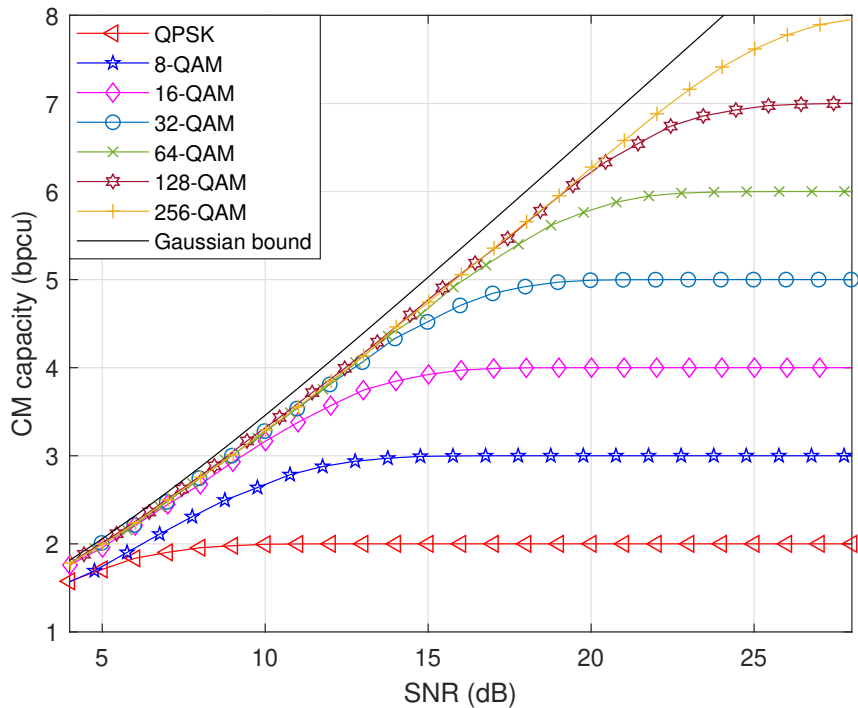


FIGURE 2.2: Capacity of uniform M-QAM formats.

PS-QAM are sent with different probabilities. Although the GS and PS schemes play different roles, they both intend to simulate a quantized sampled Gaussian distribution. Also, they can provide performance closer to the Shannon limit within finite dimensions.

### 2.2.1 Geometric Shaping

The optimal GS constellation depends on the optimization criterion and the SNR. For example, we can adopt the following strategies; minimizing the average symbol error probability, maximizing the MI, or minimizing the mean-square error of Gaussian source representation [31, 32]. Typically, the constellation points with lower amplitude are spaced closer than the outside points. Several works concerning GS-QAM formats, like a generalized cross constellation [33], were proposed in the literature to achieve the shaping gain. Recently, practical GS implementations have been proposed, and we can mention, for example, iterative polar modulation [34], generalized MI-optimized QAM formats [35], and multidimensional constellations with the multi-sphere distribution [36]. Furthermore, in [37], authors show that GS achieves the capacity of the AWGN channel if the number of constellations points tends to infinity.

In [38], authors investigate the achievable rate of GS when symbol-metric decoding (SMD) and bit-metric decoding (BMD) are applied to one-dimensional constellations.

The best constellation depends on the decoding metric used and the SNR. Consider that  $\mathbb{E}[|x|^2] = P$  so that the SNR equals  $P/\mathbb{E}[|w|^2]$ . The GS optimization problem summarizes as follows

$$\begin{aligned} \max_{\mathcal{X}} \quad & R_{\{\text{SMD}, \text{BMD}\}}(\text{SNR}), \\ \text{s.t.} \quad & \mathbb{E}[|x|^2] \leq P, \\ & |\mathcal{X}| = M, \end{aligned} \tag{2.15}$$

where  $R_{\text{SMD}(P_X, \text{SNR})} = \mathbb{I}(X; Y)$  is the information rate when we typically use SMD, and  $R_{\text{BMD}(P_X, \text{SNR})}$  denotes the BMD achievable rate which is given by

$$R_{\text{BMD}} = \left[ \mathbb{H}(B) - \sum_{i=1}^m \mathbb{H}(B_i | Y_i) \right]^+, \tag{2.16}$$

where  $[\cdot]^+ = \max(0, \cdot)$ . The BMD achievable rate in Eq. 2.16 can be given as  $R_{\text{BMD}} = \sum_{i=1}^m \mathbb{I}(B_i; Y)$ , which is the BICM capacity. The optimization problem in 2.15 is non-convex in  $\mathcal{X}$ . Some works in [38, 39] have used constrained non-linear optimization algorithms to find solutions. Authors in [40] have used simulated annealing to optimize amplitude phase shift keying (APSK) constellations.

## 2.2.2 Probabilistic Shaping

### PS Principle

In an AWGN channel, the constellation with PS generally follows a Maxwell-Boltzmann (MB) distribution. Indeed, the latter shows relative performance to the optimal distribution with optimized parameters. Fundamentally, the constellation points within high energy are transmitted with a lower probability. As a consequence, the average symbol power can be reduced. For example, Fig. 2.3 shows the constellation of PS-16QAM with an entropy loss of 0.25 bits/symbol. PS was started with Gallager's many-to-one mapping scheme. Several PS schemes have been proposed, and we note, for example, trellis shaping [32] and shell mapping [17]. In addition, an arithmetic coding-based constant composition distribution matcher (CCDM) has been proposed in [15]. Later, the CCDM-based PAS was presented by Böcherer et al. in [14].

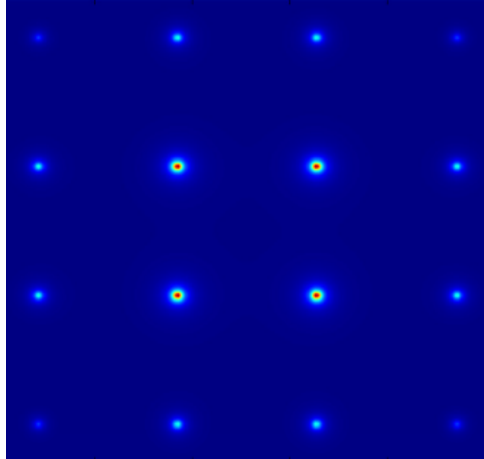


FIGURE 2.3: The constellation diagram of PS-16QAM.

### Probabilistic Amplitude Shaping (PAS)

The invention of PAS was an important achievement in making PS efficient. PAS is a method devised in [14, 41] to implement non-uniform signaling [42]. The generated version no longer refers to modulating “amplitudes” as such, but its original name is conserved for simplicity. Let us instantiate with the real-valued-output channel such as the  $2^m$ -pulse amplitude modulation (PAM) AWGN channel, and set  $x = \Delta\tilde{x}$  where  $\tilde{x} \in \{\pm 1, \pm 3, \dots, \pm(2^m - 1)\}$ , and  $\Delta$  is a positive real-value parameter that denotes the spacing between the constellation points. The matching optimization problem summarizes as follows

$$\begin{aligned} \max_{P_X, \Delta > 0} \quad & R_{\{\text{SMD}, \text{BMD}\}}(P_X, \text{SNR}), \\ \text{s.t.} \quad & \mathbb{E}[|\Delta\tilde{x}|^2] \leq \text{SNR}. \end{aligned} \tag{2.17}$$

$R_{\text{SMD}}$  is convex in  $P_X$  for fixed  $\Delta$  [43]. The following nested approach is employed;

1.  $\Delta$  is optimized by using a simple line search,
2. For each fixed  $\Delta$ ,  $P_X$  is optimized by using efficient and universal optimization algorithms such as the Blahut-Arimoto [44] and the Cutting-Plane [45] approaches.

We can use the mentioned approach for BDM, but  $R_{\text{BMD}}$  is not convex in  $P_X$ . However, we can overcome this problem by optimizing over the MB distributions [42].

PAS is compatible with legacy systems because it can be built around a standard (or pre-existing) FEC coding engine (e.g., an LDPC-based system [14]). PAS first focuses on shaping the distribution of points inside the entire region using the DM. To exemplify this, let us operate the binary case  $q = 2$ . The distribution of the  $2^m$ -PAM amplitudes is shaped to allow the distribution of the whole constellation to behave like the capacity achieving Gaussian [42]. If the standard PAM modulation rate is  $R_M = m$ , then PAS modulates the signal amplitudes at the DM output at rate  $R_{AM} = m - 1$ . PAS uses (up to very few operational changes) a conventional coding and modulation chain. After the DM, the information sequence is parsed to modulate the point amplitudes while the parity bits encode the sign of the PAM amplitudes. In the generalized PAS version, the concatenation chain is divided into three main layers and encoding operations are done sequentially. The block diagram PAS is represented in Fig. 2.4.

1. First, a fraction of the information stream is encoded into a sequence with a given distribution. Hence, uniform independent identically distributed (iid) symbols are encoded into a symbol sequence that labels the modulated regions at rate  $R_{AM}$ . The rate  $R_{AM}$  equals the number of symbols in an alphabet needed to label a region.
2. Second, a sequence of redundant symbols generally obtained from a linear combination of information symbols is generated by a linear channel encoder. Dense linear combinations of symbols make the resulting sum symbols asymptotically uniform.
3. Third, the final encoding layer modulates symbols in  $\mathcal{X}$  by selecting a pair composed of a point in the entire region according to the label sequence.

We now study the rates at which we can achieve reliable transmission. In [15], a reliable communication at a rate  $R$  is achievable only if

$$R < \frac{\sum_{i=1}^n \mathbb{I}(X_i; Y_i)}{n} = \mathbb{I}(X; Y). \quad (2.18)$$

As  $S^n$  represents the data; the transmission rate is given as

$$R = \frac{\mathbb{H}(S^n)}{n} = \mathbb{H}(S) \left[ \frac{\text{bits}}{\text{channel use}} \right]. \quad (2.19)$$

Thus, condition 2.18 can be rewritten as

$$\mathbb{H}(S) < \mathbb{I}(X; Y). \quad (2.20)$$

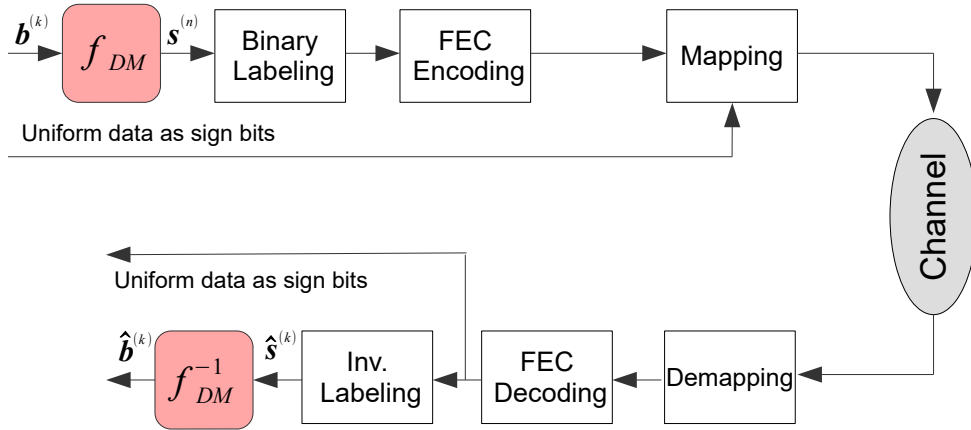


FIGURE 2.4: Block diagram of PAS.

The PAS scheme can sometimes be extended to use code rates higher than  $(m-1)/m$  on  $2^m$ -PAM constellations. This is achieved by using some signs from a data source that generates uniformly distributed bits. This extension of the PAS scheme is illustrated in Fig. 2.4. Let  $\gamma n$  denote the number of signs used for data bits. The  $\gamma n$  bits and the  $(m-1)n$  bits from the amplitude labels are encoded together by the parity matrix of a coding rate  $R_c$ . This encoding generates the remaining  $(1-\gamma)n$  sign labels.  $R_c$  can be expressed in terms of  $m$  and  $\gamma$  as

$$R_c = \frac{m-1+\gamma}{m}, \quad (2.21)$$

and so the fraction gamma is given by

$$\gamma = 1 - (1 - R_c)m. \quad (2.22)$$

Now, the transmission rate of the extended PAS can be expressed as

$$R = \mathbb{H}(S) + \gamma. \quad (2.23)$$

The optimal operating point is then determined by crossing the rate curve  $\mathbb{H}(S) + \gamma$  and the MI rate. To better understand, we take as an example the 8-ASK modulation. In this case,  $m = 3$  is the number of bits per symbol, and the amplitude alphabet is  $\mathcal{S} = \{1, 3, 5, 7\}$  where each amplitude symbol is represented by 2 bits. Hence,  $R_c = (2 + \gamma)/3$ . In Fig. 2.5, we display for 8-ASK the optimal operating points for  $R_c = 2/3$  and  $R_c = 3/4$ .

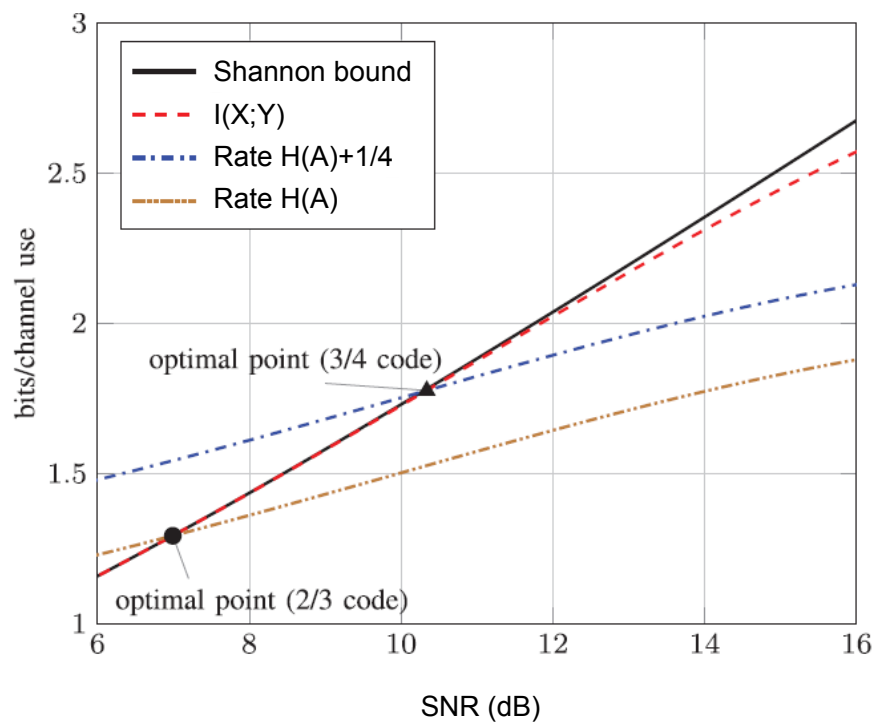


FIGURE 2.5: Optimal operating points of 8-ASK for PAS ( $R_c = 2/3$ ) and extended PAS ( $R_c = 3/4$ ).

### Non-uniform CCDM

This section describes the principle of CCDM that we will employ in this thesis. We consider a distribution matcher (DM) that maps a binary input  $\mathbf{b}^{(k)} \in \{0, 1\}^{(k)}$  to a shaped output sequence  $\mathbf{s}^{(n)} = (s_1, \dots, s_n)$  of length  $n$ . The DM mapping function creates an invertible mapping  $f_{\text{DM}} : \mathbf{b}^{(k)} \rightarrow \mathbf{s}^{(n)}$ . The sequence  $\mathbf{s}^{(n)}$  consists of different output amplitudes that are taken from the alphabet  $\mathcal{A} = \{a_1, \dots, a_m\}$ . The CCDM output sequence is said to have the composition  $C = \{n_1, \dots, n_m\}$  where  $n_i$  denotes the number of times the  $i$ th amplitude  $a_i$  occurs, i.e.,

$$n_i = |j : s_j = a_i|, \quad (2.24)$$

where  $i \in \{1, \dots, m\}$  and  $j \in \{1, \dots, n\}$ . Thus, the relative frequency  $P_A$  of  $a_i$  is  $P_A(a_i) = \frac{n_i}{n}$ . The number of input bits  $k$  of the DM depends on the number of different output sequences, which is given by the multinomial coefficient

$$M(C) = \binom{n}{n_1, n_2, \dots, n_m} = \frac{(\sum_{i=1}^m n_i)!}{\prod_{i=1}^m (n_i!)}. \quad (2.25)$$

Thus, the input length  $k$  is  $k = \log_2 \lfloor M(C) \rfloor_2$  where  $\lfloor \cdot \rfloor_2$  denotes rounding down to the closest power of two. The rate loss of a DM is then defined as

$$R_{\text{loss}} = \mathbb{H}(A) - \frac{k}{n}, \quad (2.26)$$

where  $\mathbb{H}(A)$  represents the entropy of the amplitudes  $\mathcal{A}$  with the quantized distribution  $P_A$ . Such a quantization is essential in many finite-length cases.

## 2.3 LDPC Codes

### 2.3.1 Binary LDPC Codes

Binary LDPC codes are a class of linear error-correcting codes over  $\mathbb{F}_2$  defined by a very sparse parity check matrix  $\mathbf{H}_{(N-K) \times N}$ . We further assume that  $\mathbf{H}_{(N-K) \times N}$  is full rank. The related coding rate of the LDPC is defined as  $R_c = K/N$ . An LDPC code can also be associated with a bipartite graph [46], which consists of bit nodes, check nodes, and a certain number of edges. Each bit/variable node represents one bit of the codeword. Each check node is associated with one parity check of the code. An edge exists between the  $i$ th check node and the  $j$ th variable node if the entry  $\mathbf{H}(i, j) = 1$ . From a Tanner graph point of view, the columns match the variable nodes, whereas the rows match the check nodes. The variable node degree corresponds to the

number of edges connecting the variable node to the check nodes, and the check node degree corresponds to the number of edges connecting the check node to the variable nodes. An irregular LDPC code can be specified by either a degree distribution pair  $(\lambda, \rho)$  [46] or, equivalently, its corresponding generating functions

$$\lambda(x) = \sum_{i=2}^{d_{v_{max}}} \lambda_i x^{i-1} \text{ and } \rho(x) = \sum_{j=2}^{d_{c_{max}}} \rho_j x^{j-1}, \quad (2.27)$$

where  $\lambda_i$  is the fraction of edges connected with a variable node of degree  $i$ ,  $\rho_j$  is the fraction of edges connected with a check node of degree  $j$ ,  $d_{v_{max}}$  is the maximal bit degree of any edge, and  $d_{c_{max}}$  is the maximal check degree of any edge. A regular LDPC code has  $\lambda(x) = x^{d_v-1}$  and  $\rho(x) = x^{d_c-1}$ . Gallager presented a decoding algorithm and a detailed performance analysis on regular LDPC codes in his dissertation in 1963 [4].

The decoding process of the binary LDPC codes is performed through the so-called (SPA), also referred to as the *belief propagation* (BP) algorithm [46]. At the receiver, the demapper outputs the scalar log-likelihood ratio (LLR) values used by a variable node  $v_i, \forall i = 0, \dots, N-1$ . Then, the LDPC decoding process is divided into two steps at a given iteration: the variable node update and the check node update. A variable node  $v_i$  of degree  $dv_i$  has  $dv_i$  edges connected to check nodes and one edge connected to the demapper. The LLR information, passing through the edge connecting variable node  $v_i$  to its adjacent check nodes, is noted  $\{\mathcal{L}_{v_i, c_j}\}_{j \in \mathcal{V}_i}$  where  $\mathcal{V}_i$  denotes the set of check nodes adjacent to  $v_i$ . The LLR information carried by the channel to variable node  $v_i$  is noted  $\mathcal{L}_{ch_i, v_i}$ . At a given iteration  $\ell > 0$ , the variable node update for the variable node  $v_i, \forall i = 1 \dots N-1$ , is given by

$$\mathcal{L}_{v_i, c_j}^\ell = \mathcal{L}_{ch_i, v_i} + \sum_{k=1, k \neq j}^{dv_i} \mathcal{L}_{c_k, v_i}^{\ell-1}, \quad \forall j \in \mathcal{V}_i, \quad (2.28)$$

where  $\mathcal{L}_{c_j, v_i}^{\ell-1}$  denotes the LLR coming from a check node  $c_j, j \in \mathcal{V}_i$ , to variable node  $v_j$  from the previous iteration. By convention,  $\forall i$ , we have  $\mathcal{L}_{c_j, v_i}^0 = 0, \forall c_j \in \mathcal{V}_i$ . Similarly, a check node  $c_j$  of degree  $dc_j$  has  $dc_j$  edges connected to variable nodes. The LLR information, passing through the edge connecting check node  $c_j$  to its adjacent variable nodes, is noted  $\{\mathcal{L}_{c_j, v_i}\}_{i \in \mathcal{C}_j}$  where  $\mathcal{C}_j$  denotes the set of variable nodes adjacent to  $c_j$ . The check node update for the check node

$c_j, j = 0, \dots, N - K - 1$ , is given as follows

$$\tanh\left(\frac{\mathcal{L}_{c_j, v_i}^\ell}{2}\right) = \prod_{k=1, k \neq i}^{d_{c_j}} \tanh\left(\frac{\mathcal{L}_{v_i, c_j}^\ell}{2}\right), \forall i \in \mathcal{C}_j. \quad (2.29)$$

### 2.3.2 Non-binary LDPC Codes

An alternative approach to conceiving non-binary codes starts with non-binary LDPC codes. In [4], Gallager described arbitrary-alphabet LDPC codes using modulo- $q$  arithmetic. Also, Davey and Mackay considered non-binary LDPC codes for binary input channels [47]. Their definition uses  $\text{GF}(q)$  arithmetic. They have shown that these codes could perform excellently for moderate sizes when the GF order is increased. These results were confirmed by [48], which show that when the GF order grows up, good code profiles for decoding under BP tend to be regular, of type  $(2, \text{xx})$ , often referenced to as ‘‘cycle’’ codes. These codes offer good performance at short blocklengths at the expense of high decoding complexity.

A non-binary LDPC code (in the broad sense) is defined by a sparse parity matrix  $\mathbf{H}$  of size  $(N - K) \times N$ , whose non-zero elements are defined on a group, a ring, or a field. Here, we will consider the LDPC codes whose elements are defined on  $\text{GF}(q)$ , particularly the binary extension fields  $q = 2^p$ . In this context, the non-zero elements  $h_{ij}$  of  $\mathbf{H}$  are elements of  $\text{GF}(2^p)$  (also noted  $\mathbb{F}_{2^p}$ ) where  $q = 2^p$  represents the order of the field. These elements belong to the set  $\mathcal{S} = \{\alpha^k : k = 0 \dots q - 2\}$  where  $\alpha$  is the primitive element (generator) of the field defined as the zero of the primitive polynomial  $P(x)$  associated with the field. Similarly to the binary case, an LDPC code over  $\text{GF}(q)$  is defined by all the codewords  $\mathbf{c} = [c_0, \dots, c_{N-1}] \in \mathbb{F}_q^N$  satisfying  $\mathbf{H}\mathbf{c}^T = 0$ , the operations being carried out in  $\mathbb{F}_q$ . Thus, by now noting  $M_H = N - K$ , a codeword  $\mathbf{c}$  must satisfy the following constraint equations

$$\sum_{j: h_{ij} \neq 0} h_{ij} c_j = 0, \forall i = 0, \dots, M_H - 1. \quad (2.30)$$

Similarly to binary LDPC codes, a family of non-binary LDPC codes is characterized by their degree distributions. A code is considered regular if the number of non-zero elements per row and column noted  $(d_v, d_c)$  is constant. Otherwise, the code is irregular and will be represented by the edge perspective distributions  $\lambda(x)$  and  $\rho(x)$  analogously to the binary case.

For a code from a family, the matrix’s non-zero values are generally generated

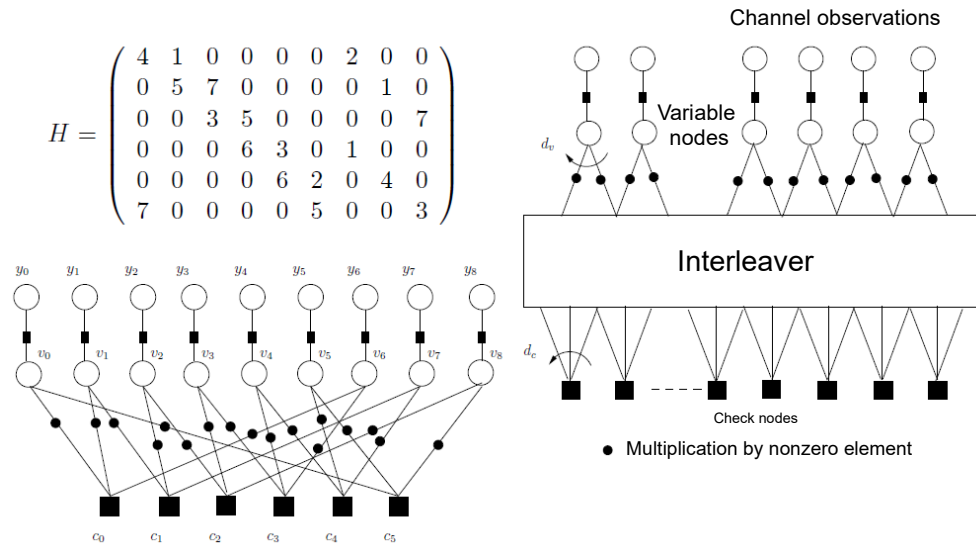


FIGURE 2.6: Bipartite graph of the family of regular non-binary codes (2,3).

uniformly, a very useful assumption in particular for the asymptotic analysis of non-binary LDPC codes. However, carefully selecting non-zero inputs can improve performance for finite-size codes, as shown in [47]. This finite-size optimization is crucial for "cyclic" codes. As in the binary case, we can also associate a Tanner graph. The graph contains nodes of variables  $v_j$ , which are associated with the symbols of the codeword (column of  $\mathbf{H}$ ), and nodes of constraints  $c_i$ , which are associated with the constraints of the code (rows of  $\mathbf{H}$ ). The variable node  $v_j$  is connected to the constraint node  $c_j$  by a branch of the graph if  $h_{ij}$  is a non-zero element. With each branch, we also associate a functional node, which we associate as label the coefficient  $h_{ij}$ . A representation is given in Fig. 2.6 [49].

In the factor graph representation of an LDPC code in  $mathbb{F}_q$ , if we consider iterative decoding by BP based on the probabilities of the symbols, the messages transiting on the graph are probability vectors of size  $q$ . We will note the messages as follows: a message leaving a variable node will be denoted  $V$ . A message leaving a constraint node will be denoted  $U$ . The probability vectors after passing through the functional nodes associated with the branches of the graph will be noted  $\tilde{U}$  and  $\tilde{V}$ , respectively. These steps correspond to the operations associated with the multiplications by the non-zero symbols  $h_{ij}$ .

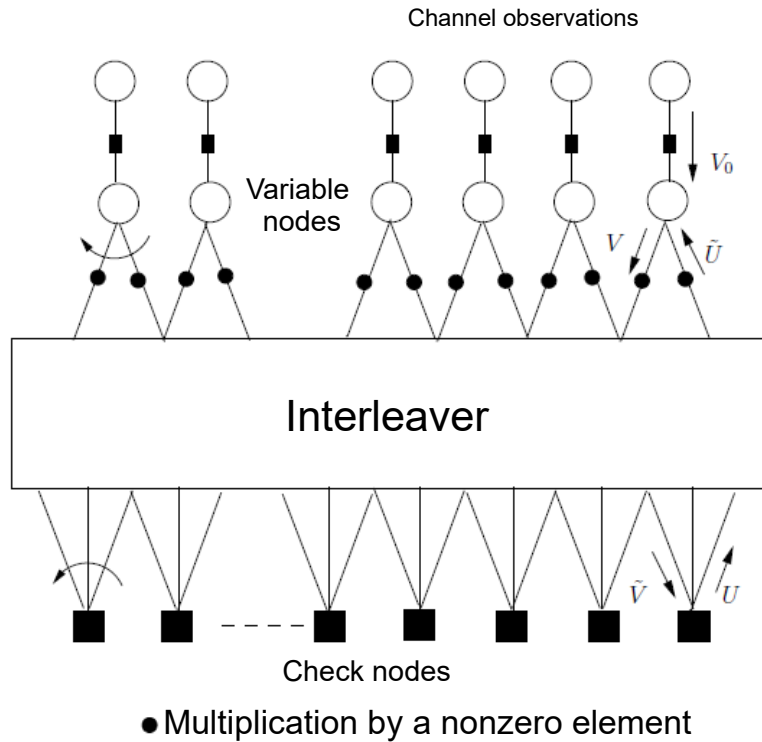


FIGURE 2.7: Tanner graph of the family of regular non-binary codes (2,3).

Finally, the vectors of initial probability densities resulting from the channel observations will be noted  $V_0$ . All messages represent discrete probability density vectors of size  $q$ . By convention, we will consider that the probability vector is ordered by increasing the power of the primitive element  $\alpha$ . By convention, the symbol  $0 \triangleq \alpha^\infty$ . We will therefore consider that the messages will be of type

$$V = \begin{pmatrix} p(v = 0) \\ p(v = 1) \\ p(v = \alpha) \\ \vdots \\ p(v = \alpha^{q-2}) \end{pmatrix}. \quad (2.31)$$

The notations are summarized in Fig. 2.7 [49]. One voluntarily omits in writing these vectors of probabilities the conditioning compared to the messages entering in the functional nodes to simplify the notations.

The non-binary BP algorithm on the factor graph generalizes the binary case. We can then give the main steps of an iteration of this algorithm as follows:

- **Calculation of initial messages:** For a node of variable  $v_j$ , the initial message  $V_0$  corresponds to the APP vector of the transmitted symbol  $x_j$ . The probability vector  $V_0$  is given by

$$V_0 = \begin{pmatrix} p(c_j = 0|y_j) \\ p(c_j = 1|y_j) \\ p(c_j = \alpha|y_j) \\ \vdots \\ p(c_j = \alpha^{q-2}|y_j) \end{pmatrix}.$$

For a memoryless binary-input channel with identically distributed inputs, we have

$$p(c_j|y_j) = \frac{p(y_j|c_j)}{\sum_{j=0}^{q-1} p(y_j|c_j)}.$$

- **Update of variable nodes:** For a variable node  $\mathcal{V}$  of connection degree  $d$ , the message emitted on the  $m$ th output branch  $V_m^{(\ell)}$  at the  $\ell$ th iteration corresponds to the multiplication of the probability vectors (component by component) of the other branches arriving at this variable node. The formal expression is given by

$$V_m^{(\ell)} = V_0 \prod_{k=0, k \neq m}^d \tilde{U}_k^{(\ell-1)}.$$

By convention, we take  $\tilde{U}_k^{(0)} = 1/q \mathbf{1}$ .

- **Permutation of messages:** Formally, the action of multiplication by a non-binary symbol in the constraint equations results in a cyclic permutation of the coordinates of the message, except for the first coordinate corresponding to the null symbol. By noting  $\mathcal{P}_m(\cdot)$ , the action of permutation induced by the value  $\alpha_m = \alpha^k$  of the label on the considered branch  $m$ , we can then give the relation between  $\tilde{V}_m^\ell$  and  $V_m^\ell$  as follows:

$$\tilde{V}_m^\ell = \mathcal{P}_m(V_m^\ell).$$

By noting

$$V_m^{(\ell)} = \begin{pmatrix} p(v_m = 0) \\ p(v_m = 1) \\ p(v_m = \alpha) \\ \dots \\ p(v_m = \alpha^{q-2}) \end{pmatrix}.$$

then it comes that

$$\tilde{V}_m^{(\ell)} = \begin{pmatrix} p(v_m = 0) \\ p(v_m = \alpha^{q-2-k+1}) \\ \vdots \\ p(v_m = \alpha^{q-2}) \\ p(v_m = 1) \\ \vdots \\ p(v_m = \alpha^{q-2-k}) \end{pmatrix}.$$

- **Update of check nodes:** For a constraint node  $\mathcal{C}$ , of connection degree  $d$ , the calculation of the outgoing messages of the constraint nodes involves the convolution of the incoming messages, which are vectors of discrete probability densities of size  $q$  defined on  $\text{GF}(q)$ . Formally, the vector  $U_k^\ell$  is written in the direct domain as follows:

$$U_k^{(\ell)} = \otimes_{m=1, m \neq k}^d \tilde{V}_m^{(\ell)}. \quad (2.32)$$

We can have an efficient implementation of this convolution using the Fourier transform defined on the finite abelian group  $G(2^p) = (\mathbb{Z}_2^p, +)$  which is the additive subgroup of  $\mathbb{F}_2^p$  (often referred to as Hadamard Transform). By transforming equation (2.32) into the Fourier domain as illustrated in Fig. 2.8, the convolution product becomes the component-by-component product of the message transforms. The message update equation using the Fourier domain is then written as

$$U_k^{(\ell)} = \mathcal{F}^{-1} \left( \prod_{m=1, m \neq k}^d \mathcal{F}(\tilde{V}_m^{(\ell)}) \right).$$

- **Reverse permutation of messages:** This operation is the dual of the previous operation. Considering the  $k$ th outgoing branch of a parity node

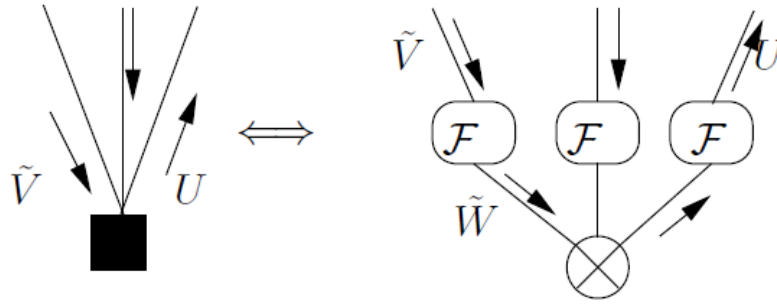


FIGURE 2.8: Operations for parity check nodes in the Fourier domain.

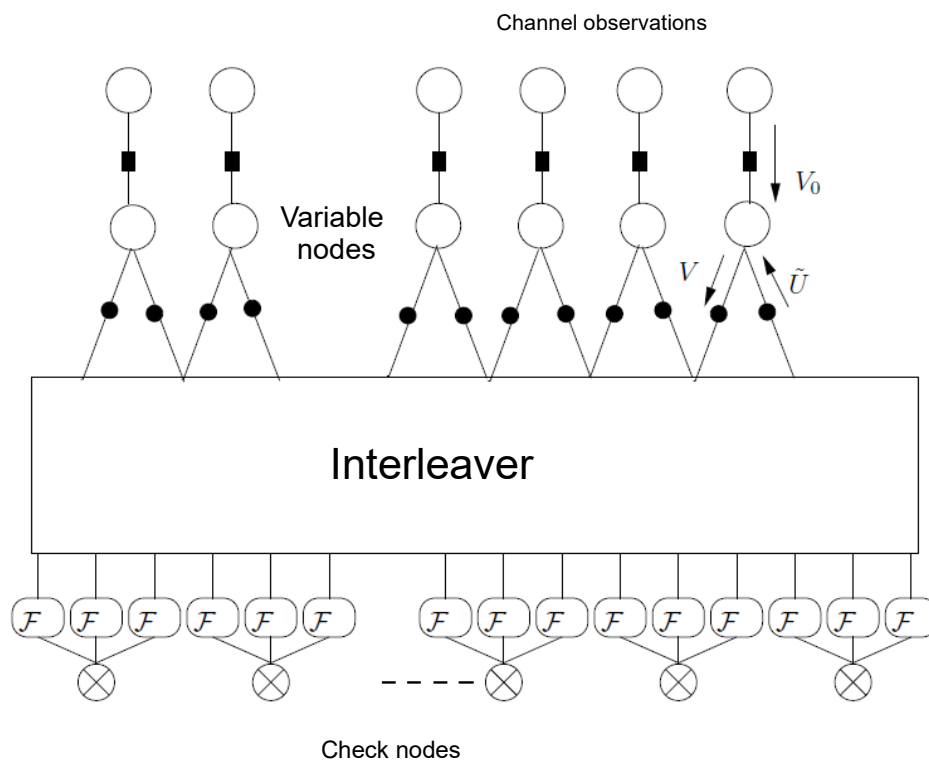
$\mathcal{C}$ , we will formally write the relation between  $\tilde{U}_k^\ell$  and  $U_k^\ell$  as follows:

$$\tilde{U}_k^{(\ell)} = \mathcal{P}_k^{-1} \left( U_k^{(\ell)} \right).$$

where  $\mathcal{P}_k^{-1}$  represents the operation of inverse permutation of the probability vector  $U_k^\ell$  after passing through the functional node associated with the label  $\alpha_k$  of the considered branch. Efficient implementation has been covered, for example, by [50,51]. Reduced complexity algorithms have also been proposed to reduce decoding complexity; see, for example, [51,52] and related references. Finally, the graph equivalent to the graph in Fig. 2.6 used for decoding is given in Fig. 2.9 [49].

### 2.3.3 Protograph-based LDPC Codes

In the last decade, the coding community has proposed more structured LDPC codes, including protograph-based ones. Protograph codes were first introduced in [53]. A protograph is defined using a small bipartite graph composed of  $n_p$  variable node (VN) types and  $m_p$  check node (CN) types connected by edges. For this type of structured graph, degree one VN and multiple parallel edges between a VN and a CN are allowed. The corresponding  $m_p \times n_p$  adjacency matrix is given by  $\mathbf{H}_B = [h_{i,j}]$  where  $h_{i,j} \in \mathbb{N}^* \cup \{0\}$ . A larger bipartite graph associated with an LDPC code of size  $N = n_p L$  and  $M_H = m_p L$  is obtained from a protograph by lifting (or expansion), where  $L$  is called lifting factor [54]. In the non-binary case, each edge of the expanded graph is further associated with a non-zero element in the field  $\mathbb{F}_q$ . The corresponding adjacency matrix gives the sparse parity check matrix  $\mathbf{H}$  associated with a binary or non-binary LDPC code. Many conventional LDPC codes can be generated and represented using protograph representations, e.g., the repeat-accumulate (RA) codes and



- Multiplication by a nonzero element  $\downarrow$

FIGURE 2.9: Tanner graph of the family of regular non-binary codes (2,3) with the update of the check nodes by Fourier.

the regular LDPC codes. The design of these structured codes consists of searching for good base matrices with good thresholds and/or asymptotic minimum distance properties [55]. The following matrices represent two examples of non-binary regular (2, 4) LDPC code and a regular RA code, respectively:

$$\mathbf{H}_{B_1} = \begin{pmatrix} 1 & 1 & 1 & 1 \\ 1 & 1 & 1 & 1 \end{pmatrix}, \text{ and}$$

$$\mathbf{H}_{B_2} = \begin{pmatrix} 2 & 1 & 1 & 1 \\ 1 & 2 & 1 & 1 \end{pmatrix}.$$

## 2.4 Asymptotic Analysis of LDPC Codes using EXIT Charts

The density evolution (DE) [46] and the extrinsic information transfer (EXIT) [56] are two well-known tools employed to study the design and the convergence behavior of sparse-graph codes. The DE tracks the probability density function of LLR messages along the edges of the Tanner graph to compute the convergence threshold. This threshold corresponds to the lowest SNR enabling reliable iterative decoding for long blocklengths. However, the DE method requires high computational complexity, especially when moving from binary to non-binary settings, for which it becomes untractable unless operating some Monte Carlo-based approximations. Thus, EXIT charts have been developed to study the performance of codes under various modulation schemes [50, 57, 58].

The main idea is to compute the average MI rate between the output of a variable node or a check node and the send symbol to evaluate the convergence threshold. In the unstructured case, this enables the definition of the best set of profiles  $(\lambda(x), \rho(x))$ . We first discuss the case of unstructured ensembles and then the extension to the protograph case. We directly address the case of non-binary LDPC codes as it is our main concern.

### 2.4.1 EXIT Charts for Unstructured Ensembles

The EXIT diagram method was introduced by Ten Brink in 2001 [56]. This method was applied for the first time to optimize turbo-decoding algorithms [59]. Later, this tool was adapted to iterative processes at the receive level, notably for turbo-equalization in 2002 [60], and iterative MIMO systems in 2003 [61].

We present here the general coset framework as proposed by [50]. The presented method mixes method 1 and 2 from [50]. This presentation is adopted as it is the method that has been developed in [62] to extend the non-binary EXIT method of [50] to the protograph EXIT (PEXIT) framework. Non-binary EXIT charts consist in tracking the evolution of the average extrinsic mutual information between an extrinsic LLR message  $\mathbf{W} = [W_1, \dots, W_{q-1}]^\top$  at the output of a VN or CN and the related transmitted symbol  $C$ . Assuming some uniform edge labeling (ensuring permutation invariance symmetry) and the use of a random coset to handle the possible use of non-symmetric constellations (message symmetry) [50], messages from check nodes to variable nodes are modeled as a multidimensional Gaussian distribution with parameters

$$\mu = \begin{bmatrix} \sigma^2/2 \\ \sigma^2/2 \\ \vdots \\ \sigma^2/2 \end{bmatrix}_{(q-1) \times 1}, \text{ and } \Sigma = \begin{bmatrix} \sigma^2 & & & \sigma^2/2 \\ & \sigma^2 & & \\ & & \ddots & \\ \sigma^2/2 & & & \sigma^2 \end{bmatrix}_{(q-1) \times (q-1)},$$

that depend on a single scalar parameter  $\sigma$ .

Messages from variable nodes to check nodes are modeled as the sum of channel initial LLR messages  $\mathbf{L}$  and a Gaussian random vector  $\mathbf{X} = [X_1, \dots, X_{q-1}]^\top$ . We note  $\mathbb{I}(C; \mathbf{W}) = 1 - \mathbb{E}_{\mathbf{W}} \left\{ \log_q \left( 1 + \sum_{i=1}^{q-1} e^{-W_i} \right) \mid C = 0 \right\}$ . For a Gaussian random LLR vector  $\mathbf{X}$  with scalar parameter  $\sigma$ , we define

$$J(\sigma) = \mathbb{I}(C; \mathbf{W} = \mathbf{X}).$$

At each iteration  $\ell$ , the non-binary EXIT analysis steps can be summarized as follows:

- **Variable node update:** The average mutual information (MI) between the messages at the output of a variable node and a transmitted symbol  $C$  is given by:

$$I_{v \rightarrow c}^\ell = \sum_i \lambda_i J_R(\sigma_{c \rightarrow v}^{\ell-1}(i)), \quad (2.33)$$

where

$$\begin{aligned} J_R(\sigma) &= \mathbb{I}(C; \mathbf{W} = \mathbf{X} + \mathbf{L}) \\ &= 1 - \mathbb{E}_{\mathbf{X}} \left\{ \log_q \left( 1 + \sum_{i=1}^{q-1} e^{-X_i - L_i} \right) \mid C = 0 \right\}. \end{aligned}$$

$\mathbf{X}$  is a Gaussian random LLR vector with scalar parameter  $\sigma$  and  $\mathbf{L}$  is a

random vector associated to the observations. This latter function is an implicit function of mapping sent symbols and the SNR. This dependence is omitted for clarity of the presentation.  $\sigma_{v \rightarrow c}(i)$  is the Gaussian variance parameter associated with the average MI of messages coming from check nodes to a variable node of degree  $i$ , given as

$$\sigma_{v \rightarrow c}(i) = \sqrt{(i-1)J^{-1}(I_{c \rightarrow v}^{\ell-1})}. \quad (2.34)$$

By convention,  $I_{c \rightarrow v}^0 = 0$ .

- **Check node update:** Similarly, the average MI between the messages at the output of a check node and a transmitted symbol  $C$  is given by

$$I_{c \rightarrow v}^{\ell} = 1 - \sum_j \rho_j J \left( \sqrt{j-1} \cdot J^{-1}(1 - I_{v \rightarrow c}^{\ell}) \right). \quad (2.35)$$

By combining the two previous expressions, we can obtain the following nonlinear recursion:  $I_{v \rightarrow c}^{\ell} = F(I_{v \rightarrow c}^{\ell-1}; \lambda(x), \rho(x), SNR)$ . However,  $F(\cdot)$  can be shown to be linear to the parameters  $\lambda_i$  for a given  $\rho(x)$  and SNR. This can be used to derive efficient methods to optimize unstructured ensembles.

## 2.4.2 Protograph EXIT Charts for Structured Ensembles

The preceding analysis further extends to the case of protograph-based non-binary LDPC codes. Thus, to be as general as possible, the general coset framework [50] is usually used for the analysis. The analysis and design will rely on a classical non-binary Protograph EXIT analysis (PEXIT) [55], which generalizes the PEXIT method as introduced by [63], capitalizing on the EXIT method initially introduced in [57]. PEXIT consists in tracking the evolution of extrinsic mutual information between an extrinsic LLR message  $\mathbf{W} = [W_1, \dots, W_{q-1}]^{\top}$  at the output of a VN or CN over each edge of protograph and the related transmitted symbol  $C$  iteratively. Assuming uniform edge labeling (ensuring permutation invariance symmetry) and the use of a random coset to handle the possible use of non-symmetric constellations (message symmetry) [50], messages from check nodes to variable nodes are still modeled as a multidimensional

Gaussian distribution with parameters

$$\mu = \begin{bmatrix} \sigma^2/2 \\ \sigma^2/2 \\ \vdots \\ \sigma^2/2 \end{bmatrix}_{(q-1) \times 1}, \text{ and } \Sigma = \begin{bmatrix} \sigma^2 & & & \sigma^2/2 \\ & \sigma^2 & & \\ & & \ddots & \\ \sigma^2/2 & & & \sigma^2 \end{bmatrix}_{(q-1) \times (q-1)},$$

that depend on a single scalar parameter  $\sigma$ .

As for the unstructured case, messages from variable nodes to check nodes are modeled as the sum of the LLR message  $\mathbf{L}$  and a random vector  $X = [W_1, \dots, W_{q-1}]^\top$ . At each iteration  $\ell$ , the three steps of PEXIT analysis can be summarized as follows:

- **Variable node update:** Let  $\mathcal{N}_c(j)$  be the set of the check nodes connected to the variable node  $j$ . The mutual information (MI) between the message from the variable node  $j$  to the check node  $i$  and the transmitted symbol  $c_j$  is given by:

$$I_{v \rightarrow c}(i, j) = \begin{cases} J(\sigma_{v \rightarrow c}(i, j)) & \text{if node } j \text{ is punctured} \\ J_R(\sigma_{v \rightarrow c}(i, j)) & \text{otherwise.} \end{cases} \quad (2.36)$$

By definition, we have

$$J(\sigma) = \mathbb{I}(C; \mathbf{W} = \mathbf{X}), \text{ and}$$

$$\begin{aligned} J_R(\sigma) &= \mathbb{I}(C; \mathbf{W} = \mathbf{X} + \mathbf{L}) \\ &= 1 - \mathbb{E}_{\mathbf{X}} \left\{ \log_q \left( 1 + \sum_{i=1}^{q-1} e^{-X_i - L_i} \right) \mid C = 0 \right\} \end{aligned}$$

where  $\mathbf{X}$  is a Gaussian random LLR vector with scalar parameter  $\sigma$  and  $\mathbf{L}$  is a random vector associated to the observations. Both functions are usually obtained through Monte Carlo integrations.

Moreover, we can compute  $\sigma_{v \rightarrow c}(i, j)$  as

$$\begin{aligned} \sigma_{v \rightarrow c}^2(i, j) &= \sum_{s \in \mathcal{N}_c(j), s \neq i} h_{s,j} \left[ J^{-1}(I_{c \rightarrow v}(s, j)) \right]^2 \\ &\quad + (h_{i,j} - 1) \left[ J^{-1}(I_{c \rightarrow v}(i, j)) \right]^2. \end{aligned} \quad (2.37)$$

- **Check node update:** Let  $\mathcal{N}_v(i)$  be the set of the variable nodes connected to the check node  $i$ . Similarly to the previous step, the MI between the message from the check node  $i$  to the variable node  $j$  and the transmitted symbol  $c_j$  is given by

$$I_{c \rightarrow v}(i, j) = 1 - J(\sigma_{c \rightarrow v}(i, j)),$$

where

$$\begin{aligned} \sigma_{c \rightarrow v}^2(i, j) = & \sum_{s \in \mathcal{N}_v(i), s \neq j} h_{i,s} \left[ J^{-1}(1 - I_{v \rightarrow c}(i, s)) \right]^2 + \\ & (h_{i,j} - 1) \left[ J^{-1}(1 - I_{v \rightarrow c}(i, j)) \right]^2. \end{aligned} \quad (2.38)$$

- **A posteriori update and stopping decision:** Finally, the MI between the a posteriori (AP) message and the transmitted symbol  $c_j$  is given by

$$I_{AP}(j) = \begin{cases} J(\sigma_{AP}(j)) & \text{if node } j \text{ is punctured} \\ J_R(\sigma_{AP}(j)) & \text{otherwise.} \end{cases}$$

with

$$\sigma_{AP}^2(j) = \sum_{s \in N(j)} h_{sj} \left[ J^{-1}(I_{c \rightarrow v}(s, j)) \right]^2.$$

The PEXIT analysis procedure stops if  $\forall j \in \llbracket 0, n_h - 1 \cdots \rrbracket$ ,  $I_{AP}(j) = 1$  (asymptotic iterative decoding succeeds) or the maximum number of iterations is reached (asymptotic iterative decoding fails). The asymptotic iterative decoding threshold is the minimum SNR for which reliable iterative decoding can be achieved for a given protograph code ensemble.

## 2.5 Application: SICM with Non-binary LDPC

We study here the case of single input, single output AWGN case. The SICM scheme is given by the serial concatenation of an LDPC code over  $\text{GF}(q)$  of coding rate  $R_c = K/N$ , and a QAM modulation of order  $M = 2^m$  separated by a symbol interleaver as depicted in Fig. 2.10. Consider the  $q^2$ -QAM modulation where  $q = \sqrt{M}$ . Whatever the mapping used for each of the two dimensions, the classical symbol labeling of  $q^2$ -QAM modulations is such that both halves of the labeling are assigned to one constellation dimension. Let  $\underline{c} = [c_1, c_2]$  be the resulting non-binary partitioning of the symbol labeling. Let us denote by



FIGURE 2.10: SICM model based on  $q$ -ary LDPC code and M-QAM.

$C_{\underline{c}_k} = \mathbb{I}(y; \underline{c}_k)$  the equivalent non-binary channel associated with the non-binary label  $\underline{c}_k$ . The SICM capacity is then given by

$$C_{\text{SICM}} = C_{\underline{c}_1} + C_{\underline{c}_2}. \quad (2.39)$$

This partitioning strategy is, in fact, optimal. It can be shown that the CM capacity, in this case, is evenly spread over each dimension, and we have the following equalities:

$$\begin{aligned} C_{\text{CM}} &= \mathbb{I}(y; \underline{c}_1) + \mathbb{I}(y; \underline{c}_2 | \underline{c}_1) \\ &= \mathbb{I}(y; \underline{c}_1) + \mathbb{I}(y; \underline{c}_2) = C_{\text{SICM}}. \end{aligned} \quad (2.40)$$

Note that the second equality is due to the orthogonal non-binary signaling. From Eq. (2.39), one deduces that it is possible to design good non-binary  $q^2$ -QAM modulation schemes when taking an alphabet of order  $q = \sqrt{M}$ . In other words, using  $M$ -ary coding schemes for  $q^2$ -QAM modulations is an unnecessarily complex solution. Two identical  $q$ -ary codes, when put together into non-binary multi-level coding (MLC) scheme, are also asymptotically optimal. Moreover, in the SICM case, two-channel codes of codelength  $N$  can be replaced by one single-channel code of codelength  $2N$ , simplifying the scheme and enabling better performance at finite codelengths. Note that, even for finite codelengths, considering non-binary labelings matched to the order of one signal dimension makes the design asymptotically independent from the possible binary or non-binary labeling of the symbols. Fig. 2.11 illustrated capacities of  $q^2$ -PAM modulations when natural binary and binary reflected Gray mappings are used. As we can see,  $C_{\text{SICM}}$  are naturally equal to  $C_{\text{CM}}$  for all considered mappings. The BICM capacity is also reported, thus showing the impact of the binary labeling of the constellation symbols. Remind that there is no influence when non-binary mapping is used for  $q^2$ -PAM modulations.

When the order  $q$  of the non-binary component codes is less than  $\sqrt{M}$ , the

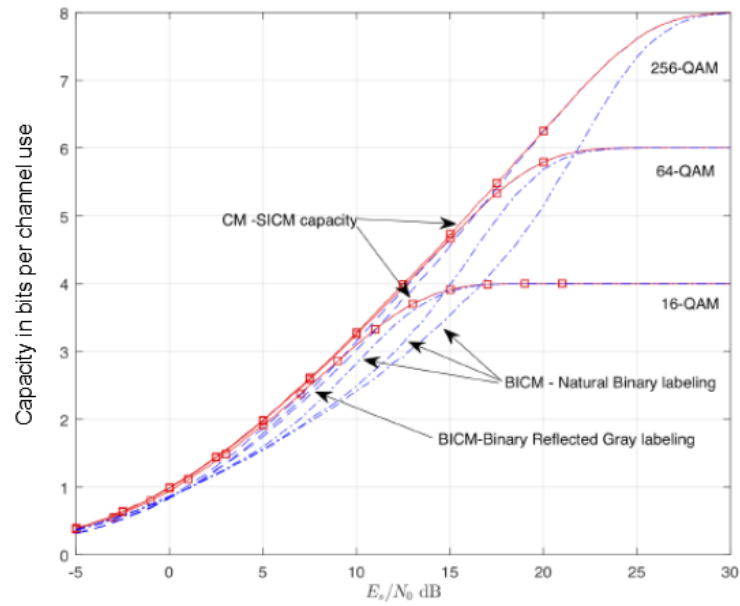


FIGURE 2.11: CM, SICM and BICM capacities for  $q^2$ -QAM with natural binary and binary Reflected Gray mappings.

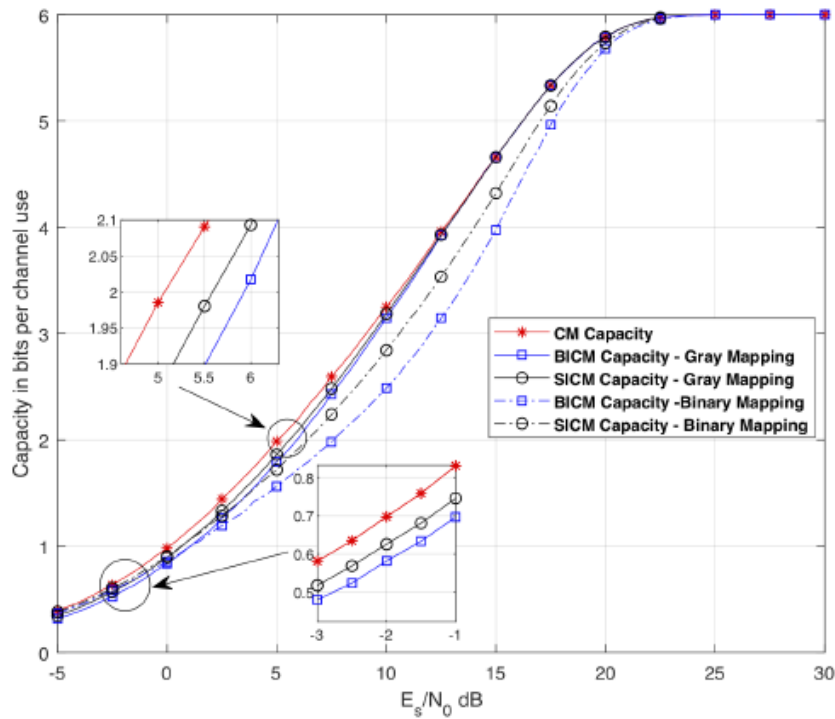


FIGURE 2.12: CM, SICM and BICM capacities for 64-QAM using Binary Reflected Gray mapping and channel codes over  $GF(4)$ .

SICM scheme is no longer optimal, and some performance loss is expected. Fig. 2.12 illustrates capacities for 64-QAM using some channel codes over  $\text{GF}(4)$ . The SICM outperforms BICM only for low capacity rates; gains up to 0.5 dB can be obtained for the Gray mapping, and a substantial gain is observed for the natural binary mapping. We obtain similar results for 256-QAM modulations.

Let us consider the SICM scheme for another family of QAM modulation, which is QAM modulation built by superposition [64, 65], sometimes referred hierarchical modulation. This type of QAM signal is generated based on the linear superposition in the signal space of 4-QAM modulations, following some rules when adding a layer to another to ensure final Gray labeling. Fig. 2.13a shows an example diagram of the hierarchical 16-QAM modulation. While generated quite differently in the signal space, QAM modulations built by superposition and orthogonal modulations perform the same when used in a BICM context. Indeed, it can be shown that bit channels are equivalent to a permutation of the bit labeling when binary-reflected Gray mapping is used. Thus, they are equivalent in terms of performance. However, it is no anymore the case for the SICM scheme. Fig. 2.14 compares the CM, SICM, and BICM capacities for various modulation orders for channel codes over  $\text{GF}(4)$  based on the LTE standard's modulations. Fig. 2.13b shows an example LTE 16-QAM modulation diagram. These constellations are Gray QAM modulations that can be interpreted as superposed QAM modulations. Fig. 2.14 also gives rates of respective layers for the non-binary MLC scheme. It appears that the SICM behaves similarly to the BICM. Only the non-binary MLC scheme can achieve the CM capacity as it benefits from the design by superposition. This example shows that the construction of the modulation matters for SICM schemes. For 64-QAM and 256-QAM modulations with codes defined on  $\text{GF}(8)$  and  $\text{GF}(16)$ , we obtain the same type of results as in Fig. 2.12.

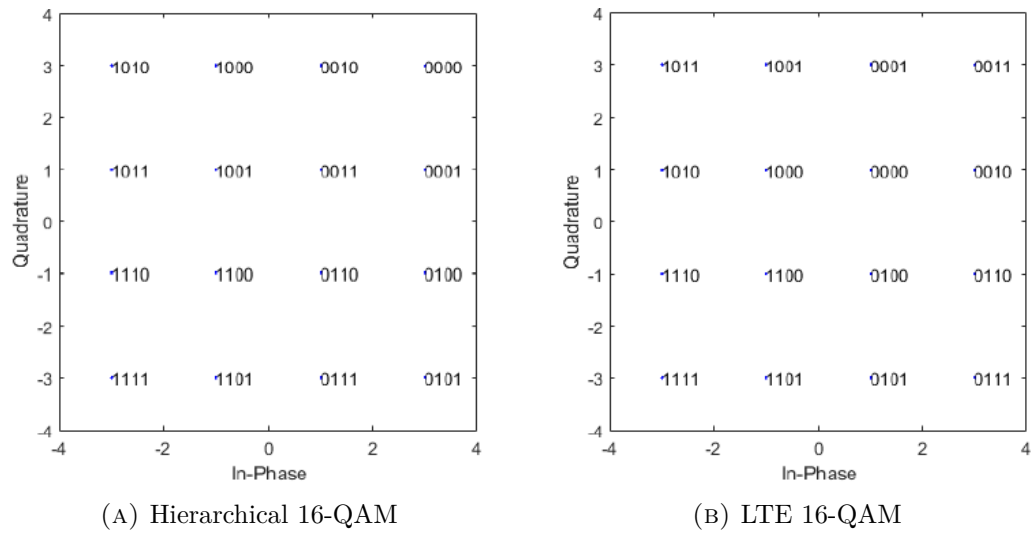


FIGURE 2.13: Examples of studied QAM constellation diagrams.

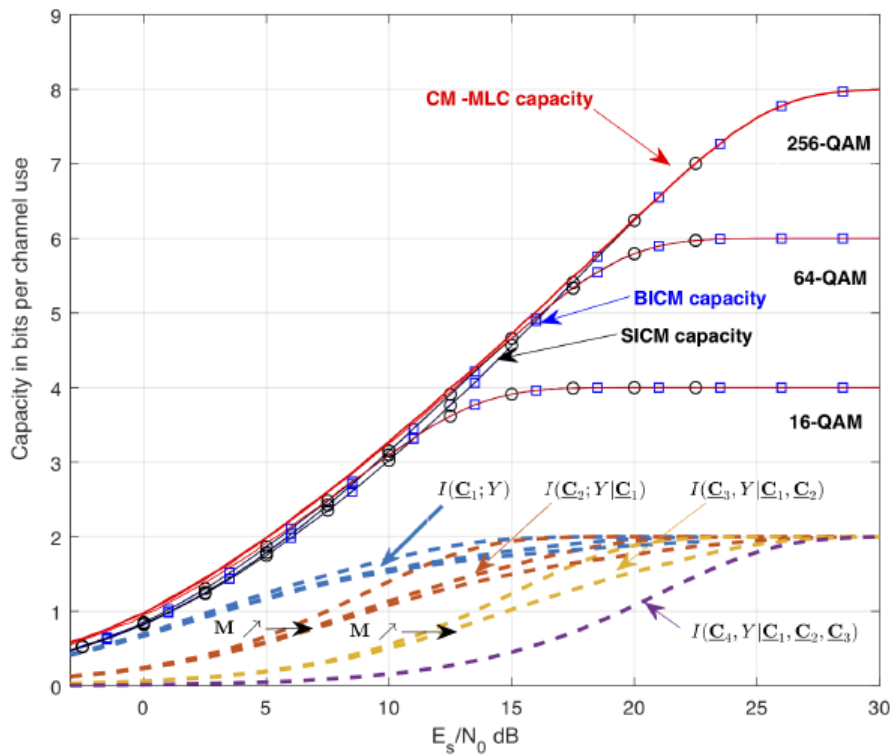


FIGURE 2.14: CM, SICM, and BICM capacities for 16, 64, and 256-QAM constellations built by superposition.

## Chapter 3

# Precoding and Non-binary Coding for Optical MIMO

### 3.1 Introduction

Nowadays, the increasing number of connected people and devices operated by 5G and the high data-consuming applications necessitate considerable communication prospects. Optical networks that represent the foundation of the high data exchange are expected to fulfill this tremendous rate demand. They have been developed in history to answer massive throughput requests. In the 1980s, new materials were invented for constructing optical fibers, the elemental medium of optical communications. This has the advantage of reducing the propagation loss in the fiber and increasing the throughput for a given range. Then, in the late 1990s, the Erbium-Doped Fiber-Amplifier technology came to give access to wavelength division multiplexing (WDM), enabling two orders of magnitude in the bit-rate when exploiting the frequency dimension [66]. After 2005, the last significant development was the capability to recover the phase of the electromagnetic field, allowing the coherent technology [67–69] and the use of polarization division multiplexing (PDM). Therefore, it was possible to quadruple the data sent by implementing multi-amplitude and phase modulation schemes and using a MIMO optical channel. Advanced digital signal processing could then be applied to the receiver to mitigate impairments and channel noise.

In coherent optical networks, PDL is a linear non-unitary impairment expected to have a powerful impact on next-generation systems [70]. Indeed, it reduces the benefit of multiplexing in polarization. Even though the throughput, in theory, is doubled by using both polarizations, PDL can reduce one of the

streams and removes the benefit of having two parallel channels. In this perspective, our work considers a  $2 \times 2$  optical MIMO system as proposed in [71]. At the emission, the signal can be multiplexed on 2 polarizations corresponding to the multiple inputs. At the receiver, it is received on 2 polarizations, corresponding to the multiple outputs. In [72], authors proposed a 2-parameter optimization, referred to as NSB, that allows maximizing the minimal information rate achieved by discrete Pol-Mux QAM transmissions. They compared its performance in CM capacity to a previously proposed scheme called SB. In this chapter, we will present the two mentioned techniques, SB and NSB, and analyze whether these polarizations are optimal when evaluating the BICM and SICM capacities instead of the CM capacity. In addition, we generate an optimized non-uniform distribution of information QAM symbols for the optical MIMO. Simulation results show that the non-uniform distribution of the transmit sequence allows for increasing the throughput of the already deployed fiber schemes, such as the SB and the NSB modulation designs. Besides, we investigate two new approaches based on non-binary information processing that have been tested : (i) the design of protograph non-binary codes under the NSB framework and (ii) the design of a SICM based on non-binary protograph LDPC codes.

## 3.2 PDL Channel Model

### 3.2.1 The Lumped PDL Channel

This work focuses on polarization-multiplexed systems exploiting amplitude/time and phase. So, we consider a  $2 \times 2$  MIMO system with two polarization inputs and two polarization outputs. Typically, we model the system output with a transfer matrix  $\mathbf{H} \in \mathbb{C}^{2 \times 2}$  where its entry  $h_{ij}$  captures how the  $j$ th input polarization sent by the transmitter evolves and is received in the  $i$ th output polarization at the receiver side. In the remainder, we will always consider that we deal with a single channel hence omitting the wavelength dimension. Indeed, it is reasonable to consider that PDL is flat on one WDM channel; thus, we will study PDL in only one channel.

With  $N_t = 2$  polarization inputs and  $N_r = 2$  polarization outputs, the associated communication model is given by

$$\mathbf{y} = \mathbf{H}\mathbf{x} + \mathbf{n}, \quad (3.1)$$

where  $\mathbf{y} = (y_1, y_2)^T \in \mathbb{C}^2$  is the received signal,  $\mathbf{x} = (x_1, x_2)^T \in \mathbb{C}^2$  is the data symbol vector whose elements belong to an  $M$ -QAM modulation  $\mathcal{X}$ , of size  $M$ ,  $x_1$  and  $x_2$  are the modulated symbols.  $\mathbf{n} \sim \mathcal{CN}(\mathbf{0}, N_0 \mathbf{I}_2)$  is an AWGN signal. The SNR can be defined as  $\text{SNR} = \frac{N_t E_s}{N_0}$ , where  $E_s = \mathbb{E} [|\mathbf{x}_i|^2]$ . The PDL matrix  $\mathbf{H}$  depends on  $(\alpha, \beta, \gamma)$  parameters; it decomposes as

$$\mathbf{H}(\alpha, \beta, \gamma) = \mathbf{D}_\gamma \mathbf{R}_\alpha \mathbf{B}_\beta, \quad (3.2)$$

where  $\mathbf{R}_\alpha$  is a real-valued rotation matrix representing the input incident angle  $\alpha \in [0, 2\pi)$ ,  $\mathbf{D}_\gamma$  denotes the real-valued eigenvalues  $\{\sqrt{1+\gamma}, \sqrt{1-\gamma}\}$  with gain imbalance  $\Lambda = 10 \log((1+\gamma)/(1-\gamma))$  in dB, and  $\mathbf{B}_\beta = \text{diag}\{e^{i\beta}, e^{-i\beta}\}$  is the birefringence or retardance matrix with  $\beta \in [0, 2\pi)$ . A frequency-flat model is assumed with lumped noise at the receiver side. The instantaneous MIMO channel capacity solely depends on  $\gamma$ ; thus, we assume  $\gamma$  to be constant over a whole transmission, while the two angles  $\alpha$  and  $\beta$  vary from one codeword to another. However, to remove the dependency in  $\beta$ , an approximation of the PDL channel can be considered; the phase retardance matrix is taken to be  $\mathbf{B}_\beta = \mathbf{I}_2$ . Consequently, the PDL channel depends, in this case, on only one angle parameter

$$\mathbf{H}(\alpha, \gamma) = \mathbf{D}_\gamma \mathbf{R}_\alpha, \quad (3.3)$$

that we call the simple PDL channel. Such simplification is often used in optical communication literature. It can be justified as the MI between  $X$  and  $Y$  strongly depends on the incident angle  $\alpha$  and, to a less extent, on  $\beta$  [72]. Nevertheless, when applicable, it should be remembered that this is not the complete model of the lumped channel. In particular, the negligible variation in  $\beta$  may not hold for a high value of PDL or when changing the input modulation. Therefore, optimum unitary precoding can be applied to the QAM modulation scheme states to offer resilience to PDL, focusing on increasing the worst rate over all channels. In the sequel, we present these precoding techniques, proposed initially by [72] to improve this worst case.

### 3.2.2 The Spatially Balance Signalling

The simple PDL channel gave insight into the construction of PDL-resilient signaling. In this subsection, we present the spatially balanced (SB) signaling that leverages the performance of square M-QAM-based modulation by improving the worst-case capacity [72]. The approach is based on information

rate considerations, and the optimal configuration is based on Euclidean distance observations. We study  $\mathbf{H}(\alpha, \gamma)$  as a real-valued system, and so we obtain two independent channels as follows

$$\mathbf{y} = \mathbf{H}\mathbf{x} + \mathbf{n} \triangleq \begin{cases} \Re(\mathbf{y}) = \mathbf{D}_\gamma \mathbf{R}_\alpha \Re(\mathbf{x}) + \Re(\mathbf{n}), \\ \Im(\mathbf{y}) = \mathbf{D}_\gamma \mathbf{R}_\alpha \Im(\mathbf{x}) + \Im(\mathbf{n}). \end{cases} \quad (3.4)$$

where  $\Re(A)$  and  $\Im(A)$  represent the respective real and imaginary parts of  $A$ . Thus, both polarization streams of the standard DP-QAM modulation scheme (without precoder) are sent in the PDL channel with the same incident angle  $\alpha$ . SB signaling was proposed to avoid the worst angle configurations. Given that the two channels are independent, a rotation is performed by an angle  $\eta$ . If  $\mathbf{f}_\eta$  represents the SB encoding function rotating the imaginary parts, Eq. (3.4) becomes

$$\mathbf{y} = \mathbf{H}\mathbf{f}_\eta(\mathbf{x}) + \mathbf{n} \triangleq \begin{cases} \Re(\mathbf{y}) = \mathbf{D}_\gamma \mathbf{R}_\alpha \Re(\mathbf{x}) + \Re(\mathbf{n}), \\ \Im(\mathbf{y}) = \mathbf{D}_\gamma \mathbf{R}_\alpha \mathbf{R}_\eta \Im(\mathbf{x}) + \Im(\mathbf{n}). \end{cases} \quad (3.5)$$

In Fig. 3.1, we present, at 11 dB SNR, the rate profile of the SB-QPSK and the DP-QPSK modulations for the simple PDL channel, i.e.,  $\beta = 0$ . For the DP-QPSK scheme, the maximum is attained at  $\pi/4$ , so taking an offset angle of  $\alpha = \pi/4$  is relevant. Regarding SB signaling, when one complex part experiences a lower achievable rate, the other part experiences a better channel. We observe in Fig. 3.1 that the SB-QPSK worst rate increases to the middle value from the minimum and maximum values of DP-QAM. As balancing signaling, the rate fluctuations to  $\alpha$  are reduced by construction. These two observations are valid for the entire SNR region, and the worst-case increase is the most significant in the SNR regions where the DP-QAM attains its maximum rate amplitudes.

In the end, we can say that, in general, SB encoding can be defined by rotating both the real and imaginary parts of the DP-QAM constellation to get an equivalently divided offset  $\eta$  between the two rotated M-QAM-like squares on each complex part. In other words, instead of sending  $\mathbf{x}$  that belongs to M-QAM it can be encoded as  $R_{-\eta/2}\Re(\mathbf{x}) + R_{\eta/2}\Im(\mathbf{x})$ .

### 3.2.3 The New Spatially Balance Signalling

The 4-D diagrams are favored candidates for implementation in optical networks, using the actual 4 symbol dimensions, which are the two polarizations' in-phase and quadrature components. Insights into optically relevant physical

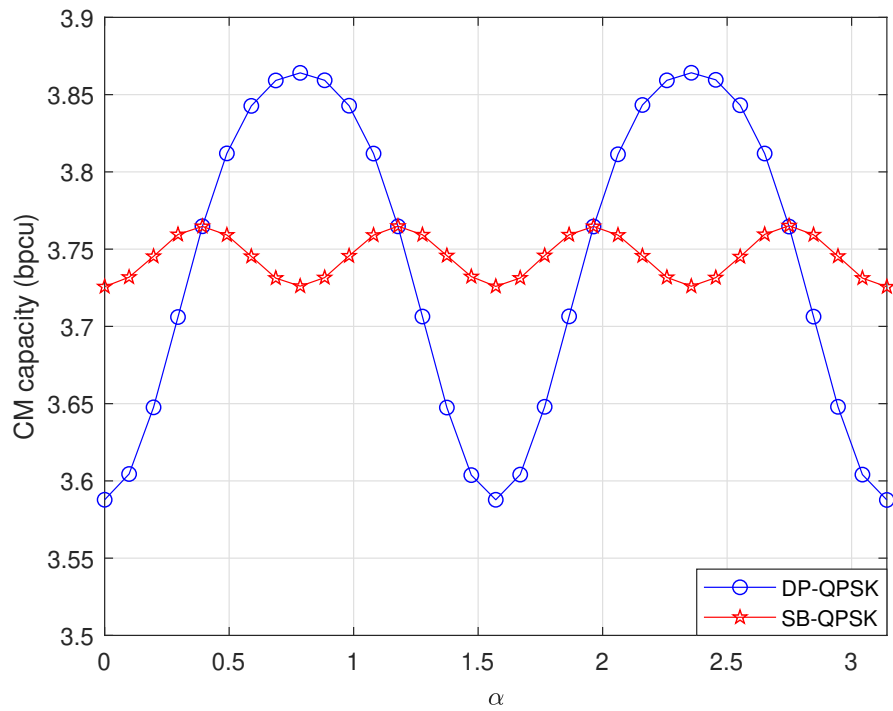


FIGURE 3.1: SB-QPSK rate as a function of  $\alpha$  at an SNR of 11 dB and for  $\Lambda = 6$  dB compared to the one of DP-QPSK.

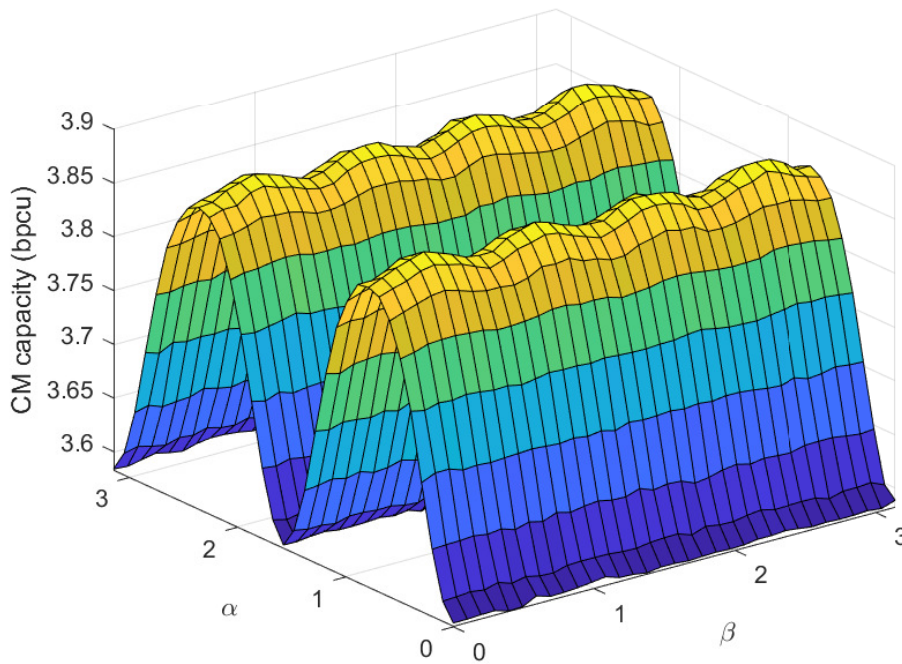


FIGURE 3.2: DP-QPSK rate as a function of the two angles  $\alpha$  and  $\beta$  for  $\Lambda = 6$  dB at an SNR of 11 dB.

and non-physical four-dimensional rotations are first found in [73, 74]. Hence, orthogonal transformations in  $\mathbb{R}^4$  are investigated. Whence simplifying transformations applied over an  $M$ -QAM<sup>2</sup> symbol vector  $\mathbf{x}$ , it can be written as  $e^{i\theta} \mathbf{f}_{\eta,\nu}(\mathbf{x})$ , where  $\mathbf{f}_{\eta,\nu}(\cdot)$  is the unitary precoding function defined as

$$\mathbf{f}_{\eta,\nu}(\mathbf{x}) = \left( \cos(\eta)\mathbf{x} + \sin(\eta)e^{i\nu} \begin{bmatrix} 0 & -1 \\ 1 & 0 \end{bmatrix} \mathbf{x}^* \right), \quad (3.6)$$

where  $\mathbf{x}^*$  is the conjugate of  $\mathbf{x}$  and the Euler angles  $(\eta, \nu) \in [0, 2\pi) \times [0, 2\pi)$ . Note that this precoding is a unitary transformation preserving signal energy. The factor  $e^{i\theta}$  is a scalar phase rotation common to both polarization tributaries and cannot offer any PDL resilience; hence it is omitted in the sequel. The channel model in (3.1) becomes

$$\mathbf{y} = \mathbf{D}_\gamma \mathbf{R}_\alpha \mathbf{B}_\beta \mathbf{f}_{\eta,\nu}(\mathbf{x}) + \mathbf{n}. \quad (3.7)$$

### 3.2.4 Zero Outage Capacity for DP and NSB

The optical fiber MIMO channel is, in essence, a quasi-static channel, i.e., the channel matrix  $\mathbf{H}$  remains constant over a frame or codeword and may vary over time. As no precoding strategy can be used to study the asymptotic achievable rate, the zero-outage capacity (ZOC) of CM [75] is of particular interest. We define the ZOC as the maximum transmission rate to transmit *without any* outages. Let  $H(\alpha, \beta, \gamma)$  be a particular instance of the MIMO channel  $\mathbf{H}$ . For a given precoding strategy  $(\eta, \nu)$ , the achievable information rate for this particular realization of the channel is given by

$$R_{\alpha,\beta}(\eta, \nu) = \mathbb{I}(\mathbf{x}; \mathbf{y} | \mathbf{H} = H(\alpha, \beta, \gamma), \mathbf{f}_{\eta,\nu}(\cdot)), \quad (3.8)$$

where  $\mathbb{I}(\mathbf{x}; \mathbf{y})$  is the MI between variable  $\mathbf{x}$  and  $\mathbf{y}$ . The parameters  $\eta$  and  $\nu$  are optimized in [72] to maximize the minimum of the MI between  $\mathbf{x}$  and  $\mathbf{y}$  for any pair  $(\alpha, \beta)$ , that is

$$(\eta^{\text{opt}}, \nu^{\text{opt}}) = \arg \max_{\eta, \nu} \min_{\alpha, \beta} R_{\alpha,\beta}(\eta, \nu). \quad (3.9)$$

Note that in the particular case where  $\nu = 0$ , Eq. (3.6) enables to construct the SB signal,

$$\begin{aligned} \mathbf{f}_{\eta,\nu=0}(\mathbf{x}) &= \cos \eta \begin{pmatrix} x_1 \\ x_2 \end{pmatrix} + \sin \eta \begin{pmatrix} -x_2^* \\ x_1^* \end{pmatrix}, \\ &= \begin{pmatrix} \cos \eta & -\sin \eta \\ \sin \eta & \cos \eta \end{pmatrix} \begin{pmatrix} \Re(x_1) \\ \Re(x_2) \end{pmatrix} + \begin{pmatrix} \cos \eta & \sin \eta \\ -\sin \eta & \cos \eta \end{pmatrix} \begin{pmatrix} i\Im(x_1) \\ i\Im(x_2) \end{pmatrix}, \\ &= \mathbf{R}_\eta \Re(\mathbf{x}) + i\mathbf{R}_{-\eta} \Im(\mathbf{x}). \end{aligned} \quad (3.10)$$

This encoding leads to an offset angle of  $2\eta$  between the two complex parts of  $\mathbf{x}$ . Section 3.2.2 shows that the optimal value is  $2\eta = \pi/4$  for low values of PDL or another value for higher gain imbalance regimes. Now, we consider all possible  $(\eta, \nu)$  pairs and conduct a numerical evaluation of  $\mathbb{I}(X; Y)$  using Monte-Carlo simulations. We restrict to the channel model in Eq. (3.7) for which we take a PDL value of 6 dB and use a state-of-polarization (SOP) grid with a step of up to  $\pi/64$ . In Fig. 3.3, we plot the  $\min_{\alpha,\beta} \mathbb{I}(X; Y)$  when using QPSK<sup>2</sup> encoded with  $f_{\eta,\nu}$  as defined in Eq. (3.6), at 11 dB SNR (corresponding to a rate of about 0.85). A coarse  $(\eta, \nu)$  grid with a  $\pi/32$  step is used for  $(\eta, \nu) \in [0, \pi/4] \times [0, \pi/4]$  and a finer step of  $\pi/64$  is considered for  $(\eta, \nu) \in [\pi/8, 3\pi/16] \times [3\pi/16, \pi/4]$ . The study is restricted to this range because the worst rate profile is  $\pi/2$ -periodic to  $\eta$  and  $\nu$ .

Following the rate optimization of the encoding parameters in [72], we denote with

$$C_{\text{CM}}^0 = \min_{\alpha,\beta} R_{\alpha,\beta}(0, 0), \text{ and} \quad (3.11)$$

$$C_{\text{CM,NSB}}^0 = \min_{\alpha,\beta} R_{\alpha,\beta}(5\pi/32, \pi/4), \quad (3.12)$$

the ZOCs of the non-precoded and the NSB schemes, respectively. Classically, transmission systems usually consider BICM schemes [12, 26], which consist of a serial concatenation of a binary error-correcting code and a high-order modulation separated by an interleaver. In this context, we define the BICM ZOC in the non-precoded and the NSB schemes as follows

$$C_{\text{BICM}}^0 = \min_{\alpha,\beta} \sum_i \mathbb{I}(B_i; y | \mathbf{H} = H(\alpha, \beta, \gamma), \mathbf{f}_{\eta=0,\nu=0}(\cdot)), \quad (3.13)$$

$$C_{\text{BICM,NSB}}^0 = \min_{\alpha,\beta} \sum_i \mathbb{I}(B_i; y | \mathbf{H} = H(\alpha, \beta, \gamma), \mathbf{f}_{\eta=5\pi/32,\nu=\pi/4}(\cdot)), \quad (3.14)$$

where  $B_i$  is the  $i$ th bit random variable carried by the sent symbol vector. As

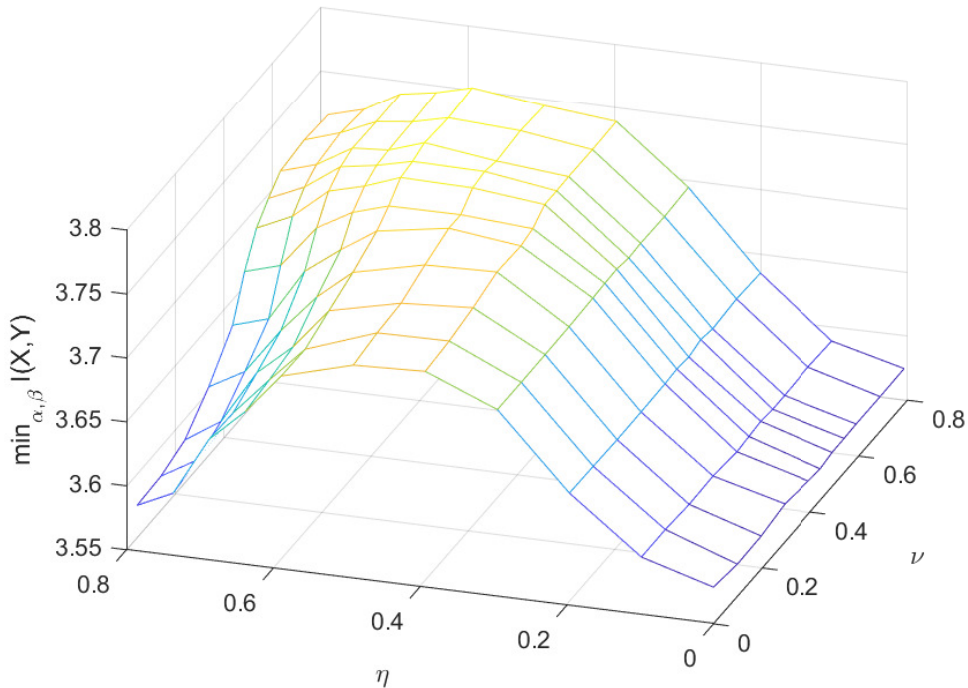


FIGURE 3.3: Numerical evaluation of worst rate overall channel SOPs  $(\alpha, \beta)$  for DP-QPSK encoded with the  $f_{(\eta, \nu)}$  function for a PDL  $\Lambda = 6$  dB at an SNR of 11 dB.

shown in Fig. 3.4, there is an inherent loss of performance for BICM MIMO systems when comparing BICM and CM ZOCs, i.e., when using the same encoding parameters that are optimal for the CM capacity. This motivates the study of non-binary error-correcting codes that can operate closer to the CM ZOC. Therefore, we will also investigate the SICM capacity, particularly the SICM ZOC in the non-precoded and the NSB schemes,

$$C_{\text{SICM}}^0 = \min_{\alpha, \beta} \sum_i \mathbb{I}\left(S_i; y | \mathbf{H} = H(\alpha, \beta, \gamma), \mathbf{f}_{\eta=0, \nu=0}(\cdot)\right), \quad (3.15)$$

$$C_{\text{SICM,NSB}}^0 = \min_{\alpha, \beta} \sum_i \mathbb{I}\left(S_i; y | \mathbf{H} = H(\alpha, \beta, \gamma), \mathbf{f}_{\eta=5\pi/32, \nu=\pi/4}(\cdot)\right), \quad (3.16)$$

where  $S_i$  is the  $i$ th symbol RV carried by the transmitted symbol vector.

### 3.3 Optimization over SB and NSB Schemes

The two optimization techniques, SB and NSB, previously proposed in [72], aim to maximize the minimal achieved CM capacity. As a result, two optimal parameters,  $\eta$ , and  $\nu$ , are identified for each scheme. However, this differs for the BICM and SICM capacities, which are not evaluated with these techniques.

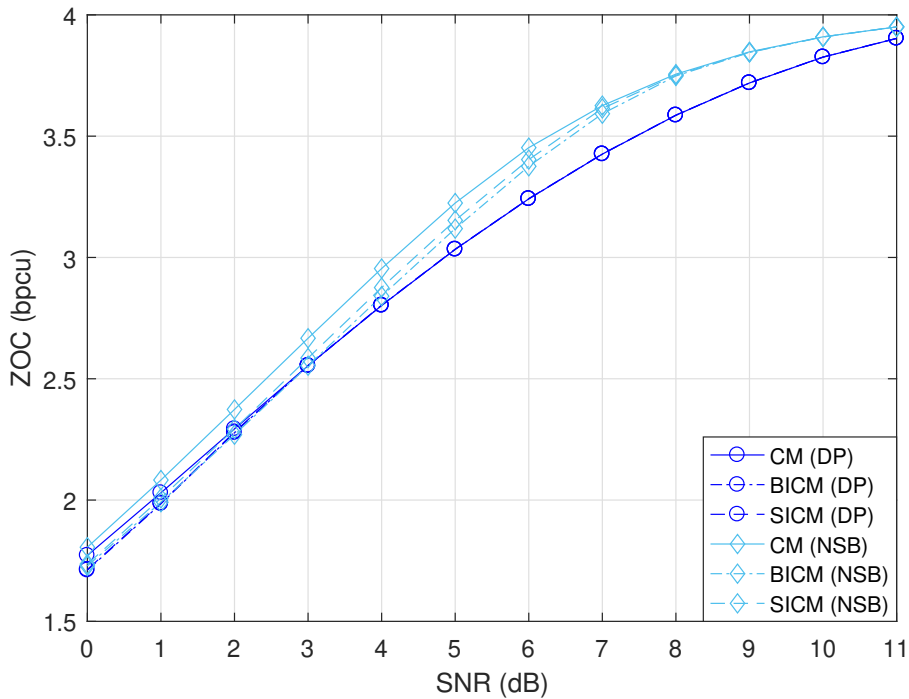


FIGURE 3.4: ZOCs of the non-precoded and NSB QPSK schemes vs. SNR for  $\Lambda = 6$  dB (where the SICM scheme coding is defined over a field of order  $Q = M$ ).

We aim to investigate their optimization and see whether the found parameters are still optimal.

### 3.3.1 Worst BICM and SICM Optimization in the SB

As shown in Fig. 3.1, the worst CM rate is reached for  $\alpha = 0$  modulo  $\pi/2$  and  $\beta = 0$ . We show by simulations that the minimum and the maximum of the worst BICM rate of the SB signaling are obtained for the same angles  $\alpha$  and  $\beta$  compared to the CM capacity. Fig. 3.5 shows that for a high SNR value equal to 11 dB. This result is explained by the fact that since the encoded bits are mapped using the Gray mapping for a high SNR range, the bits are independent, and the BICM scheme behaves as the CM scheme. This is also confirmed for the SICM capacity from Fig. 3.5. Its behavior is similar to that of the CM scheme at a high SNR level. Indeed, its SB's worst rate corresponds to the pair  $(\alpha, \beta)$  that minimizes the maximum of the SB's CM rate.

Conversely, for a low SNR range, the correlation between bits occurs, which explains the difference in behavior between the BICM and the CM schemes. Fig. 3.6 shows, for a low SNR value equal to 6 dB, that the two pairs  $(\alpha, \beta) = (0, 0)$  and  $(\alpha, \beta) = (\pi/4, \pi/8)$  do not correspond to the worst and best cases,

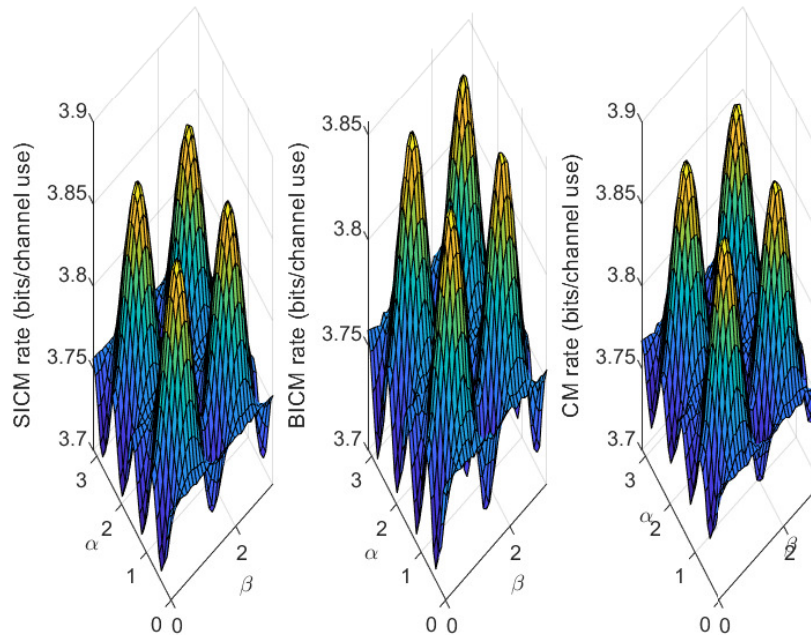


FIGURE 3.5: SB-QPSK CM, BICM and SICM as a function of the two angles  $\alpha$  and  $\beta$  for  $\Lambda = 6$  dB at an SNR of 11 dB.

respectively, for the SB BICM. Although the behavior of the CM and BICM rates is the same function of  $\alpha$  and  $\beta$  at 11 dB, it changes entirely at 6 dB, i.e., for low rates. We observe in Fig. 3.6 that the minimum of the SB's worst BICM rate corresponds to the maximum of the SB's worst CM rate for the same pair  $(\alpha, \beta)$ . However, Fig. 3.6 shows the same behavior between the CM and SICM capacities for low SNRs, as shown at 6 dB. This confirms that the optimal SB polarization is well-founded for the SICM scheme at the entire SNR region.

We plot in Fig. 3.7 the minimum of the SB-QPSK CM, SB-QPSK BICM, and DP-QPSK BICM rates as a function of the SNR by averaging on the angles  $\alpha$  and  $\beta$ . We can figure out that using the SB encoding function  $\mathbf{f}_{\eta, \nu}$  at low SNR ranges is unnecessary. Besides, we find, for high rates, the maximum of the SB worst BICM does not evaluate to  $\eta$ , i.e., the optimal value of  $\eta$  that maximizes the minimum of the SB BICM rate is almost  $\pi/8$  modulo  $\pi/4$ , which is the same angle for the CM rate. In Fig. 3.8, we observe that the SB's worst BICM is much flatter than the SB's worst CM. Unlike the CM rate, the variation between the minimum and the maximum of SB's worst BICM is insignificant for low-to-moderate SNRs.

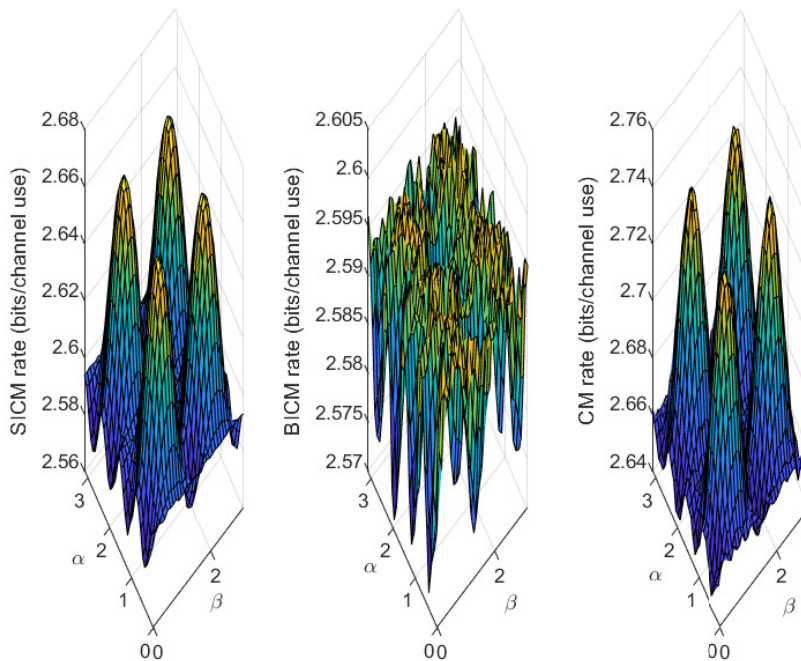


FIGURE 3.6: SB-QPSK CM, BICM and SICM as a function of the two angles  $\alpha$  and  $\beta$  for  $\Lambda = 6$  dB at an SNR of 6 dB.

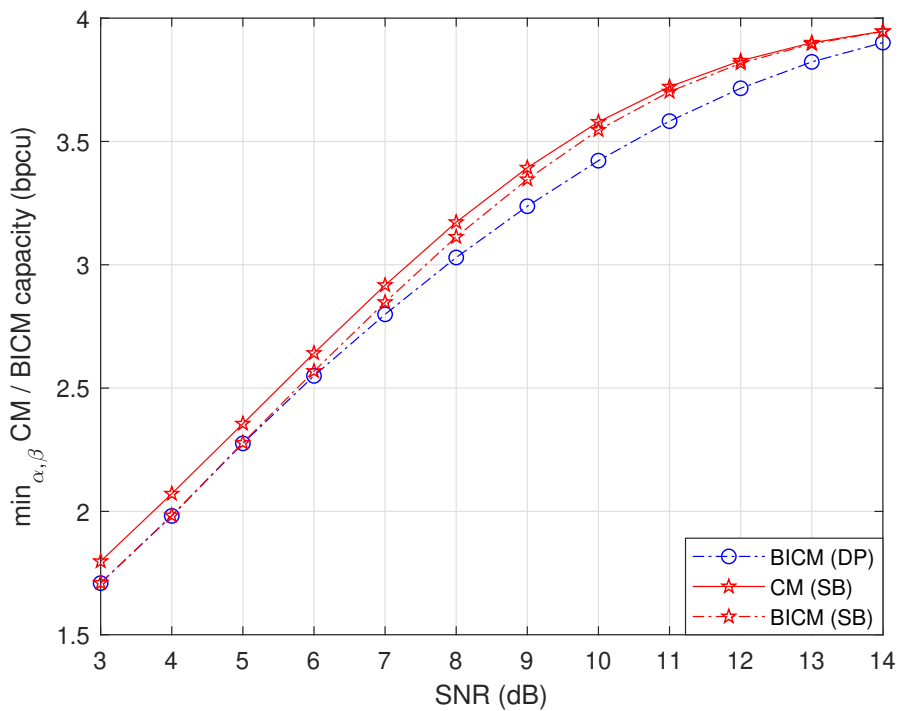


FIGURE 3.7: Worst CM and BICM rates for the SB and DP schemes as a function of SNR for  $\Lambda = 6$  dB.

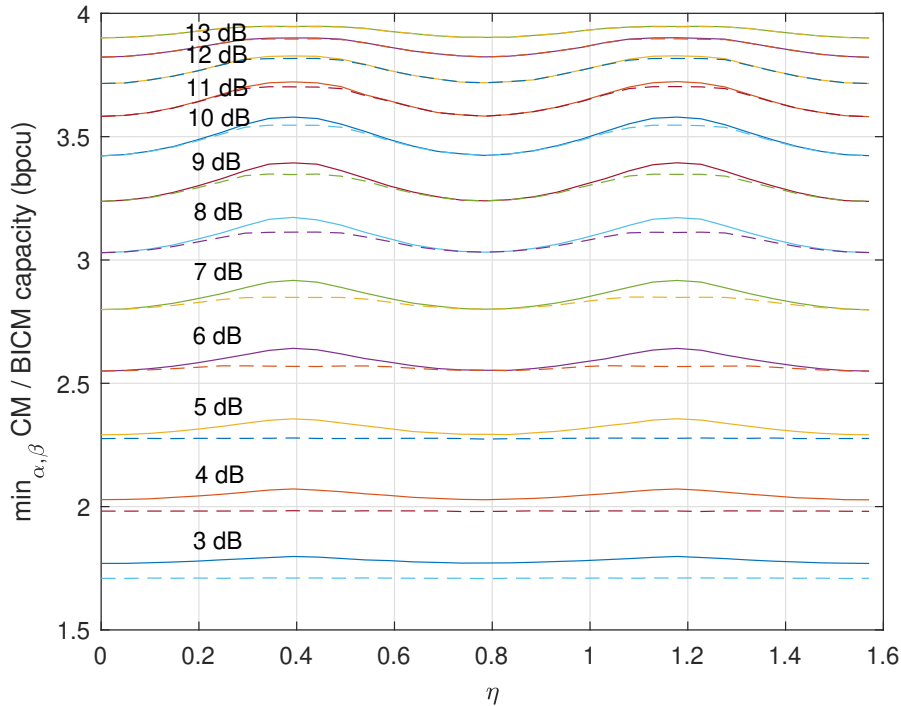


FIGURE 3.8: SB's worst CM and BICM rates as a function of  $\eta$  at different SNRs for  $\Lambda = 6$  dB (the solid and dashed lines represent the CM and BICM capacities, respectively).

### 3.3.2 Worst BICM and SICM Optimization in the NSB

We study the variation of the QPSK-CM, QPSK-BICM, and QPSK-SICM rates for the NSB scheme where we take  $\nu = \pi/4$ ,  $\eta \in [0, \pi/2]$  with a  $\pi/64$  precision and  $(\alpha, \beta) \in [0, \pi] \times [0, \pi]$  with a  $\pi/32$  precision. We can see from Fig. 3.9 that the minimum and the maximum of the QPSK-CM rate correspond to the pairs  $(\alpha, \beta) = (0, 0)$  and  $(\alpha, \beta) = (\pi/4, \pi/8)$ , respectively. This indicates that the CM, BICM, and SICM have identical optimal parameters for NSB polarization. However, at low rates, for example, at 6 dB SNR, as shown in Fig. 3.10, the pairs  $(\alpha, \beta)$  for the minimum and the maximum, are not the same compared to the CM scheme, for both the BICM and SICM capacities. This difference in behavior between the CM, BICM, and SICM rates lies in the fact that bit correlations occur at low rates due to the employed mapping.

Moreover, like the SB signaling, the NSB's worst BICM rate is not better than that of the non-precoded case (DP) for low SNR ranges, as shown by Fig. 3.11. Hence, considering the encoding function  $\mathbf{f}_{\eta, \nu}$  for those ranges is unnecessary.

In Fig. 3.12, we compare the behavior of the CM and BICM rates as a function of  $\eta$  and  $\nu$ , at 6 dB SNR, with taking  $(\eta, \nu) \in [0, \pi/4] \times [0, \pi/4]$ . As a result,

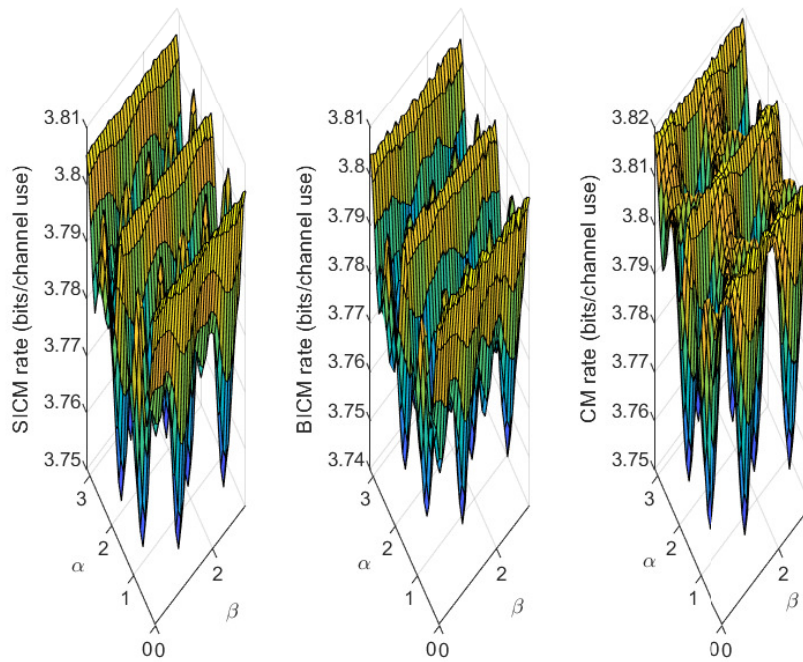


FIGURE 3.9: NSB-QPSK CM, BICM and SICM as a function of the two angles  $\alpha$  and  $\beta$  for  $\Lambda = 6$  dB at an SNR of 11 dB.

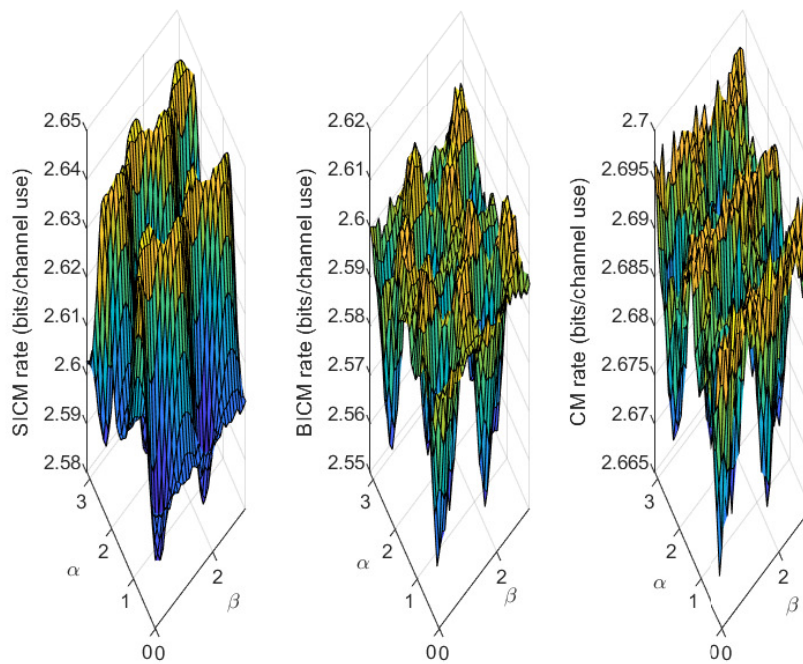


FIGURE 3.10: NSB-QPSK CM, BICM and SICM as a function of the two angles  $\alpha$  and  $\beta$  for  $\Lambda = 6$  dB at an SNR of 6 dB.

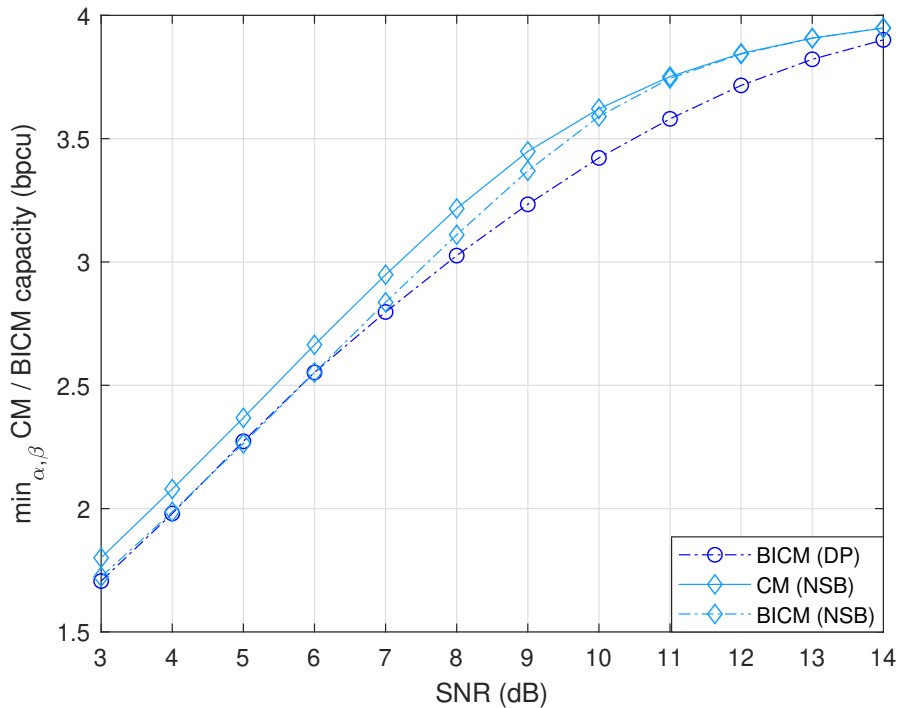


FIGURE 3.11: Worst CM and BICM rates for the NSB and DP schemes as a function of SNR for  $\Lambda = 6$  dB.

we can see that the optimal pair  $(\eta_{\text{opt}}, \nu_{\text{opt}})$  that maximizes the NSB's worst BICM rate is not the same for the NSB's worst CM rate. This is because there are two optimal pairs for the BICM scheme, whereas only one is for the CM scheme. Also, it is well-observed in Fig. 3.12 that there is not a significant evolution of the NSB's worst BICM rate as a function of  $\eta$ . Consequently, we think that whatever the chosen value of the angle  $\eta$ , we have to choose precisely the value of the angle  $\nu$ .

All the obtained performance is evaluated on the QPSK modulation format, but the work is also well-founded for M-QAM modulation formats. For example, Fig. 3.13 shows that significant SNR variations are observed as a function of the incident angle  $\alpha$  for 16-QAM where  $\beta = 0$ . In Fig. 3.14, we see the equivalent variation in  $\alpha$  for SNR = 18 dB. Also, it is well-observed that the SB scheme improves the worst MI of the non-precoded scheme, which is realized for  $\alpha \in \{0, \pi/2, \pi\}$ . Before concluding this chapter, we should mention that the same results concerning the CM, BICM, and SICM capacities are obtained for the 16-QAM, like the QPSK modulation format.

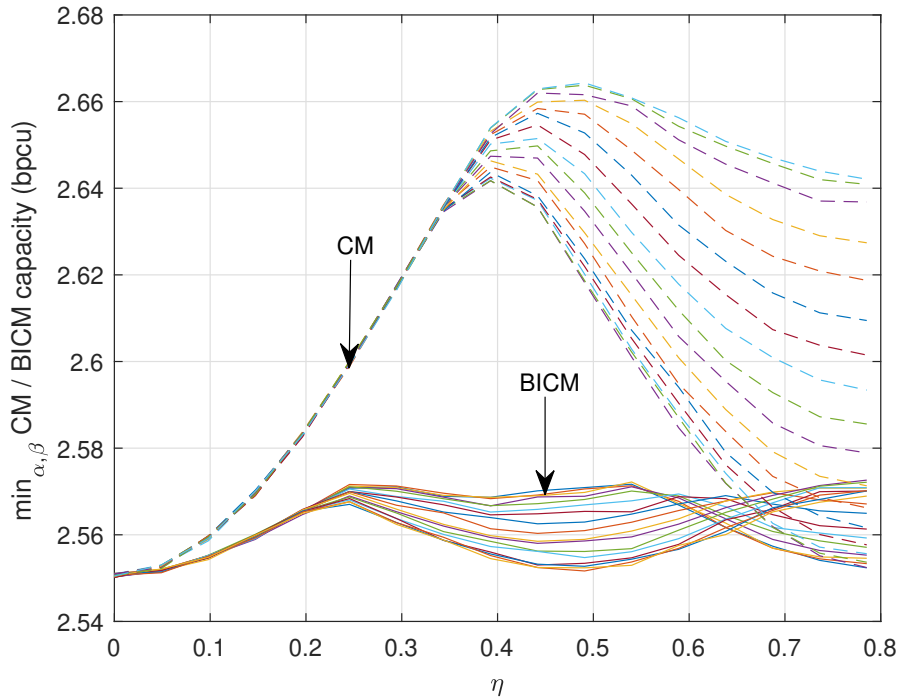


FIGURE 3.12: NSB’s worst CM and BICM rates as a function of  $\eta$  and  $\nu$  for  $\Lambda = 6$  dB at an SNR of 6 dB.

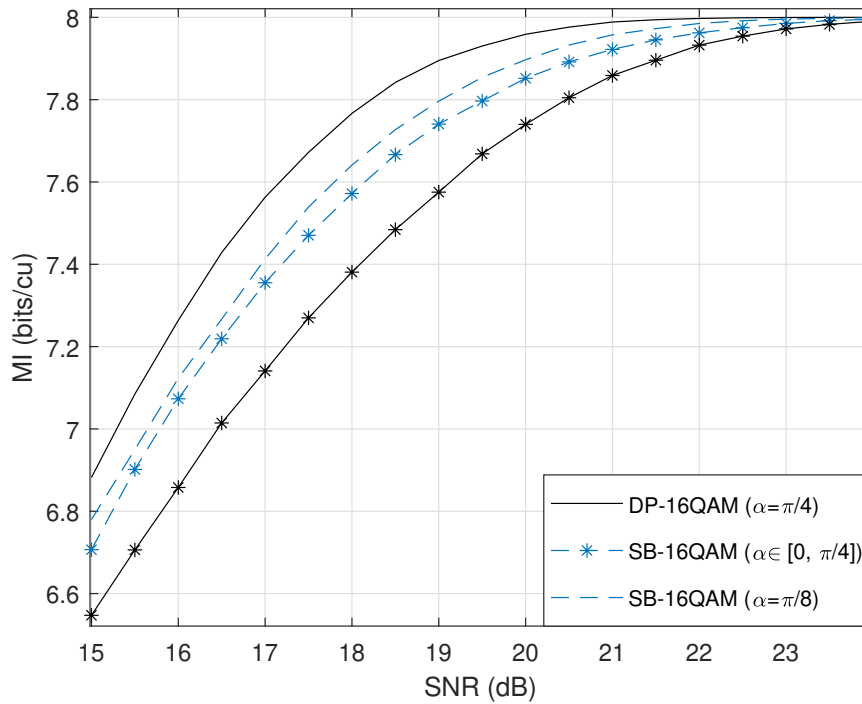


FIGURE 3.13: DP-16QAM and SB-16QAM MI in a 6dB-PDL channel as a function of SNR

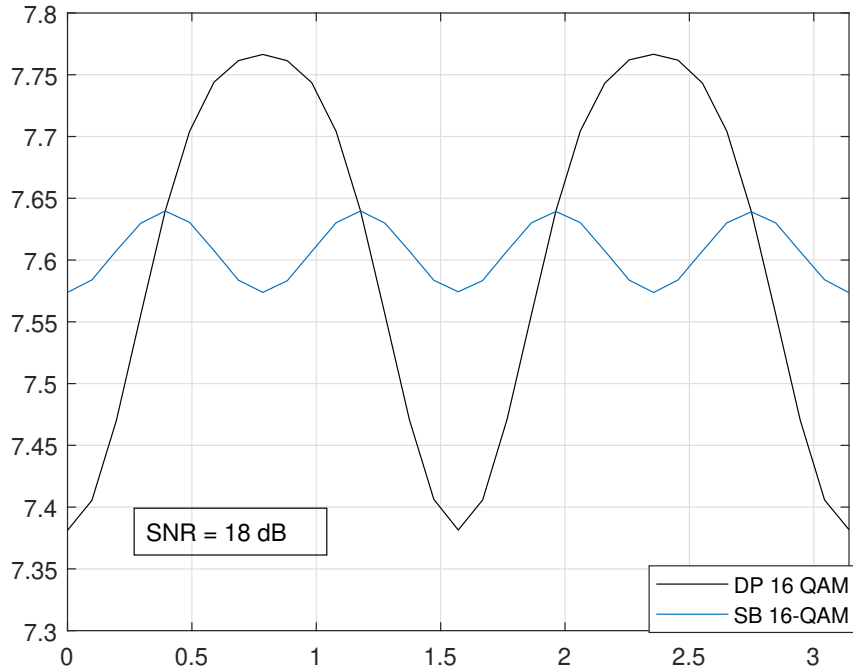


FIGURE 3.14: DP-16QAM and SB-16QAM MI in a 6dB-PDL channel as a function of SNR

### 3.4 Binary PAS for the Optical Channel

QAM modulations are usually deployed in modern optical transport networks. However, an asymptotic loss of almost 1.53 dB can be observed towards the Shannon limit [76]. Such a gap can be closed in information theory by shaping when the modulation format follows a Gaussian distribution. In recent years, several works concerning optical transmissions have successfully implemented different shaping techniques, from many-to-one and geometrically-shaped formats to PS [14–16, 77, 78]. In this context, many transmission demonstrations and record experiments with shaped modulations have been reported, e.g., in [19, 79–85]. This section considers the optical  $2 \times 2$  MIMO channel as described earlier. We aim to generate an optimized non-uniform distribution of information symbols for QAM modulations to be transmitted using binary LDPC encoding. Associating the information symbols (amplitudes) with the parity bits creates the desired symbols to be sent via the optical MIMO channel. The communication system is depicted in Fig. 3.15, which combines binary PAS and binary channel encoding. We employ QAM modulations representing the constellations of choice in various communication systems. QAM enables natural Gray labeling of the information bits, which increases performance at

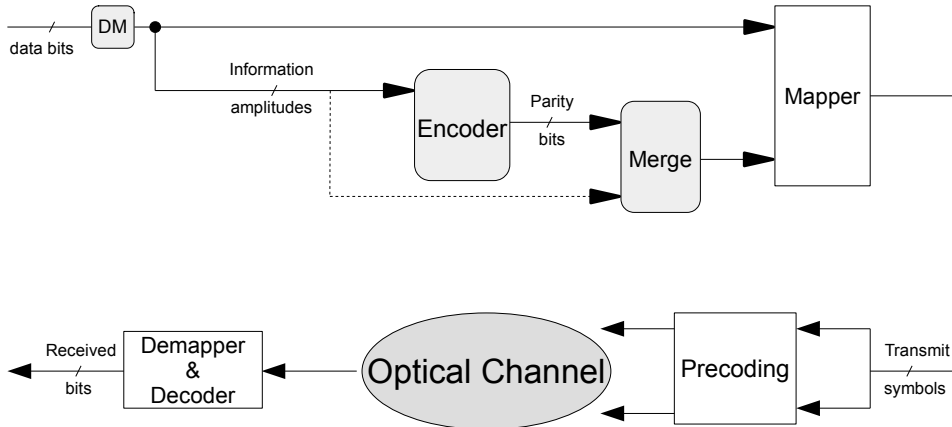


FIGURE 3.15: Optical communication system with binary PAS.

mid-to-large SNRs.

We consider binary LDPC encoding for simulations to generate uniformly distributed parity bits, representing the sign bits described in [14]. In this context, a DM converts the binary data to symbols representing the amplitudes the binary LDPC encoder will encode. The parity bits after encoding are distributed uniformly, although the input bits to the LDPC encoder follow a non-uniform distribution. At last, the final transmit signal is obtained after associating the information amplitudes with the parity bits generated by the binary LDPC encoding. Then, the transmission is realized over the PDL channel. Finally, the received signals are demodulated at the receiver to form binary probabilities fed to the binary LDPC decoder.

We evaluate the performance of the PS scheme by Monte Carlo simulations. The system performance depends on the considered transmission scheme. Therefore, we have tested the implementation of the following schemes:

- **DP uniform:** there is no precoding applied  $(\eta, \nu) = (0, 0)$ , and the transmit symbols are uniformly distributed;
- **DP PS:** there is no precoding applied  $(\eta, \nu) = (0, 0)$ , and for each SNR, we search the distribution  $P_A^*$  that maximizes the outage capacity;
- **SB uniform:** we fix  $\nu$  equal to zero and we consider  $\eta \in [0, \pi/2]$  with a  $\pi/64$  precision. Then, for each SNR, we search the optimal value  $\eta^*$  that maximizes the outage capacity;

- **SB PS** : we fix  $\eta^*$  to the found value in the SB uniform; then we search for each SNR the distribution  $P_A^*$  that maximizes the outage capacity  $\implies$  non-joint optimization for the SB non-uniform;
- **NSB uniform**: we consider  $(\eta, \nu) \in [0, \pi/2] \times [0, \pi/2]$  with a  $\pi/64$  precision, then, for each SNR, we search the optimal pair  $(\eta^*, \nu^*)$  that maximizes the outage capacity;
- **NSB PS** : we fix  $\eta^*$  and  $\nu^*$  to the found values in the NSB uniform; then for each SNR, we search the distribution  $P_A^*$  that maximizes the outage capacity  $\implies$  non-joint optimization for the NSB non-uniform;

The precoding process is performed first for all schemes, i.e., before the shaping optimization. Hence, no joint processing is applied, which has the advantage of reducing the greedy procedure complexity.

The simulation results show that the non-uniform distribution of the transmit sequence allows for increasing the throughput of the already deployed fiber schemes, DP, SB, and NSB. We plot in Fig. 3.16 the achievable CM capacity of the different schemes when employing the 64-QAM modulation. It is well observed that PS achieves relative performance in all schemes. What is clear is that the performance of non-uniform schemes is always better than that of uniform designs. For instance, in the NSB scheme, the gain is almost 0.5 dB for high SNRs (corresponding to rates between 0.8 and 0.85). Besides, we can see the advantage of integrating the precoding and the PS to enhance capacity. For instance, we can see almost 1.5 dB gain achieved by the NSB PS over the uniform DP. However, it is well-observed that precoding does not bring profits at low-to-moderate SNRs. By comparing the uniform DP and the uniform SB and NSB schemes, we observe that their performances are almost similar when the SNR regions are upper-bounded by 16 dB. In contrast, PS improves the capacity, which indicates that PS is more competent than precoding, especially for low-to-moderate SNRs. For example, we can see that the DP PS achieves the best performance compared to the uniform SB and NSB schemes when the SNR is less than 20 dB. We briefly summarize the analysis above and list in Table 3.1 the optimal schemes in specific SNR regions. The hatched cells indicate that the corresponding designs are not included for comparison. We can conclude from the Table results that the precoding process does not improve performance for some SNR regions and is only effective at high SNR levels. Conversely, PS always enhances the system performance even at low SNRs, showing that it is more beneficial at some target rates.

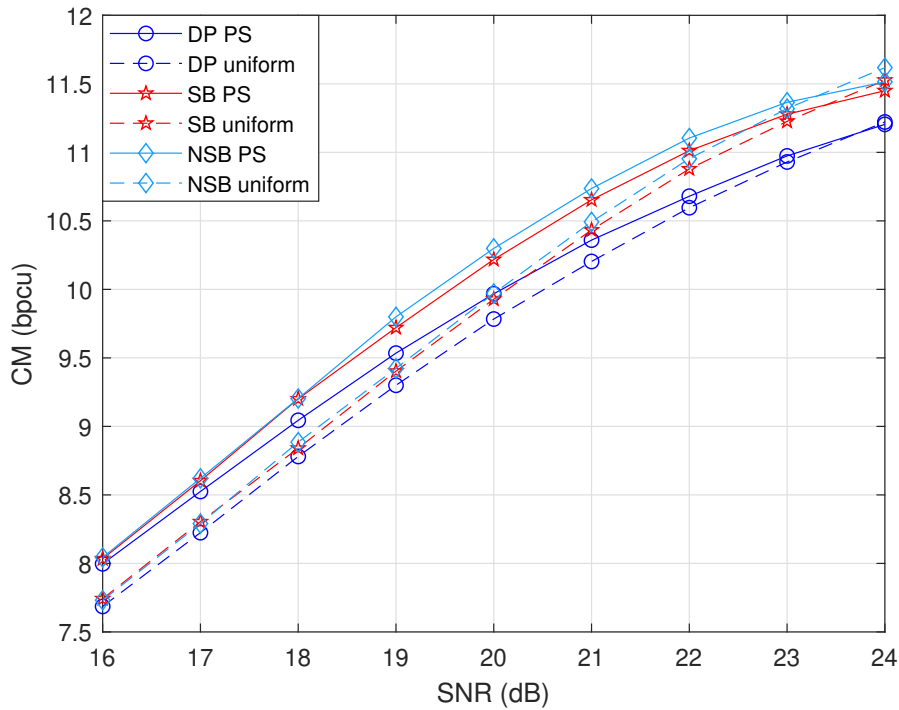


FIGURE 3.16: CM performance of different schemes when using QAM signals.

We may refer to the SICM that represents the achievable rate associated with the conventional estimation of the representative symbol for practical systems. Fig. 3.17 shows the achievable SICM capacities of the different schemes when employing the 64-QAM modulation. Results illustrate again the advantage yielded by applying PS. Also, it is displayed that the DP scheme with PS is efficient at low-to-moderate SNRs, and the NSB scheme with PS achieves almost 0.5 dB gain for high SNRs compared to the DP scheme with uniform distribution.

### 3.5 Non-binary Coding for Optical MIMO

This section deals with the optical  $2 \times 2$  MIMO channel, as described in detail in the preceding sections. Two new approaches based on non-binary information processing have been tested : (i) the design of protograph non-binary codes under the NSB framework and (ii) the design of a SICM based on non-binary protograph LDPC codes.

TABLE 3.1: Optimal shaping schemes in the PDL channel.

SNR (dB)	DP		SB		NSB	
	uniform	PS	uniform	PS	uniform	PS
$\forall$ values	$\times$	$\checkmark$				
			$\times$	$\checkmark$		
					$\times$	$\checkmark$
$< 20$	$\times$	$\checkmark$	$\times$		$\times$	

### 3.5.1 CM Schemes

The first scheme to be considered is a CM scheme based on non-binary LDPC codes for which the field order is directly mapped to the MIMO symbol dimension. Non-binary LDPC codes have been widely studied for high-order modulation in the AWGN channel with optical signals. [22, 81, 86–89]. Our work investigates the design of non-binary protograph LDPC codes suited for the multi-dimensional mapping naturally induced by the NSB precoding. Assume  $q = M^{N_t}$  where  $M$  is the constellation size, and  $N_t$  is the number of transmitting antennas. We consider a simple CM scheme using a  $q$ -ary LDPC error correcting code, i.e., a code defined using a sparse parity-check matrix whose non-zero coefficients belong to the GF of order  $q$ , denoted GF( $q$ ). For this scheme, an information sequence  $\mathbf{u}$  consisting of  $K$  symbols is encoded first into a codeword vector  $\mathbf{c}$  of length  $N$ , defining a code of design rate  $R = K/N$ . Then, each code symbol  $\mathbf{c}_n$ ,  $n \in \{1, \dots, N\}$ , is mapped into  $\mathbf{x}_n = [\mathbf{x}_{n,1}, \mathbf{x}_{n,2}]^T$ . Here, we consider a multi-dimensional mapping where each code symbol  $\mathbf{c}_n$  is first converted into its binary representation of length  $\log_2(q)$  bits. Then, each successive  $\log_2(q)/2$ -tuples of bits is used to assign an  $M$ -QAM symbol on each dimension of the MIMO symbol. In this context, a Gray mapping rule is considered for a fair comparison with the BICM case. Finally, the obtained code symbol  $\mathbf{x}_n$  is precoded into  $\tilde{\mathbf{x}}_n = \mathbf{f}_{\eta,\nu}(\mathbf{x}_n)$  and sent over the optical MIMO channel. At the receiver, observation vectors are used to compute likelihood functions that will feed the soft input of the non-binary LDPC decoder. We use the fast-Fourier transform (FFT) based belief propagation (BP) decoding assuming  $L$  decoding iterations [51, 90].

For the optimization, we consider non-binary protograph LDPC codes [55, 58,



allows operating at 0.03 dB from the precoded multi-dimensional AWGN channel capacity. When considering punctured/precoded graphs, we found that

$$H_{B_2} = \begin{bmatrix} 2 & 1 & 1 & 1 & 1 & 1 & 1 & 1 & 1 & 1 & 0 \\ 1 & 1 & 1 & 1 & 1 & 1 & 1 & 1 & 1 & 1 & 0 \\ 2 & 1 & 0 & 0 & 0 & 0 & 0 & 0 & 0 & 0 & 1 \end{bmatrix} \quad (3.18)$$

gives a threshold only within 0.01 dB from the capacity. The first column corresponds to the variable punctured nodes. As often for non-binary coding schemes operating close to the capacity, the corresponding capacity-approaching graphs tend to have many variable nodes of 2 degrees. This can be detrimental to finite length performance if no optimization of non-binary coefficients is performed. However, a denser graph with better graph properties can generally perform far away from the capacity, which can cancel the benefit of a non-binary scheme over the BICM one. For example, for  $R = 0.8$ , regular  $(3, 15)$  protograph codes and irregular repeat accumulate (IRA) based protograph codes following DVB-S2 profile [92] have a threshold of 0.44 dB and 0.39 dB respectively away from the capacity for codes over  $\text{GF}(16)$ .

### 3.5.2 BICM/SICM Schemes

The second scheme is a generalization of the BICM scheme to higher field orders, referred to as SICM. It is a different sub-optimal approach to reducing the CM complexity. Several SICM schemes can be considered by assigning different values to  $q$  such that  $1 \leq \log_2 q \leq m$ , with  $M = 2^m$ ,  $m \in \mathbb{N}$ , and  $q$  divides  $m$ . The SICM transmitter involves a serial concatenation of a  $q$ -ary LDPC code, a symbol interleaver, and an  $M$ -ary QAM mapper. An LDPC code over  $\text{GF}(q)$ , of a rate  $R = K/N$  encodes an information sequence  $\mathbf{u}$  of  $K$  symbols into a codeword  $\mathbf{c}$ . The coded symbols are then interleaved using a symbol interleaver and grouped into  $l$ -tuples of symbols over  $\text{GF}(q)$  where  $l = m/\log_2 q$ . We note with  $\underline{\mathbf{c}}_k = [\underline{\mathbf{c}}_{k,1}, \underline{\mathbf{c}}_{k,2}, \dots, \underline{\mathbf{c}}_{k,l}]$  the sequence of non-binary  $l$ -tuples for  $1 \leq k \leq N/l$ . Finally, the mapper associates to each  $l$ -tuple  $\underline{\mathbf{c}}_k$  a complex symbol  $\mathbf{x}$ . Here, we consider  $q = M$  and a Gray mapping based on the binary representation of the coded symbols. The resulting  $M$ -QAM symbols are then demultiplexed and precoded before being sent through the optical MIMO channel. The SICM receiver, in turn, involves a serial concatenation of a soft MIMO detector/demapper, a symbol desinterleaver, and a soft-input  $q$ -ary FFT-BP decoder. By applying the same methodology as for the CM case, considering the symbol-based marginalization, we have optimized non-binary protograph

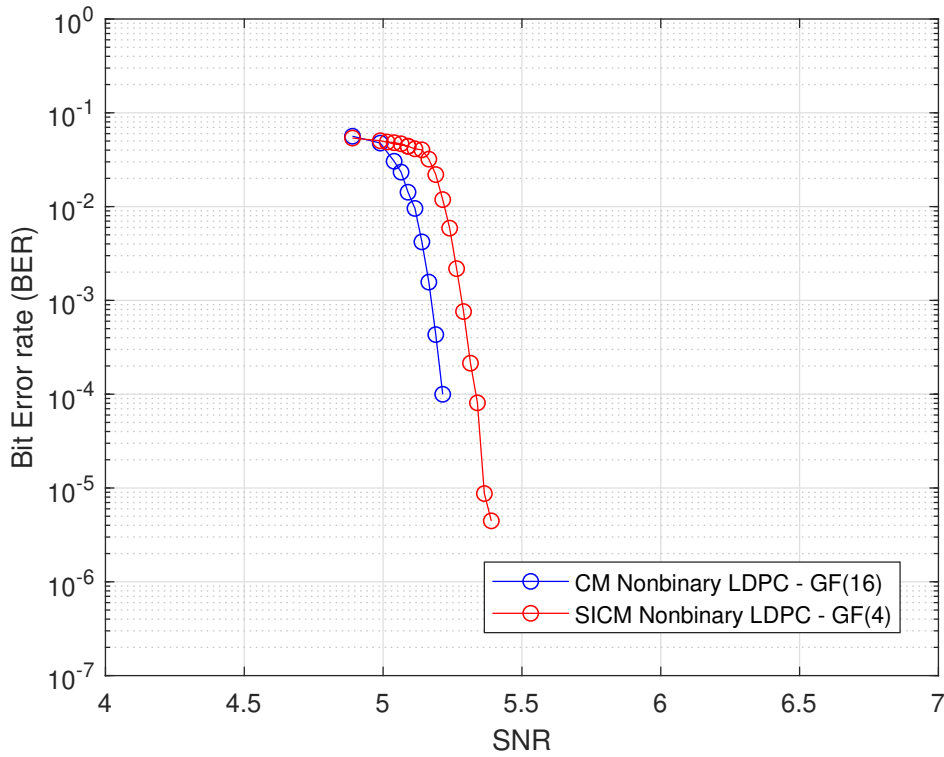


FIGURE 3.18: BER versus SNR for protograph based codes using  $H_{B_1}$  and  $\tilde{H}_{B_1}$ .

LDPC codes. For example, considering QPSK modulation and a code defined over GF(4), we obtain the following unpunctured protograph code,

$$\tilde{H}_{B_1} = [6 \ 3 \ 2 \ 2 \ 2]. \quad (3.19)$$

For the punctured case, we obtain

$$\tilde{H}_{B_2} = \begin{bmatrix} 3 & 1 & 1 & 2 & 1 & 2 & 1 & 1 & 1 & 1 & 0 \\ 1 & 1 & 2 & 1 & 2 & 1 & 1 & 1 & 1 & 1 & 0 \\ 2 & 1 & 0 & 0 & 0 & 0 & 0 & 0 & 0 & 0 & 1 \end{bmatrix}, \quad (3.20)$$

which is 0.08 away from capacity. The first column corresponds to the punctured variable nodes.

In Fig. 3.18, we give some BER results for the worst-case MIMO channel for the two described schemes (CM and SICM) for codewords of length 61440 bits. We can operate close to the CM ZOC for the CM scheme, while the SICM scheme operates only close to the SICM ZOC.

## 3.6 Conclusion

In this chapter, we have presented studied PDL-resilient signaling. An optimal four-dimensional modulation is developed in the literature. We first tested the SB signaling with a single PDL element to observe the performance. The latter showed an increase in the worst encountered rate. Also, we have tested the NSB signaling that offered rate increases. However, the optimization techniques are only performed to maximize the minimal CM capacity. Therefore, we have optimized the BICM and SICM capacities to find the optimal parameters that maximize their minimal capacities. We have found that the behaviors of BICM and CM capacities are different in low-to-moderate SNR regions but are similar in high SNR levels. However, we have noticed that CM and SICM capacities behaviors are the same in the entire SNR region.

Furthermore, we have shown the advantage yielded by PS when employed in the optical channel. It outperforms the precoding process for low-to-moderate SNRs and significantly increases the performance in terms of achievable rates. We have also studied the design of non-binary protograph LDPC codes for precoded optical MIMO transmissions. Results show that we can design satisfying codes operating close to the zero-outage capacities. Finally, for perspectives, we can consider the design of efficient non-binary spatially-coupled schemes enabling both good finite-length performance and suitable thresholds for the MIMO case.

## Chapter 4

# Circular QAM Signals and Non-binary Coding

### 4.1 Introduction

Commonly QAM constellations are usually deployed in modern transport networks thanks to their efficiency of generation and detection. However, these modulations realize an asymptotic loss of almost 1.53 dB towards the Shannon limit [76]. Such a 1.53 dB gap can be closed using constellation shaping, which is becoming the last resort to approach channel capacity since channel coding has reached its maturity [93]. Two strategies can be used to achieve that goal; PS or GS techniques [17,33,41,43,94]. Compared to regular modulation formats (with equal probability), the constellation points with PS are sent with different probabilities, usually following an MB distribution [42] that intends to maximize the shaping gain. The invention of PAS was an important achievement for making PS efficient [14]. On the other hand, more classical GS techniques allow non-equidistant constellation distribution over Euclidean space. Although PS and GS differ, they usually mimic a quantized sampled Gaussian distribution to approach the Shannon limit with finite dimensions.

Many approaches to building a capacity-approaching codebook exist in the literature. For instance, authors in [37] proposed a non-uniform constellation on the real line with a uniform probability distribution. Méric brought their approach to the complex plane in [95]. Also, authors in [96] built a codebook which is a real geometrically non-uniform Gaussian-like constellation, and it achieves channel capacity when the number of points goes to infinity. Another recent approach in [16] consisted of building  $p^2$ -CQAM constellations that allow to directly generalize PAS to finite fields  $\mathbb{F}_p = \{0, 1, \dots, p-1\}$ . PS shows a

small gap in the capacity; however, a complex DM, e.g., [15, 97], is required to modify the source distribution.

In this work, inspired by the analysis of existing GS techniques on the complex plane, we propose the construction of  $(c, p)$  CQAM constellations with equiprobable signaling that can approach the Gaussian capacity. The constellation design splits the points into  $c$  circles, each containing  $p$  points uniformly distributed. Compared to existing approaches where  $c = p$ , we can find parameters allowing us to get closer to the capacity for uniform inputs. For the proposed GS design, we propose non-binary protograph LDPC codes to optimize the asymptotic convergence threshold and operate so close to the channel capacity.

## 4.2 From Gaussian Shaping to CQAM Signals

In this section, we compare Gaussian-shaped constellations that are proved efficient as the order of the constellation tends to infinity. If several approaches have been proposed, we intend to link these strategies and provide some links to the newly introduced CQAM [16]. For Gaussian shaping, we can mainly adopt two approaches. The first is to build a two-dimensional  $M$ -ary constellation as the Cartesian product of two Gaussian-shaped  $\sqrt{M}$ -ary PAM constellations. Hence, we refer to these constellations as GS-QAM. The second is to consider the extension of the Gaussian shaping directly in the complex plane, which results mainly in APSK-like modulations. Hence, we refer to these constellations as GS-APSK. Finally, we link existing GS-APSK constellations to the more general family of circular QAMs.

### 4.2.1 GS-QAM Signals

GS-PAM signals have often been studied in the literature, e.g., [37, 50, 96]. In [96], Boutros *et al.* propose a real geometrically non-uniform Gaussian-like constellation  $\mathcal{G}$ , referred to as GS-PAM, associated to  $q$ -ary codes defined over the ring  $\mathbb{Z}_q$ . When the constellation cardinality is equal to  $q = \sqrt{M}$ , the construction can be summarized as follows:

- Let  $\mathcal{U}$  be a discrete set of  $q$  equidistant points in the interval  $[0, 1]$  such that  $\mathcal{U} = \{u_0, u_1, \dots, u_{q-1}\}$ , and we have  $u_i = \frac{1}{2q} + \frac{i}{q}$ , for  $i = 0 \dots q - 1$ ;
- We denote by  $s \in \mathbb{Z}_q = \{0, 1, 2, \dots, q - 1\}$  the symbol from the uniform  $q$ -ary information input. At first, the symbol  $s$  is mapped into a point

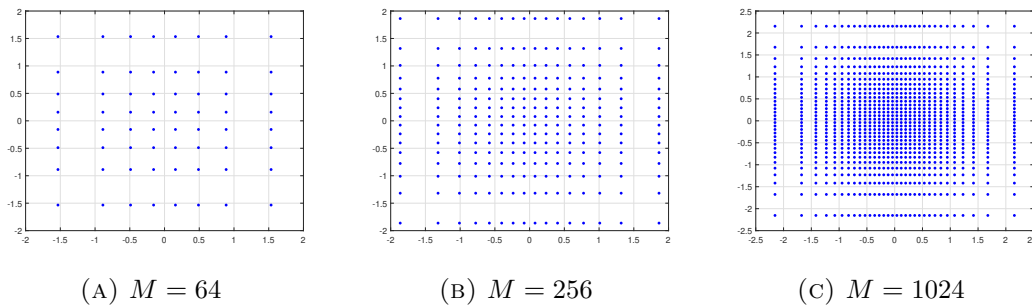


FIGURE 4.1: Three different GS-QAM.

given by

$$u(s) = \frac{1}{2q} + \frac{(s + \lfloor q/2 \rfloor) \bmod q}{q}. \quad (4.1)$$

Then, the point  $u(s)$  is mapped into a point  $x(s) = \phi^{-1}(u(s)) \in \mathcal{G}$  where  $\phi^{-1}(u)$  is the inverse of the well-known distribution function of a zero-mean unit-variance real Gaussian random variable.

Authors have proved that their discrete codebook  $\mathcal{G}$  achieves the channel capacity when the number of points  $q$  tends to infinity. One can bring their approach to the complex plane to get the two-dimensional (2D) constellation of size  $M = q \times q$ . As the constellation of the M-QAM can be expressed as the Cartesian product of two PAM constellations, we can construct the GS-QAM constellation from the discrete codebook  $\mathcal{G}$ . For example, the coordinates of the obtained GS-QAM points are illustrated in Fig. 4.1 for different constellation sizes  $M = 64$ , 256, and 1024.

### 4.2.2 GS-APSK Signals

APSK constellations are an important family of constellations. For instance, some practical systems, such as the DVB standards, implement APSK constellations with large cardinality, up to 256 [92]. In this context, [95] presents a 2D generalization of [37] building GS-APSK constellations that can achieve the Gaussian capacity as the constellation size goes to infinity. It is based on the same sampling as in [96] but applied to the complex plane. By considering two random variables  $U_m$  and  $V_m$ ,  $m \geq 1$ , uniformly distributed on

$$\left\{ \frac{1}{2m} + \frac{k}{m} \mid 0 \leq k \leq m-1 \right\}, \quad (4.2)$$

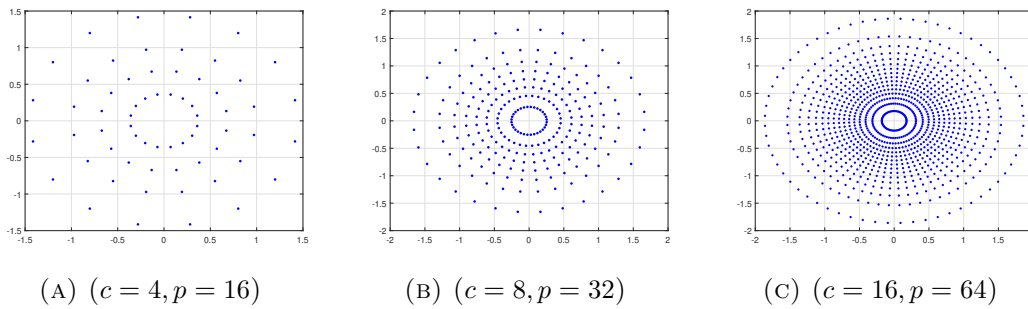


FIGURE 4.2: Three different GS-APSK.

and the following mapping  $\varphi : (0, 1)^2 \rightarrow \mathbb{R}^2$  defined as

$$\varphi(x, y) = \left( \sqrt{-P \log_e x} \cos(2\pi y), \sqrt{-P \log_e x} \sin(2\pi y) \right), \quad (4.3)$$

the vector  $W_m = \varphi(U_m, V_m)$  is a random vector uniformly distributed on a set  $\mathcal{C}_m$  of  $m^2$  points in  $\mathbb{R}^2$ . Thus, it consists of splitting the points on  $c = m$  circles where each circle contains  $p = m$  points uniformly distributed. This scheme will be referred to as  $(c = m, p = m)$  GS-APSK of size  $M = m^2$ . However, a better construction is achieved by considering a slightly different sampling strategy [95]. In this latter case,  $m$  being a power of 2,  $\mathcal{U}_m$  and  $\mathcal{V}_m$  are the two sets defined as

$$\mathcal{U}_m = \left\{ \frac{1}{m} + \frac{2k}{m} \mid 0 \leq k \leq \frac{m}{2} - 1 \right\}, \quad (4.4)$$

and

$$\mathcal{V}_m = \left\{ \frac{1}{4m} + \frac{k}{2m} \mid 0 \leq k \leq 2m - 1 \right\}. \quad (4.5)$$

The resulting shaping involves  $c = m/2$  circles, and each circle has  $p = 2m$  points uniformly spaced. This scheme will be called  $(c = m/2, p = 2m)$  GS-APSK scheme. An illustration of different GS-APSK constellation points is shown in Fig. 4.2. For instance, note that the  $(c = 4, p = 16)$  GS-APSK can be further extended to design a constellation with parameters  $(c = 16, p = 4)$ . This configuration is not reported here, as it does not lead to an exciting modulation in achievable capacity. However, these parameters will enable the design of efficient CQAM modulations.

### 4.2.3 Achievable Capacities

As an illustration, we compare the different CM capacities for constellation sizes  $M = 64$  and  $M = 256$ . As shown in Fig. 4.3, GS-APSK constellations can achieve better CM capacity than GS-QAM modulations for some range of

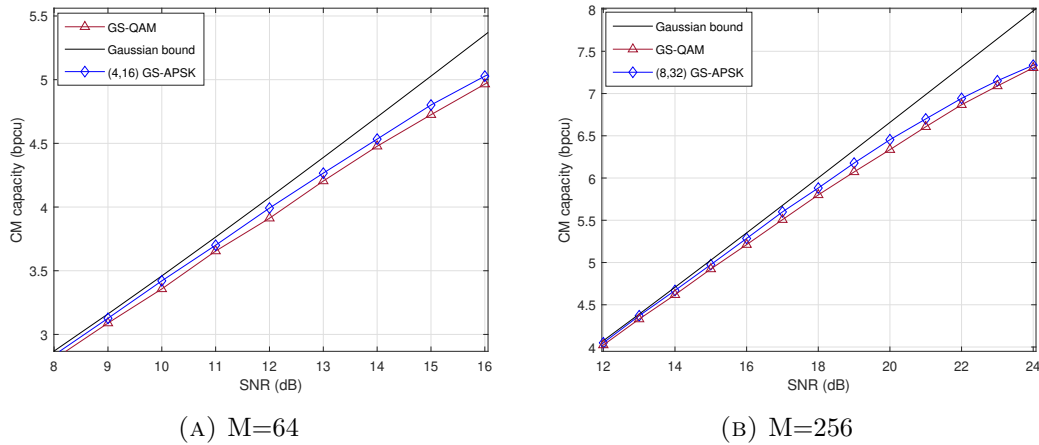


FIGURE 4.3: Comparison between the GS-QAM and GS-APSK

SNRs. For instance, the GS-APSK achieves almost 0.3 and 0.4 dB gains for  $M = 64$  and  $M = 256$ , respectively. However, GS-QAM signals have the advantage of having independent real and imaginary parts, which enables achieving the corresponding CM capacity by considering non-binary coding schemes defined on an alphabet of order  $\sqrt{M}$ . This is not the case for APSK signals, and careful constellation labeling should be chosen to limit the loss. We compare the different CM capacities [20, 98] of the GS-QAM and the (4, 16) GS-APSK following a mapping as suggested by [92]. Despite the loss of information induced by marginalization over a smaller alphabet, it shows that there is still an advantage of GS-APSK over the GS-QAM. Note that we can fill the GS-APSK CM capacity gap by considering iterative detection and decoding at the price of increased decoding complexity.

#### 4.2.4 Link to Existing Shaping Strategies

We can link the GS-APSK to the newly introduced CQAM [16]. Indeed, GS-APSK signals can be viewed as STAR-like constellations, i.e., rotated GS-PAM signals. For example, the (4, 16) GS-APSK can be described as an 8-ary rotated GS-PAM. The (8, 8) GS-APSK constellation is a particular instance of the (8, 8) CQAM, viewed as a 16-ary rotated GS-PAM. It is always the same interpretation for a higher modulation order. For instance, the (8, 32) GS-APSK can be defined as a 16-ary rotated GS-PAM, and the (16, 16) GS-APSK is a particular case of the (16, 16) CQAM, observed as a 32-ary rotated GS-PAM. Fig. 4.4 illustrates the above analysis for two different GS-APSK constellations: ( $c = 4, p = 16$ ) and ( $c = 8, p = 32$ ). However, it is interesting to note that the resulting Gaussian shapings of the underlying PAMs do not lead to the one

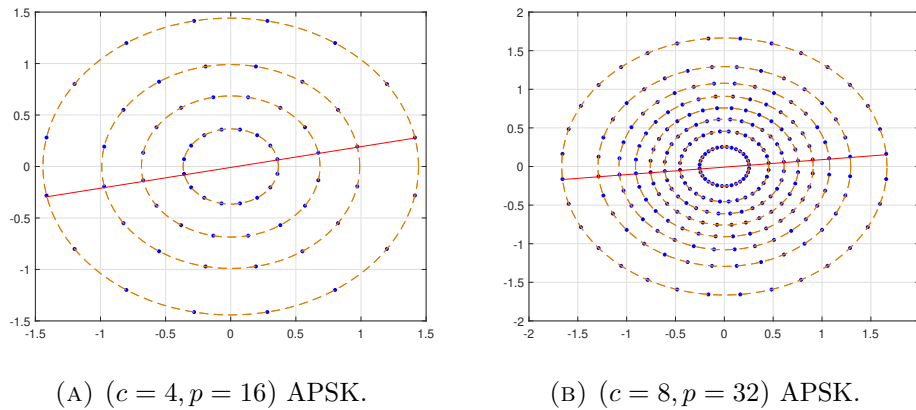


FIGURE 4.4: GS-APSK observed as rotated GS-PAM.

given by [96] due to the different sampling strategies. It has been shown in [98] for the  $(p, p)$  case that careful design of the CQAM can lead to improved performance. These observations show that some capacity gains can be obtained in the case of the uniform input by generalizing the  $(p, p)$  CQAM approach to a  $(c, p)$  CQAM for a given order of modulation  $M = c \times p$ . This is the purpose of the next section. We will also address the question of possible further improvements by applying PS with these new configurations.

### 4.3 $(c, p)$ -Circular QAM Signals

#### 4.3.1 $(p, p)$ CQAM

Boutros *et al.* propose in [16] a novel approach based on tiling triangles to make a circular bi-dimensional constellation for both GS and PS, referred to as CQAM constellation (see the extension in [99]). They define a  $p^2$ -CQAM constellation as a rotation-invariant circular QAM format in the I/Q plane. The  $p^2$ -CQAM is a two-dimensional constellation that includes  $p$  circles containing points of the same amplitude, referred to as shells, with  $p$  points per shell. We can write

$$p^2\text{-CQAM} \propto \cup_{i=0}^{p-1} e^{i\frac{2\pi}{p}\sqrt{-1}i} B, \quad (4.6)$$

where  $B$  is a whole (connected or not) discrete set of  $p$  points with distinct amplitudes. Based on the design criteria, many  $p^2$  CQAM constructions are possible, and different properties and performances are obtained. Fig. 4.5 shows several CQAM like examples [98]. A construction criterion permits control spacing and phase offset between shells. The selection of a particular criterion may be motivated by geometric considerations. It may also be combined with the

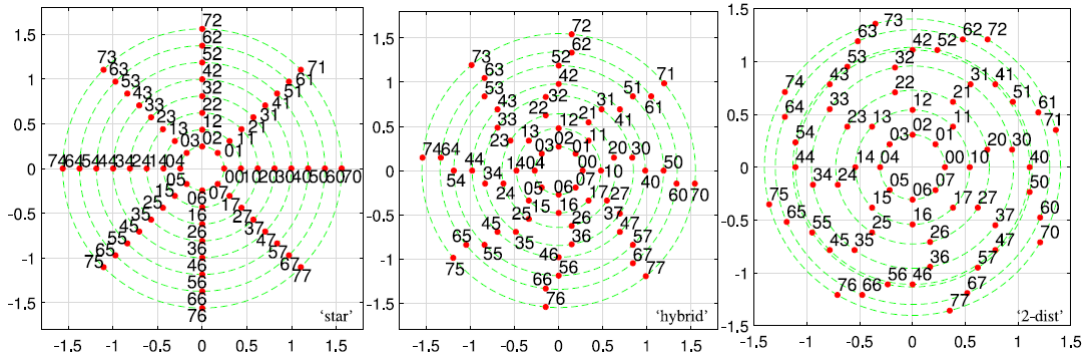


FIGURE 4.5: Types of CQAM-like constructions [98].

further optimization of the transceiver design at a given target SNR under non-uniform signaling. The interest of these constellation formats is that they are naturally adapted to  $p$ -ary PAS coding. The type of CQAM-like constructions introduced in [16] is solely based on the minimum Euclidean distance. The chosen criteria maximize the figure of merit or the ratio between  $|\mathcal{X}|d_{\min}^2(\mathcal{X})$  and  $\sum_{x \in \mathcal{X}} |x|^2$ , where  $\mathcal{X}$  denotes the constellation, and  $d_{\min}^2$  is the minimum squared Euclidean distance. The minimum distance of the power-normalized constellation  $\mathcal{X}$  is first maximized via a greedy procedure. Then, MB shaping is performed such that, for a given SNR, the gap between the CM capacity and the Shannon limit is minimized. The work in [98] shows that the combined geometric-probabilistic CQAM leads to an exciting performance concerning the CM capacity. This is illustrated by Fig. 4.6, which shows that the shaped  $(8, 8)$  CQAM outperforms the 64-QAM regarding CM and SICM capacities.

### 4.3.2 New $(c, p)$ -Circular QAM Signals

Based on our previous observations on improving capacity by enabling different sampling/tilling strategies for a given modulation order, this section gives insight into the generalization of CQAM signals using the different tools presented in [16]. Assume that the constellation cardinality equals  $M$ , and let  $c$  ( $\leq M/2$ ) an integer that divides  $M$ . Inspired by previous observations, our approach looks at  $c$  shells with  $p = M/c$  points per shell instead of populating  $p$  shells with  $p$  points [98]. In this context, and following the construction given by [16], we build a  $(c, p)$  CQAM constellation depending on the design criteria, e.g., the figure of merit (minimum distance), and we formulate the  $c$  shells as follows:

1. For the first shell ( $i = 0$ ), draw  $p$  points  $(x_0 \dots x_{p-1})$ , which are uniformly spaced on the unit circle. The coordinate of points are given by

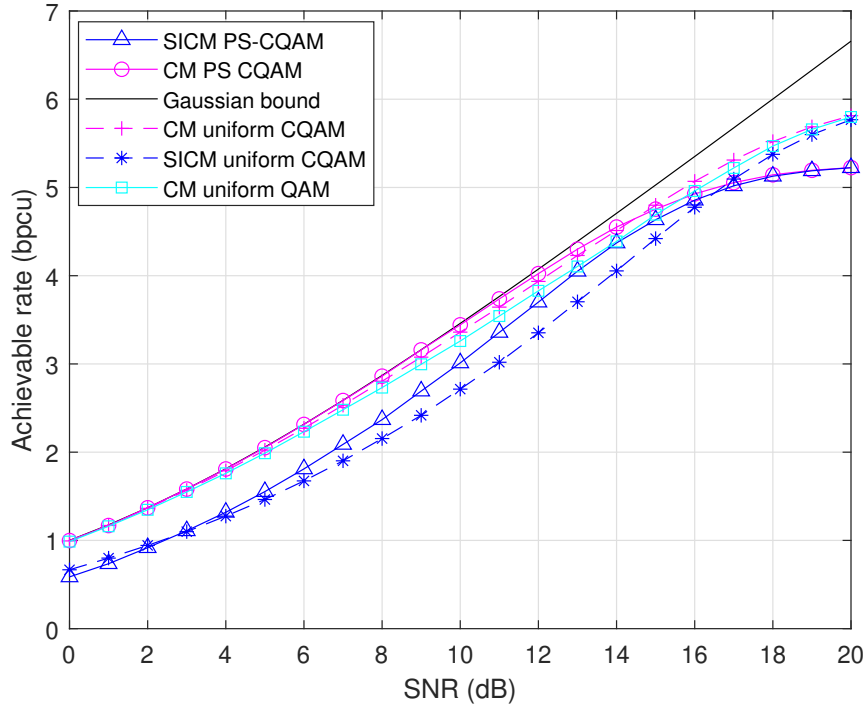


FIGURE 4.6: Information rate as a function of SNR over the linear AWGN channel for a constellation size  $M = 64$ .

$$\exp\left(i\ell\frac{2\pi}{p}\right), \text{ for } \ell = 0 \dots p-1;$$

2. Assume that shells from 0 to  $i-1$  are already constructed. For the  $i$ th shell, let  $x_{ip} = \rho_i \exp(i\Phi_i)$  be the first point. The remaining points are expressed as  $x_{ip+\ell} = \rho_i \exp\left(i\left(\Phi_i + \ell\frac{2\pi}{p}\right)\right)$ , for  $\ell = 1 \dots p-1$ . Let  $d_i^2$  be the minimum distance between the first point of the  $i$ th shell and all previously constructed shells. The radius  $\rho_i$  and the phase shift are determined along these lines:
  - Start with  $\rho_i = \rho_{i-1}$  and increment by a step  $\Delta_\rho$ ;
  - At each radius update, vary  $\Phi_i$  from  $\pi/p$  to  $-\pi/p$  by a step  $\Delta_\Phi$ ;
  - Stop updating the radius  $\rho_i$  and the phase shift  $\Phi_i$  when  $d_i^2 \geq 4 \sin^2\left(\frac{\pi}{p}\right)$ .

3. Repeat step 2 until reaching the  $c$ -th shell.

For a constellation size equal to  $M = 64$ , examples of  $(c, p)$  CQAM modulations are shown for  $c = 4$ ,  $c = 8$ , and  $c = 16$  in Fig. 4.7a, Fig. 4.7b, and Fig. 4.8c, respectively. For  $M = 256$ , Fig. 4.8 also shows the different studied CQAM constellation diagrams, with  $c = 8$ , 16, and 32.

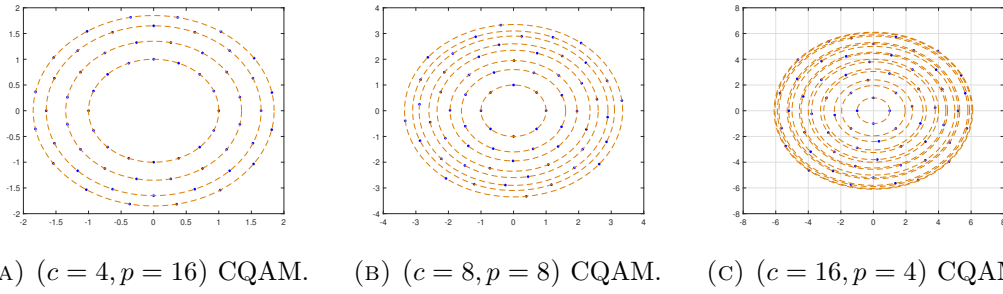


FIGURE 4.7: The different studied 64-CQAM constellation diagrams.

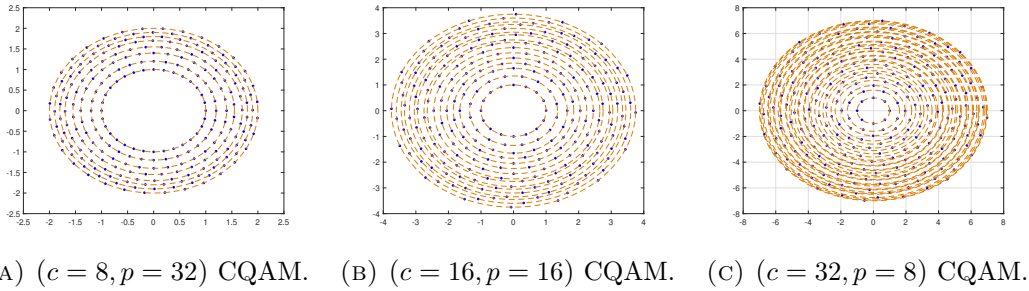


FIGURE 4.8: The different studied 256-CQAM constellation diagrams.

To increase the achievable MI, the radii of the CQAM constellation may be adapted. To that end, we can adopt two main strategies. First, one may adopt one of the two described GS approaches in sections 4.2.1 and 4.2.2 to get the different radii values and match them to the CQAM constellation. In other words, if the  $(c, p)$  CQAM construction produces the shells' radii  $\rho_0 \dots \rho_{c-1}$ , and if one of the GS approaches has the radii  $\rho'_0 \dots \rho'_{c-1}$  in the ascending order, then

$$\rho_i \longleftarrow \rho'_i \text{ for } i = 0 \dots c - 1. \quad (4.7)$$

As we can see, this update of CQAM radii is deterministic as it is computed directly by one of the two GS methods, GS-QAM or GS-APSK. In this context, we can show that using the GS-APSK design as a deterministic approach to revising the  $(c, p)$  CQAM radii leads to better performance than adopting radii from GS-PAM. Second, to devise optimized constellations close to the Shannon bound, we can perform a stretching step [98] to the CQAM radii instead of the deterministic GS approach. In this perspective, the optimization procedure is summarized as follows: the radius  $\rho_i$  of shell  $i$ , for  $i = 0 \dots c - 1$ , is taken to be

$$\rho_i = 1 + (\rho_{\max} - 1)(i/(c - 1))^\beta, \quad (4.8)$$

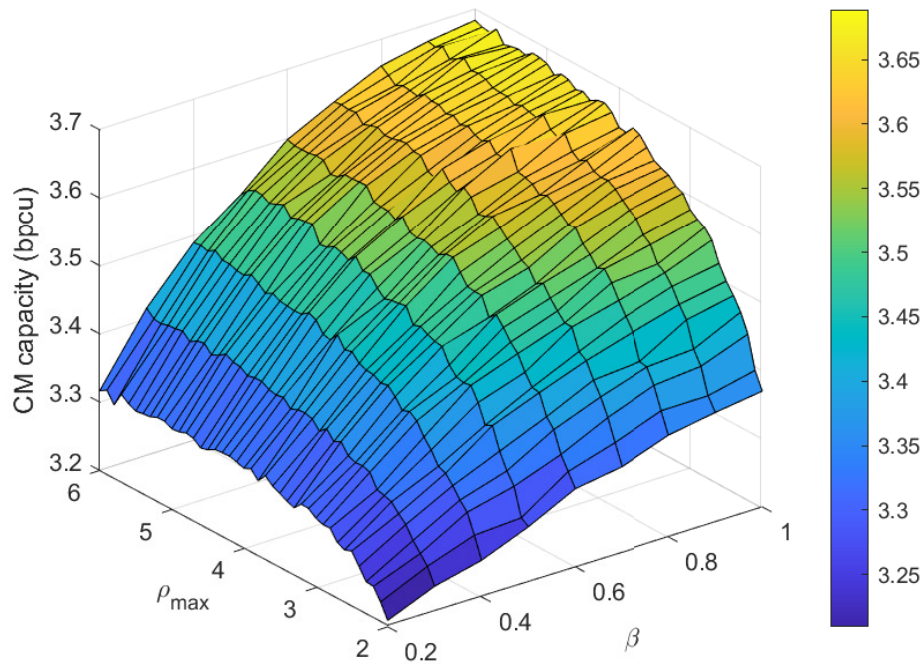


FIGURE 4.9: CM capacity for the stretched  $(8 \times 8)$  CQAM at 11 dB SNR as a function of the stretching parameters.

where the outer radius  $\rho_{\max}$  and the profile exponent  $\beta$  are the parameters to optimize. Fig. 4.9 illustrates the optimization procedure within a 3D plot that shows the CM capacity as a function of the stretching parameters. We consider the deterministic approach in the sequel to show the corresponding results.

### 4.3.3 Capacity Analysis

We numerically compare the CM capacity performance of the different CQAM formats to the traditional  $(c = 8, p = 8)$  CQAM format with an optional stretching as suggested in [98]. Fig. 4.10 shows the resulting CM performances vs. SNR for a constellation size  $M = 64$ . We can see that the proposed  $(c = 4, p = 16)$  and  $(c = 16, p = 4)$  CQAM signals approach the Gaussian bound and consistently outperform uniformly stretched  $(8, 8)$  CQAM signals for moderate SNRs (corresponding to coding rates around and slightly above 0.5). Around 4 bits/s/hz, we can see that the proposed  $(c = 4, p = 16)$  CQAM achieves similar performance to the  $(c = 4, p = 16)$  GS-APSK. They reach a 0.2 dB gain compared to the traditional  $(c = 8, p = 8)$  CQAM and the proposed  $(c = 16, p = 4)$  CQAM, which perform almost similarly. Fig. 4.11 shows results for  $M = 256$ . We can see that the proposed  $(c = 8, p = 32)$  CQAM has the best performance and achieves almost 0.05 dB and 0.35 dB gains compared to

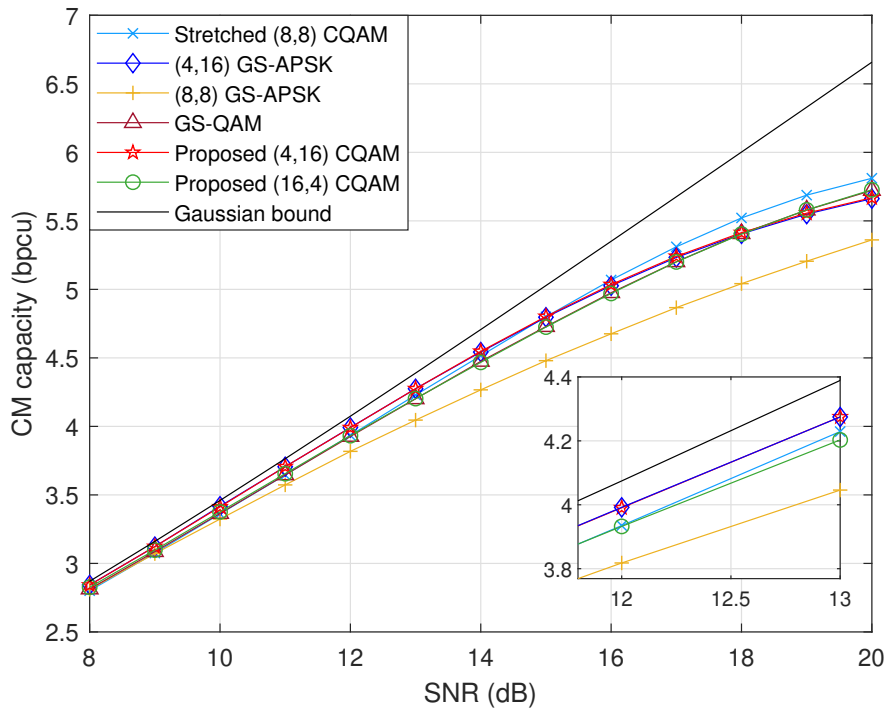


FIGURE 4.10: CM capacity performances estimated from a white Gaussian noise channel, as a function of the SNR for uniform 64-sized constellations.

the  $(c = 8, p = 32)$  GS-APSK, and the GS-QAM, respectively. In practical systems, we may refer to the BICM or SICM information rates. To perform well in practice, we should combine the geometry of the designed  $(c, p)$  CQAM constellations with Gray mapping. Fig. 4.12 compares the SICM capacity performance of the different constellations for  $M = 64$ . It is well observed that our proposed design consistently outperforms the traditional  $(c = 8, p = 8)$  CQAM with equiprobable signaling ( $H(X) = 6$ ) for the entire SNR region. For example, around 4 bits/s/hz, the  $(c = 4, p = 16)$  CQAM and the  $(c = 16, p = 4)$  CQAM achieve almost 0.8 dB and 0.5 dB gains, respectively. Despite their use of PS, we can see that the proposed  $(c = 4, p = 16)$  CQAM with equal probability is close to the traditional  $(c = 8, p = 8)$  CQAM performance. This seems interesting since we have excellent performance without PS, which requires a complex DM to reshape the source distribution. Fig. 4.13 shows results for  $M = 256$ . We can see that the proposed  $(c = 8, p = 32)$  CQAM has the best performance and achieves almost 0.8 dB gain compared to the  $(c = 8, p = 32)$  GS-APSK.

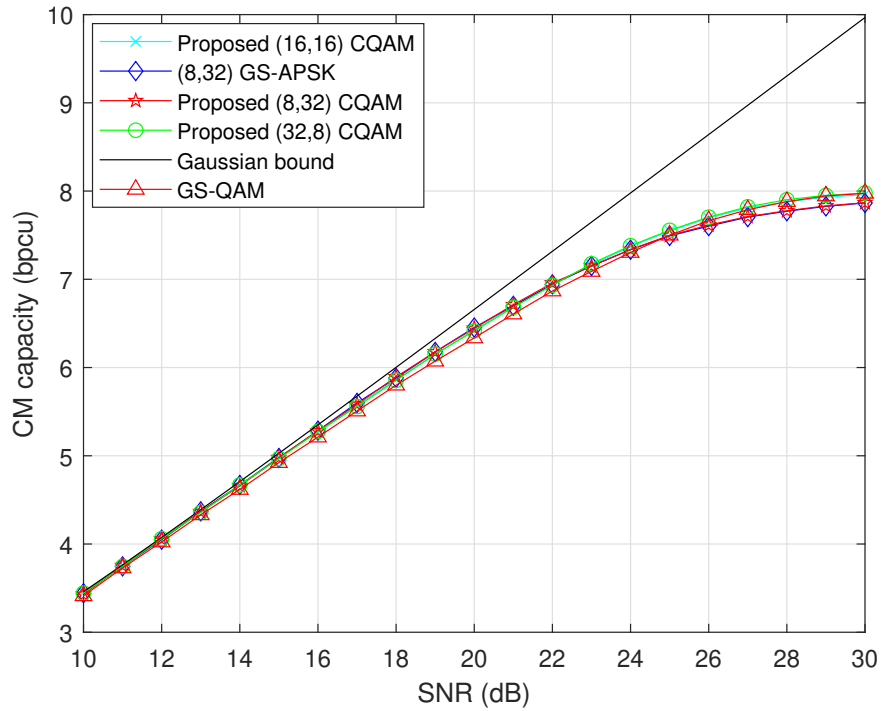


FIGURE 4.11: CM capacity performances estimated from a white Gaussian noise channel, as a function of the SNR for uniform 256-sized constellations.

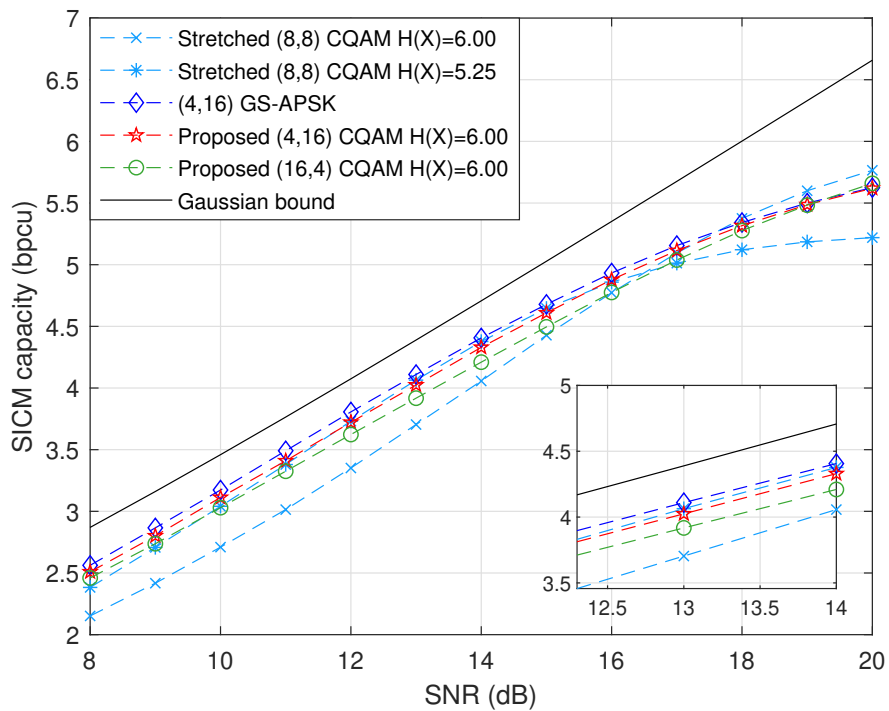


FIGURE 4.12: SICM capacity performances estimated from a white Gaussian noise channel as a function of the SNR for 64-sized constellations.

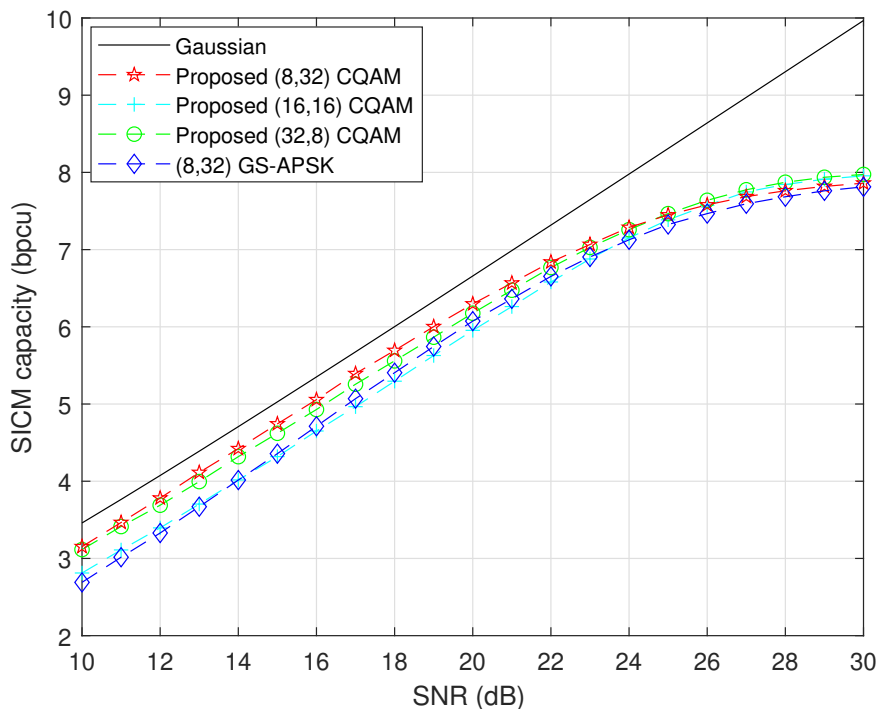


FIGURE 4.13: SICM capacity performances estimated from a white Gaussian noise channel as a function of the SNR for 256-sized constellations.

## 4.4 Design of Non-binary Protograph Codes for Geometric Shaping

In this section, we intend firstly to investigate efficient non-binary protograph codes for GS. These coding schemes are defined on  $\mathbb{F}_q$  for GS-shaped constellations  $\mathcal{X}$  of even order  $M$ , with  $q \leq M$ , assuming a uniform distribution of the symbols in  $\mathcal{X}$ . The coded symbols are transmitted over an additive memoryless Gaussian channel. We design non-binary protograph codes defined on  $\mathbb{F}_q$ . For the optimization, we have considered non-binary protograph LDPC codes [55, 58]. The goal is to optimize the asymptotic convergence threshold to operate close to the capacity. The optimization consists of selecting the coefficients of the associated adjacency matrix referred to as *base matrix*, noted  $\mathbf{H}_B$ , whose elements lie in  $\mathbb{N}^+$ . This is usually done using PEXIT [58].

For GS-QAM signals, we have considered the approach from [55, 58], directly inspired by [50], considering the obtained modulation as the Cartesian product of two GS-PAMs. For GS-APSK modulations or CQAM signals with  $q = M$ , we can easily generalize the estimation of EXIT functions of [50] by rewriting [50, Lemma 12] directly for a complex codebook. Thus, for regular non-binary

TABLE 4.1: SNR thresholds in dB for different non-binary constellations over  $q = M = 64$  and regular  $(2, d_c)$  non-binary protograph codes.

Rate	Shannon	(4, 16) CQAM	(4, 16) GS-APSK	64 GS-QAM
1/3	4.77	5.15	5.15	5.22
1/2	8.45	8.81	8.78	8.88
2/3	11.75	12.25	12.25	12.34
3/4	13.35	14.03	14.04	14.18
4/5	14.29	15.16	15.20	15.37

protographs, we get the results given in Table 4.1. This shows that (4, 16) CQAM and GS-APSK perform nearly the same with codes that operate close to their modulation capacity. Non-binary codes with GS-QAM perform slightly worse. At 4 bits/s/Hz, we found that

$$\mathbf{H}_B = \begin{pmatrix} 1 & 2 & 0 & 0 & 0 & 0 & 0 \\ 0 & 1 & 1 & 1 & 1 & 1 & 1 \\ 0 & 1 & 1 & 1 & 1 & 1 & 1 \end{pmatrix} \quad (4.9)$$

has a threshold of 12.13 dB and 12.15 dB for the 64-GS-APSK and the (4,16)-CQAM, respectively (the second column corresponds to a punctured node). This is close to their respective modulation capacity. For GS-APSK or CQAM signals with  $q = \sqrt{M}$ , we extend the preceding methods by considering the Monte Carlo evaluation. Initial non-binary log-likelihood messages are generated from MAP symbol estimation (symbol-wise marginalization). In this context, we have compared the 64 GS-APSK with the 64-GS-QAM, for which we can have good SICM capacities. In Table 4.2, we have compared several simple protographs for a targeted rate of 4 bits/s/hz for codes defined on  $q = 8$ . This shows that we can operate very close to the SICM capacity, which is very close to the modulation capacity. Thus, efficient *low-complexity* non-binary coding schemes can be designed to operate close to the capacity.

## 4.5 Conclusion

This work has investigated  $(c, p)$  CQAM constellations with equiprobable signaling that can approach the Gaussian capacity. Compared to existing approaches where  $c = p$ , we can find parameters that allow us to get closer to the uniform input capacity. Furthermore, we have designed simple non-binary

TABLE 4.2: SNR thresholds in dB for 64-GS APSK and QAM constellations over  $q = \sqrt{M} = 8$  for different protographs. The left column in blue corresponds to punctured variable nodes.

$\mathbf{H}_B$	GS-APSK	GS-QAM
$\binom{222}$	13.48	13.35
$\binom{322}$	12.61	12.62
$\begin{pmatrix} 1 & 1 & 1 & 1 & 1 & 1 & 0 \\ 1 & 1 & 1 & 1 & 1 & 1 & 0 \\ 2 & 1 & 0 & 0 & 0 & 0 & 1 \end{pmatrix}$	12.17	12.23

protographs for GS constellations, showing that we can operate close to the capacity.



## Chapter 5

# PAS with Non-binary LDPC Codes for CQAM Signals

### 5.1 Introduction

The constellation points with PS are sent with different probabilities than standard modulation formats with equal probability. In this context, PS techniques can be classified into two subgroups. On the first hand, the first group refers to the direct approach that fixes a target distribution and finds an algorithm to reach it [41]. In recent literature [100], the direct approach can also be called DM. On the other hand, the other group refers to the indirect approach that fixes a target rate and bounds the  $n$ -dimensional signal by a sphere, which we call sphere shaping [94]. Recently, the invention of PAS was essential for making PS efficient [14]. PAS concatenates a shaping outer code called a DM and an FEC inner code. The DM is the enabling device that transforms uniform input bits into arbitrarily shaped sequences. Many different DM schemes have been proposed in the literature [15, 101–103]. Also, many FEC codes, such as LDPC, turbo, or polar codes, can be employed. It was demonstrated that PAS increases transmission reach by up to 40%.

This chapter shows how to combine non-binary LDPC codes over  $\mathbb{F}_q$  with PS to transmit CQAM signals over the AWGN channel. To this end, we extend our previous chapter to CQAM modulations using PS. We first analyze the achievable capacities for such schemes. Then, for short blocklengths, the objective of shaping should be reformulated as achieving the most energy-efficient signal space for a given rate rather than matching distributions. In this perspective, sphere shaping is reviewed as an energy-efficient shaping technique. Deploying the CQAM constellations design as proposed in [104], we present end-to-end decoding performance simulation results. Compared to uniform signaling, up

to 1.25 dB improvement in power efficiency is shown with sphere shaping at blocklengths around 100.

The remainder of this chapter is organized as follows. Section 5.2 gives some preliminaries about PS techniques. Section 5.3 shows how to combine non-binary LDPC codes with PAS, particularly with sphere shaping. Section 5.4 provides numerical simulation results for short blocklength and compares the uniform and shaping signaling. Finally, we conclude in section 5.5.

## 5.2 Preliminaries

### 5.2.1 Distribution Matching

A DM transforms input bits uniformly distributed into a sequence of output symbols with the desired distribution. Fixed-to-fixed length, a DM maps  $k$  input bits to  $n$  output symbols representing the shells of the CQAM constellation. The mapping is invertible so that a low-complexity decoder can recover the input from the output. The DM rate is equal to

$$R_s = \frac{k}{n} \left[ \frac{\text{bits}}{\text{output symbols}} \right]. \quad (5.1)$$

The constant composition DM (CCDM) has been proposed in [15], and it was used as the amplitude shaping architecture for PAS in [14]. With CCDM, all matcher output sequences are permutations of a particular base sequence, typically described by the composition  $C$  that states the number of occurrences of each amplitude. All amplitude sequences have the same energy  $E^O$  and are located on the  $n$ -shell of squared radius  $E^O$ .

### 5.2.2 Sphere Shaping

The sphere shaping algorithms target a certain rate, i.e., the number of unique output sequences, rather than a probability mass function (PMF). For a given set of amplitude alphabets  $\mathcal{S} = \{1, 3, \dots, 2^m - 1\}$ ,  $n$ , and  $k$ , the maximum-energy constraint  $E_{\max}$  is selected as the minimum value such that  $|\mathcal{S}_o| \geq 2^k$  where  $\mathcal{S}_o$  is defined as follows:

$$\mathcal{S}_o = \left\{ s_1, s_2, \dots, s_n \mid \sum_{i=1}^n s_i^2 \leq E_{\max} \right\}, \quad (5.2)$$

i.e., it consists of all  $2^m$ -ASK amplitude lattice points on the surface of or inside the  $n$ -dimensional sphere of square radius  $E_{\max}$ . An algorithm for realizing sphere shaping is enumerative sphere shaping (ESS). The latter starts from the assumption that the energy-bounded amplitude sequences can be ordered lexicographically. Therefore, the index of an amplitude sequence is defined as the number of lexicographically smaller sequences. To represent  $n$ -amplitude sequences inside a sphere, an energy-bounded enumerative amplitude trellis is constructed as described in [105]. This can be implemented by considering the path representing  $s^n$  in the trellis and adding the number of paths that branch off to lower nodes.

### 5.2.3 Comparison: Finite Length Rate Loss

The rate loss of a shaping set  $\mathcal{S}^*$  with average distribution  $P_{\mathcal{S}}(s)$  can be defined as

$$R_{\text{loss}} = \mathbb{H}(P_{\mathcal{S}}) - k/n. \quad (5.3)$$

For asymptotically long blocklengths, the CCDM is known to generate the target-achieving distribution. However, for small blocklengths, the resulting rate loss diminishes the efficiency of CCDM. In this context, i.e., for short blocklengths, the sphere shaping is shown to have the minimum rate loss amongst all. Fig. 5.1 shows the rate loss versus the blocklength for CCDM and ESS. We fix the target shaping rate  $R_s = 1.75$ , and for each  $n$ , we choose a target amplitude composition  $\#(s) \approx nP_{\mathcal{S}}(s)$ ,  $s \in \mathcal{S}$ , and  $E_{\max}$  for CCDM and ESS, respectively, such that these PS codes have at least  $2^k$  signal points, with  $k = \lfloor nR_s \rfloor$ . We use the amplitude alphabet  $\mathcal{S} = \{1, 3, 5, 7\}$  of 8-ASK. At  $n = 96$ , we observe that the sphere shaping code has an almost five times lower rate than the CCDM code. We note that  $n = 96$  is the number of real dimensions in a single orthogonal frequency-division multiplexing (OFDM) symbol for one of the modes in the IEEE 802.11 standard. As shown in Fig. 5.1, it is well-observed that the spheres codes outperform the constant composition codes at small blocklengths for a fixed rate  $R_s$ . Therefore, we employ only the sphere codes in our work as long as we deal with the finite length regime.

## 5.3 PAS with Non-binary Codes for CQAM

This section describes our proposed approach that combines the non-binary LDPC codes over  $\mathbb{F}_q$  with PAS. The combination of PAS and non-binary codes is depicted in Fig. 5.2. All details about the two mapping functions  $\beta(\cdot)$  and

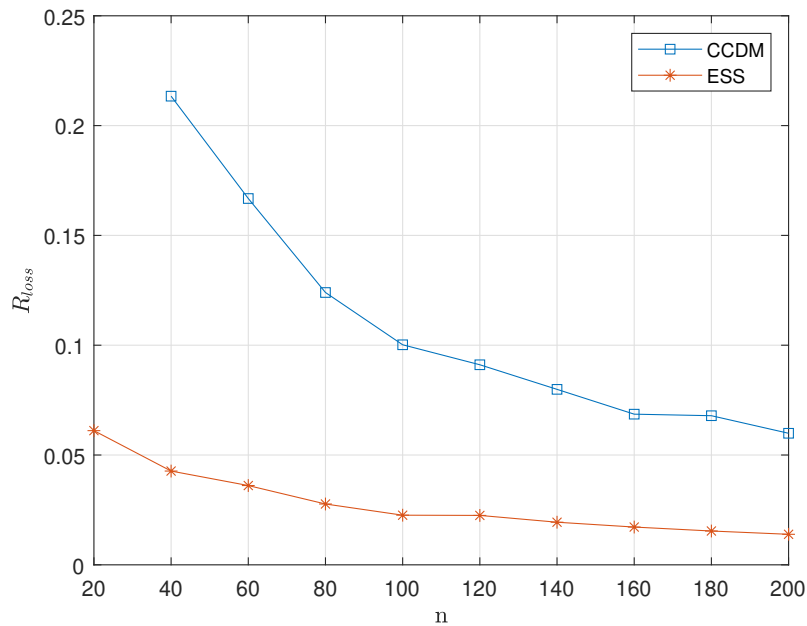


FIGURE 5.1: Comparison of constant composition and sphere codes regarding rate loss. The target shaping rate is  $R_s = 1.75$  bit/amp. with 8-ASK.

$\tau(\cdot)$  will be described in sections 5.3.2 and 5.3.4, respectively. Here, we present the non-binary PAS framework of the studied  $(c, p)$  CQAM constellations. For instance, regarding the  $(c = 4, p = 16)$  CQAM, we consider at first a DM that will generate a non-uniform sequence of 8-ary symbols. These symbols are associated with a base "PAM"-like a constellation, and from which we can generate the whole CQAM constellation by applying 8 rotations. This sequence is the input to the non-binary LDPC encoder over  $\mathbb{F}_8$ . The parity symbols, which are uniformly distributed, determine the rotation angles relative to the abscissa axis. The resulting shaping involves  $c = 4$  circles, each containing  $p = 16$  points. Regarding the  $(c = 16, p = 4)$  CQAM constellation, we consider a non-uniform 16-ary information source that generates symbols in the set  $\{0, 1, \dots, 15\}$  associated with a shell, as classically done by [16]. Then, each source symbol can be mapped to a vector of two symbols over  $\mathbb{F}_4$ . We can encode the resulting non-binary symbols with a non-binary LDPC code over  $\mathbb{F}_4$ . The resulting parity symbols then help select a point within a shell associated with a source symbol. In this way, the code rate constraint of the LDPC encoder is necessary such that  $R_c \geq 2/3$ . Eventually, we should mention that, for each  $(c, p)$  CQAM-based transmission system, we should devise non-uniform signaling (PS) strategies specifically.

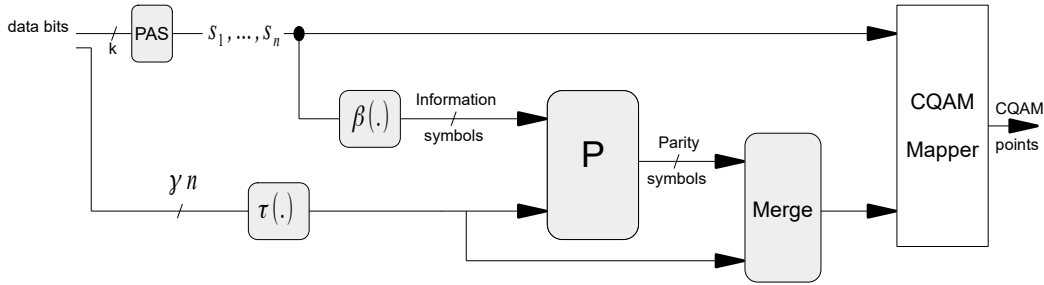
FIGURE 5.2: System model of PAS with non-binary  $\mathbb{F}_q$  codes.

TABLE 5.1: Gain in dB of PS for circular constellations: (8,8)-CQAM, (4,16)-CQAM and (16,4)-CQAM.

Constellations	Target Rate	Gap to Capacity	Potential Gain
(8, 8)-CQAM	4	0.086 (1.259)	0.38 (0.818)
(4, 16)-CQAM	4	0.256 (1.159)	0 (0)
(16, 4)-CQAM	4	0.111 (0.959)	0.396 (0.564)

### 5.3.1 PS Performance

We provide some results for the PS of the proposed CQAMs. Table 5.1 includes results for 64-CQAM shaping concerning the CM and SICM capacity, whose data occurs within parentheses. We see that PS does not always bring performance improvements. If we only consider achievable rates for the SICM capacity for that scheme, PS CQAMs do not seem to bring a serious advantage compared to well-designed GS constellations. However, if iterative decoding is performed, we could get closer to the achievable CM capacity at the price of increased complexity. Table 5.2 shows results for 256-CQAM shaping. We can see that PS improves only the performance of (16,16) CQAM constellations, whereas poor gain is achieved for the other constellations.

### 5.3.2 CQAM with Non-binary Codes

Consider a non-binary LDPC code  $\mathcal{C}$  which is defined as the nullspace of the sparse parity-check matrix  $\mathbf{H}$  of dimension  $m_c \times n_c$  where the non-zero entries  $h_{ij}$  of  $\mathbf{H}$  are taken from the finite field  $\mathbb{F}_q$ . Let  $R_c = k_c/n_c$  be the coding rate of  $\mathcal{C}$ , where  $n_c$  is the code length and  $k_c = n_c - m_c$  is the code dimension. For

TABLE 5.2: Gain in dB of PS for circular constellations: (16,16)-CQAM, (8,32)-CQAM and (32,8)-CQAM.

Constellations	Target Rate	Gap to Capacity	Potential Gain
(16, 16)-CQAM	6	0.15 (0.5)	0.325 (0.75)
(8, 32)-CQAM	6	0.4 (1)	0 (0)
(32, 8)-CQAM	6	0.5 (1.4)	0.06 (0.08)

shaping, we can consider two different techniques. The first technique we can employ is the CCDM which transforms input bits uniformly distributed into a sequence of output symbols with the desired distribution  $R_s$ . Fixed-to-fixed length, a DM maps  $k$  input bits to  $n$  output symbols representing the shells of the CQAM constellation. The mapping is invertible so that a low-complexity decoder can recover the input from the output. On the other hand, we can employ the ESS algorithm. It maps  $k = \lfloor nR_s \rfloor$  input bits to  $n$  output symbols representing the shells of the CQAM constellation.

Let  $s_1, s_2, \dots, s_n$  be the amplitude sequence generated by shaping with a priori probability distribution  $\{\pi_i\}_{i=1}^c$  where  $c$  also represents the size of the amplitude alphabet  $\mathcal{S}$ . Given the a priori distribution of amplitude symbols in the finite field  $\mathbb{F}_c$ , the non-binary LDPC code and the  $(c \times p)$ -CQAM should be combined as illustrated in Fig. 5.2. Each amplitude symbol requires  $\log_2(c)$  bits for representation. When  $(c \times p)$ -CQAM is combined with non-binary codes over  $\mathbb{F}_q$ , the amplitude symbols in  $\mathbb{F}_c$  should be mapped to symbols in  $\mathbb{F}_q$ . We denote this mapping as

$$\beta : \mathbb{F}_c^n \rightarrow \mathbb{F}_q^\ell, \quad (5.4)$$

where the variable  $\ell$  is defined as

$$\ell = n \log_2 c / \log_2 q.$$

### 5.3.3 Coding Rates Equal To $\log_2 c / (\log_2 c + \log_2 p)$

In the first setting, we suppose that the coding rates of the non-binary codes are equal to  $R_c = \log_2 c / (\log_2 c + \log_2 p)$ . The parameter  $\gamma$  in Fig. 5.2 defines the fraction of extended bits to add to the proposed scheme. In this case,  $\gamma$  always equals zero, so we will pay attention to it in the following setting. Therefore, the

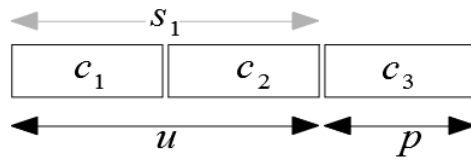


FIGURE 5.3: Illustration how the codeword symbols of a  $\mathbb{F}_4$  code are associated with amplitudes and parity symbols for  $(16 \times 4)$  CQAM with PAS.

information symbols comprise  $\ell$  non-uniformly distributed symbols belonging to  $\mathbb{F}_q$ . They are collected in a vector  $\mathbf{u} \in \mathbb{F}_q^\ell$  to represent the model input to the non-binary LDPC code  $\mathcal{C}$ . So, we can deduce in this setting that  $\ell = k_c$ . Systematic encoding yields the parity part of  $(1 - R_c)n_c$  symbols that are approximately uniformly distributed [16]. For instance, we illustrate the setting for  $R_c = 2/3$  codes and a  $(16 \times 4)$ -CQAM constellation in Fig 5.3. We consider a code over  $\mathbb{F}_4$  ( $q = 4$ ) and a blocklength of three symbols. Then, the  $\ell=2$  symbols in the information part represent one shell of the 16 shells. The last codeword symbol forms the parity part, representing one point of the 4 points in the corresponding shell. This way, the constellation points are constructed and transmitted through the channel. We should note that the PAS transmitter's overall transmission rate  $R_t$  equals the shaping rate  $R_s$ .

### 5.3.4 Coding Rates Bigger Than $\log_2 c / (\log_2 c + \log_2 p)$

In the second scheme, we consider coding rates strictly larger than  $\log_2 c / (\log_2 c + \log_2 p)$ . In this case, a binary source generates  $\gamma n$  uniformly distributed bits that are mapped by  $\tau : \{0, 1\}^{\gamma n} \rightarrow \mathbb{F}_q^{\ell'}$  to be part of parity symbols of size equal to  $\ell' = \gamma n / \log_2 q$ . Therefore, we have  $k_c = \ell + \ell'$ . The code rate in this scheme is  $R_c = (\log_2 c + \gamma) / (\log_2 c + \log_2 p)$ ; thus  $\gamma = (\log_2 c + \log_2 p)R_c - \log_2 c$  specifies the number of extra data bits that will be transmitted per symbol. Its derivation is shown in Appendix A. For instance,  $\gamma$  has the following expressions

$$\gamma_{(8 \times 8)} = 6R_c - 3, \text{ and } \gamma_{(16 \times 4)} = 6R_c - 4, \quad (5.5)$$

for the  $(8 \times 8)$  CQAM and  $(16 \times 4)$  CQAM, respectively. In this modified structure, in addition to the  $(n \log_2 c)$  bit output of the sphere shaper, extra  $\gamma n$  information bits are fed to the LDPC code over  $\mathbb{F}_q$ . The latter is now specified

by the  $m_c \times n_c$  parity-check matrix  $P$  where

$$\begin{aligned} k_c &= (\log_2 c + \gamma)n / \log_2 q, \text{ and} \\ n_c &= k_c / R_c = (\log_2 c + \log_2 p)n / \log_2 q. \end{aligned} \quad (5.6)$$

The  $(n_c - k_c) \log_2 q$  bit parity output of the LDPC code is then multiplexed with the  $\gamma n$  uniform bits to form an  $n$ -symbol sequence in  $\mathbb{F}_p$  that will select the points in the shells. The transmission rate of the PAS transmitter is

$$R_t = R_s + \gamma. \quad (5.7)$$

The considerable flexibility in supported spectral efficiencies is achieved using different shaping rates  $R_s$  for the same LDPC code.

### 5.3.5 PAS Receiver

An iterative demapping and decoding architecture are used in our proposed scheme. A soft demapper computes the LLRs at the receiver. Then, the LLRs are processed by the turbo decoder at the same iteration to exploit all received information iteratively. A maximum of 100 iterations are performed during the belief propagation decoding. Since the decoding precedes the deshaping algorithm in PAS, we do not require a soft-output deshaper which can involve considerable complexity.

## 5.4 Finite Length Simulations

This section provides simulation results of the end-to-end decoding performance for non-binary LDPC codes with short blocklengths. PAS decoding performance is evaluated after transmitting a 64-CQAM signal over the AWGN channel. Two modulations are employed: the (8, 8) CQAM and the (16, 4) CQAM that show performance improvements when applied with PAS architecture. We consider a target transmission rate  $R_t = 4$  and a blocklength  $n = 96$  of non-binary LDPC codes over  $\mathbb{F}_{q=64}$ . For each SNR value, we run simulations until at least 100 frame errors are reached. We aim to compare the uniform and shaped signaling techniques at the same transmission rate  $R_t$ , as it is the only fair comparison.

We ignore the ESS operation that produces non-uniformly distributed symbols in uniform signaling. Instead, a  $k$  bit sequence uniformly distributed  $u^k$  is mapped to  $k_c$  symbol sequence over  $\mathbb{F}_q$  and encoded by an LDPC code of rate  $R_c = k_c/n_c$ . Then, the coded sequence  $c^{n_c}$  is mapped into a sequence  $x^n$

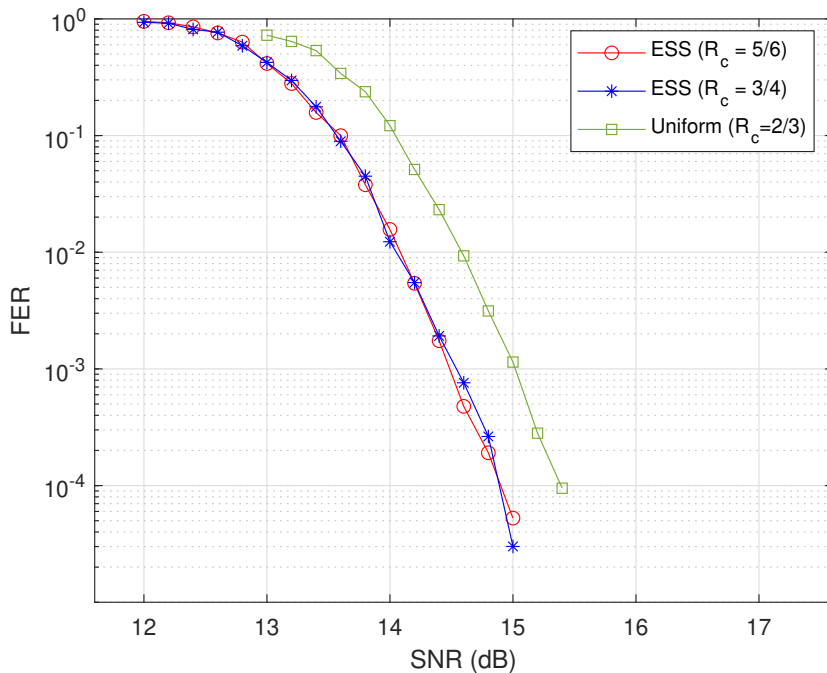


FIGURE 5.4: FER vs SNR for (8,8) CQAM at transmission rate  $R_t=4$  and shaping blocklength  $n = 96$ .

consisting of channel input symbols to be transmitted over the channel. The transmission rate of this scheme is  $R_t = k/n$ . At this stage, we can compare the uniform and shaped signaling at the same target transmission rate  $R_t$ . Fig. 5.4 shows the decoding performance with the non-binary LDPC codes over  $\mathbb{F}_{q=64}$  for ESS and uniform signaling at a transmission rate of  $R_t = 4$  bits per channel use for the (8, 8) CQAM constellation. For uniform signaling, the coding rate equals  $R_c = 2/3$  to guarantee  $R_t = 4$ . For the uniform shaping, we have tested two different coding rates,  $R_c = 3/4$  and  $R_c = 5/6$ . We have employed two shaping rates,  $R_s = 2.5$  and  $R_s = 2$  for  $R_c = 3/4$  and  $R_c = 5/6$ , respectively. As shown in Fig. 5.4, both perform similarly and outperform uniform signaling. For example, to achieve a FER of  $10^{-3}$ , shaping signaling requires 0.5 dB less than uniform signaling.

In Fig. 5.5, we plot the FER vs. SNR for (16,4) CQAM at  $R_t = 4$ . This time, we observe the difference between the two coding rates  $R_c = 3/4$  and  $R_c = 5/6$  in shaping signaling. The shaping rate  $R_s = 3$  corresponding to  $R_c = 5/6$  performs better than  $R_c = 3/4$ . Further, it outperforms the uniform signaling and achieves a 1.25 dB SNR gain at a FER of  $10^{-3}$ . Someone wonders how to choose the optimum coding rate  $R_c$  for  $(c, p)$  CQAM constellations.

If we assume that the input is constrained to follow a Maxwell-Boltzmann (MB)

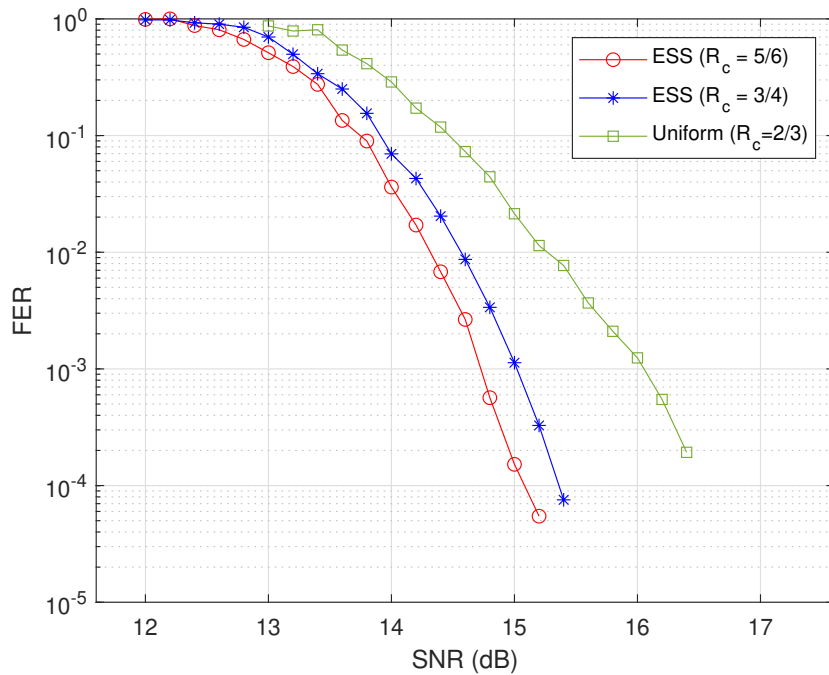


FIGURE 5.5: FER vs. SNR for (16,4) CQAM at transmission rate  $R_t=4$  and shaping blocklength  $n = 96$ .

distribution  $P_S(s) \sim e^{-\lambda s^2}$ , then  $\mathbb{H}(X) = \mathbb{H}(S) + \log_2 p$  can be used as a design parameter to tune the balance between shaping and coding redundancies at a fixed rate  $R_t$ . More precisely, the entropy  $\mathbb{H}(S)$  is controlled by the MB parameter  $\lambda$ , and the question is how to choose the optimum  $\lambda$ . Following [25], we define the gap to capacity as follows:

$$\Delta\text{SNR} = \frac{\text{SNR}_{\text{SMD}}}{2^{R_t} - 1}, \quad (5.8)$$

where  $\text{SNR}_{\text{SMD}}$  is the SNR value at which  $R_{\text{SMD}} = R_t$  for a given  $P_X$ . The denominator in (5.8) is the SNR value at which the capacity  $C_{\text{AWGN}} = R_t$ . Generally, the gap-to-capacity can be computed for any parametric family of distributions. Here we only consider the MB distributions. When transmitting the  $(c, p)$  CQAM, the rate of the LDPC code that should be employed in PAS to obtain a transmission rate  $R_t$  for a given constellation entropy  $\mathbb{H}(X)$  is given by

$$R_c = \frac{\log_2 c + \gamma}{\log_2 c + \log_2 p} = \frac{\log_2 c + R_t - (\mathbb{H}(X) - \log_2 p)}{\log_2 c + \log_2 p}. \quad (5.9)$$

The deduction to be made from the last equations (5.9) is that we choose the optimum point  $\mathbb{H}(X)$  that minimizes the gap to capacity  $\Delta\text{SNR}$  in (5.8) for a

---

fixed  $R_t$ , and then we conclude the optimum  $R_c$ .

## 5.5 Conclusion

In this work, we have investigated  $c \times p$  CQAM constellations with non-uniform signaling that reach the Gaussian capacity. We have shown in a novel strategy how to combine non-binary LDPC codes over  $\mathbf{F}_q$  with PAS. Numerical simulation results with high-order non-binary LDPC codes show the decoding performance for the different CQAM constructions for short blocklengths.



## Chapter 6

# Conclusions and Perspectives

This thesis is dedicated to designing and evaluating the CM schemes based on  $M$ -ary signalling and non-binary LDPC channel coding. Different schemes have been tested to achieve performance approaching the channel capacity over interesting channels.

We first studied the PDL-resilient signalling and an optimal four-dimensional modulation developed in the literature. We first tested the SB signalling with a single PDL element to evaluate the performance. The latter showed an increase in the worst encountered rate. Also, we have tested the NSB signalling that offered rate increases. We have noticed that the behaviours of CM and BICM capacities are different in the active SNR region. Indeed, the performance behaviour is conditioned by the initial geometric properties of the constellation.

Second, we have investigated the combination of precoding schemes, SB and NSB, and the shaping constellations. This combination has shown a better performance of up to 1.5 dB. Furthermore, we have concluded that precoding is not efficient for low-to-moderate SNR regions. In contrast, PS usually improves the performance of the whole SNR region. Finally, we have also studied the design of non-binary protograph LDPC codes for precoded optical MIMO transmissions. Results show that we can design satisfying codes that operate close to the zero-outage capacities.

Third, we have investigated  $(c, p)$  CQAM constellations with equiprobable signalling that can approach the Gaussian capacity. We also have discussed how PS with non-binary LDPC codes can enhance performance. Further, simple non-binary protographs for GS constellations have been designed to show that we can operate close to the capacity.

The last part of this thesis has shown how to combine non-binary LDPC codes over  $\mathbb{F}_q$  with PAS for the different CQAM constructions. Simulation results with

high-order non-binary LDPC codes show the decoding performance for short blocklengths and the advantage yielded by shaping compared to the uniform signalling.

In the following, we give insight into possible research directions:

- For the optical channel, we can consider the design of efficient non-binary spatially-coupled schemes enabling both good finite-length performance and convenient thresholds for the MIMO case.
- Advanced shaping schemes such as combined geometric and probabilistic CQAM could be designed and perform well. This may be key for the next generation of communication systems.
- Since significant performance gains come from efficient channel coding and particular constellation geometry, it is interesting to jointly design coding and modulation schemes to approach the channel capacity.

## Appendix A

# Extended PAS for $(c, p)$ CQAM

We consider the proposed PAS scheme for  $(c, p)$  CQAM signals as proposed in Chapter 5. We suppose that the coding rate  $R_c$  is strictly bigger than  $\frac{\log_2 c}{\log_2 c + \log_2 p}$ . In general,  $R_c$  equals  $k_c/n_c$  where  $k_c$  defines the length of information symbols, and  $n_c$  is the code length.

We suppose that the non-uniformly sequence of information symbols generated by the ESS algorithm is of length  $n$  in  $\mathbb{F}_c$ . As we deal with non-binary LDPC codes over  $\mathbb{F}_q$ , these non-uniformly symbols are mapped to symbols in  $\mathbb{F}_q$  of length  $\ell$ . In addition, extra  $\gamma n$  uniformly distributed bits are also mapped to symbols in  $\mathbb{F}_q$  of length  $\ell' = \frac{\gamma n}{\log_2 q}$ . Together, all these symbols in  $\mathbb{F}_q$  constitute the input of the LDPC encoder. Thus, we have

$$\begin{aligned} k_c &= \ell + \ell' \\ &= n \frac{\log_2 c}{\log_2 q} + \gamma n \frac{1}{\log_2 q} \\ &= \frac{n}{\log_2 q} (\log_2 c + \gamma) \end{aligned} \tag{A.1}$$

Suppose that the number of redundancy symbols in  $\mathbb{F}_q$  added by the LDPC encoder equals  $m_c = n_c - k_c$ . We have

$$m_c = (1 - R_c)n_c = \frac{1 - R_c}{R_c} k_c \tag{A.2}$$

Based on the proposed  $(c, p)$  CQAM mapper, we should have the following equality

$$\left( \ell' + m_c \right) \frac{\log_2 q}{\log_2 p} = n \tag{A.3}$$

Substituting (A.2) in (A.3), we obtain

$$\left(\ell' + \frac{1 - R_c}{R_c} k_c\right) \frac{\log_2 q}{\log_2 p} = n \quad (\text{A.4})$$

Replacing  $\ell'$  and  $k_c$  in (A.4), we get the following equality

$$\left(\gamma n + \frac{1 - R_c}{R_c} n(\log_2 c + \gamma)\right) \frac{1}{\log_2 p} = n \quad (\text{A.5})$$

Finally, (A.5) leads to

$$\gamma + \frac{1 - R_c}{R_c} (\log_2 c + \gamma) = \log_2 p \quad (\text{A.6})$$

Thus;  $\gamma = (\log_2 c + \log_2 p)R_c - \log_2 c$

# Bibliography

- [1] D. J. Costello and G. D. Forney, “Channel coding: The road to channel capacity,” *Proceedings of the IEEE*, vol. 95, no. 6, pp. 1150–1177, 2007.
- [2] C. E. Shannon, “A mathematical theory of communication,” *ACM SIG-MOBILE mobile computing and communications review*, vol. 5, no. 1, pp. 3–55, 2001.
- [3] R. W. Hamming, “Error detecting and error correcting codes,” *The Bell system technical journal*, vol. 29, no. 2, pp. 147–160, 1950.
- [4] R. G. Gallager, “Low-density parity check codes. cambridge,” *Massachusetts*, 1963.
- [5] C. Berrou, A. Glavieux, and P. Thitimajshima, “Near shannon limit error-correcting coding and decoding: Turbo-codes. 1,” in *Proceedings of IEEE Int. Conf. Commun.*, vol. 2, 1993, pp. 1064–1070.
- [6] D. J. MacKay and R. M. Neal, “Good codes based on very sparse matrices,” in *IMA Int. Conf. Crypto. Coding*. Springer, 1995, pp. 100–111.
- [7] D. J. MacKay, “Good error-correcting codes based on very sparse matrices,” *IEEE Trans. Inf. Theory*, vol. 45, no. 2, pp. 399–431, 1999.
- [8] D. J. MacKay and R. M. Neal, “Near shannon limit performance of low density parity check codes,” *Electronics letters*, vol. 33, no. 6, pp. 457–458, 1997.
- [9] J. Hou, P. H. Siegel, and L. B. Milstein, “Performance analysis and code optimization of low density parity-check codes on rayleigh fading channels,” *IEEE J. Sel. Areas Commun.*, vol. 19, no. 5, pp. 924–934, 2001.
- [10] I. B. Djordjevic, “On the irregular nonbinary QC-LDPC-coded hybrid multidimensional OSCD-modulation enabling beyond 100 Tb/s optical transport,” *J. Lightw. Technol.*, vol. 31, no. 16, pp. 2669–2675, 2013.

- 
- [11] H. Song, R. M. Todd, and J. Cruz, “Low density parity check codes for magnetic recording channels,” *IEEE Trans. Magn.*, vol. 36, no. 5, pp. 2183–2186, 2000.
- [12] G. Caire, G. Taricco, and E. Biglieri, “Bit-interleaved coded modulation,” *IEEE Trans. Inf. Theory*, vol. 44, no. 3, pp. 927–946, 1998.
- [13] A. Martinez, A. G. i Fabregas, G. Caire, and F. M. Willems, “Bit-interleaved coded modulation revisited: A mismatched decoding perspective,” *IEEE Trans. Inf. Theory*, vol. 55, no. 6, pp. 2756–2765, 2009.
- [14] G. Böcherer, F. Steiner, and P. Schulte, “Bandwidth efficient and rate-matched low-density parity-check coded modulation,” *IEEE Trans. Commun.*, vol. 63, no. 12, pp. 4651–4665, 2015.
- [15] P. Schulte and G. Böcherer, “Constant composition distribution matching,” *IEEE Trans. Inf. Theory*, vol. 62, no. 1, pp. 430–434, 2015.
- [16] J. J. Boutros, F. Jardel, and C. Méasson, “Probabilistic shaping and non-binary codes,” in *IEEE Int. Symp. Inf. Theory*, 2017, pp. 2308–2312.
- [17] A. K. Khandani and P. Kabal, “Shaping multidimensional signal spaces. I. Optimum shaping, shell mapping,” *IEEE Trans. Inf. Theory*, vol. 39, no. 6, pp. 1799–1808, 1993.
- [18] G. D. Forney, “Trellis shaping,” *IEEE Trans. Inf. Theory*, vol. 38, no. 2, pp. 281–300, 1992.
- [19] F. Buchali, G. Böcherer, W. Idler, L. Schmalen, P. Schulte, and F. Steiner, “Experimental demonstration of capacity increase and rate-adaptation by probabilistically shaped 64-QAM,” in *IEEE Eur. Conf. Opt. Commun.*, 2015, pp. 1–3.
- [20] G. Rezgui, A. Maaloui, I. Andriyanova, C. Poulliat, and C. Méasson, “NB-LDPC Codes with High Rates Achieving Low BER over the AWGN Channel with QAM Signaling,” in *IEEE Int. Symp. Inf. Theory Appl.*, 2020, pp. 235–239.
- [21] D. Declercq, M. Colas, and G. Gelle, “Regular GF  $(2q)$ -LDPC modulations for higher order qam-awgn channels,” in *Proc. Int. Symp. Inf. Theory Appl. (ISITA)*, 2004, pp. 1–6.

- [22] M. Arabaci, I. B. Djordjevic, R. Saunders, and R. M. Marcoccia, "Polarization-multiplexed rate-adaptive non-binary-quasi-cyclic-LDPC-coded multilevel modulation with coherent detection for optical transport networks," *Optics Express*, vol. 18, no. 3, pp. 1820–1832, 2010.
- [23] S. Kruglik, V. Potapova, and A. Frolov, "On performance of multilevel coding schemes based on non-binary ldpc codes," in *VDE Eur. Wireless Conf.*, 2018, pp. 1–4.
- [24] E. Zehavi, "8-psk trellis codes for a rayleigh channel," *IEEE Trans. Commun.*, vol. 40, no. 5, pp. 873–884, 1992.
- [25] U. Wachsmann, R. F. Fischer, and J. B. Huber, "Multilevel codes: Theoretical concepts and practical design rules," *IEEE Trans. Inf. Theory*, vol. 45, no. 5, pp. 1361–1391, 1999.
- [26] A. G. i Fabregas, A. Martinez, and G. Caire, *Bit-interleaved coded modulation*. Now Publishers Inc, 2008, vol. 5, no. 1-2.
- [27] N. Merhav, G. Kaplan, A. Lapidoth, and S. S. Shitz, "On information rates for mismatched decoders," *IEEE Trans. Inf. Theory*, vol. 40, no. 6, pp. 1953–1967, 1994.
- [28] A. Ganti, A. Lapidoth, and I. E. Telatar, "Mismatched decoding revisited: General alphabets, channels with memory, and the wide-band limit," *IEEE Trans. Inf. Theory*, vol. 46, no. 7, pp. 2315–2328, 2000.
- [29] S. Pfletschinger and D. Declercq, "Getting closer to mimo capacity with non-binary codes and spatial multiplexing," in *IEEE Global Telecommun. Conf.*, 2010, pp. 1–5.
- [30] E. Biglieri, G. Taricco, and E. Viterbo, "Bit-interleaved time-space codes for fading channels," in *Proc. Conf. Inform. Sci. Syst.*, 2000, pp. 15–17.
- [31] T. Liu and I. B. Djordjevic, "Multidimensional optimal signal constellation sets and symbol mappings for block-interleaved coded-modulation enabling ultrahigh-speed optical transport," *IEEE Photon. J.*, vol. 6, no. 4, pp. 1–14, 2014.
- [32] Z. Qu and I. B. Djordjevic, "Geometrically shaped 16QAM outperforming probabilistically shaped 16QAM," in *Eur. Conf. Opt. Commun.*, 2017, pp. 1–3.

- [33] G. D. Forney and L.-F. Wei, "Multidimensional constellations. I. introduction, figures of merit, and generalized cross constellations," *IEEE J. Sel. Areas Commun.*, vol. 7, no. 6, pp. 877–892, 1989.
- [34] H. G. Batshon, I. B. Djordjevic, L. Xu, and T. Wang, "Iterative polar quantization-based modulation to achieve channel capacity in ultrahigh-speed optical communication systems," *IEEE Photon. J.*, vol. 2, no. 4, pp. 593–599, 2010.
- [35] S. Zhang, F. Yaman, E. Mateo, T. Inoue, K. Nakamura, and Y. Inada, "A generalized pairwise optimization for designing multi-dimensional modulation formats," in *IEEE Opt. Fiber Commun. Conf. Exhibition*, 2017, pp. 1–3.
- [36] J. Karout, R.-J. Essiambre, E. Agrell, and A. Tulino, "Achievable rates of multidimensional multisphere distributions," in *2017 Optical Fiber Communications Conference and Exhibition (OFC)*. IEEE, 2017, pp. 1–3.
- [37] F.-W. Sun and H. C. Van Tilborg, "Approaching capacity by equiprobable signaling on the Gaussian channel," *IEEE Trans. Inf. Theory*, vol. 39, no. 5, pp. 1714–1716, 1993.
- [38] M. F. Barsoum, C. Jones, and M. Fitz, "Constellation design via capacity maximization," in *IEEE Int. Symp. Inf. Theory*, 2007, pp. 1821–1825.
- [39] J. Zöllner and N. Loghin, "Optimization of high-order non-uniform qam constellations," in *IEEE Int. Symp. Broadband Multimedia Syst. Broadcast.*, 2013, pp. 1–6.
- [40] F. Kayhan and G. Montorsi, "Constellation design for transmission over nonlinear satellite channels," in *IEEE Glob. Commun. Conf.*, 2012, pp. 3401–3406.
- [41] A. R. Calderbank and L. H. Ozarow, "Nonequiprobable signaling on the Gaussian channel," *IEEE Trans. Inf. Theory*, vol. 36, no. 4, pp. 726–740, 1990.
- [42] F. R. Kschischang and S. Pasupathy, "Optimal nonuniform signaling for Gaussian channels," *IEEE Trans. Inf. Theory*, vol. 39, no. 3, pp. 913–929, 1993.
- [43] R. G. Gallager, *Information theory and reliable communication*. Springer, 1968, vol. 588.

- 
- [44] R. Blahut, "Computation of channel capacity and rate-distortion functions," *IEEE Trans. Inf. Theory*, vol. 18, no. 4, pp. 460–473, 1972.
- [45] J. Huang and S. P. Meyn, "Characterization and computation of optimal distributions for channel coding," *IEEE Trans. Inf. Theory*, vol. 51, no. 7, pp. 2336–2351, 2005.
- [46] T. J. Richardson and R. L. Urbanke, "The capacity of low-density parity-check codes under message-passing decoding," *IEEE Trans. Inf. Theory*, vol. 47, no. 2, pp. 599–618, 2001.
- [47] M. C. Davey and D. J. MacKay, "Low density parity check codes over GF (q)," in *IEEE Inf. Theory Workshop (Cat. No. 98EX131)*, 1998, pp. 70–71.
- [48] X.-Y. Hu, E. Eleftheriou, and D.-M. Arnold, "Regular and irregular progressive edge-growth tanner graphs," *IEEE Trans. Inf. Theory*, vol. 51, no. 1, pp. 386–398, 2005.
- [49] C. Poulliat, "Contributions à l'étude et à l'optimisation de systèmes à composantes itératives." Ph.D. dissertation, Université de Cergy Pontoise, 2010.
- [50] A. Bennatan and D. Burshtein, "Design and analysis of nonbinary LDPC codes for arbitrary discrete-memoryless channels," *IEEE Trans. Inf. Theory*, vol. 52, no. 2, pp. 549–583, 2006.
- [51] D. Declercq and M. Fossorier, "Decoding algorithms for nonbinary ldpc codes over  $gf(q)$ ," *IEEE Trans. Commun.*, vol. 55, no. 4, pp. 633–643, 2007.
- [52] A. Voicila, D. Declercq, F. Verdier, M. Fossorier, and P. Urard, "Low-complexity decoding for non-binary ldpc codes in high order fields," *IEEE Trans. Commun.*, vol. 58, no. 5, pp. 1365–1375, 2010.
- [53] J. Thorpe, "Low-density parity-check (LDPC) codes constructed from protographs," *IPN progress report*, vol. 42, no. 154, pp. 42–154, 2003.
- [54] G. Liva, S. Song, L. Lan, Y. Zhang, S. Lin, and W. E. Ryan, "Design of LDPC codes: A survey and new results," *J. Commun. Softw. Syst.*, vol. 2, no. 3, pp. 191–211, 2006.
- [55] L. Dolecek, D. Divsalar, Y. Sun, and B. Amiri, "Non-binary protograph-based LDPC codes: Enumerators, analysis, and designs," *IEEE Trans. Inf. Theory*, vol. 60, no. 7, pp. 3913–3941, 2014.

- [56] S. Ten Brink, "Convergence behavior of iteratively decoded parallel concatenated codes," *IEEE Trans. Commun.*, vol. 49, no. 10, pp. 1727–1737, 2001.
- [57] S. Ten Brink, G. Kramer, and A. Ashikhmin, "Design of low-density parity-check codes for modulation and detection," *IEEE Trans. Commun.*, vol. 52, no. 4, pp. 670–678, 2004.
- [58] B.-Y. Chang, L. Dolecek, and D. Divsalar, "EXIT chart analysis and design of non-binary protograph-based LDPC codes," in *Mil. Commun. Conf.* IEEE, 2011, pp. 566–571.
- [59] S. Ten Brink, "Design of serially concatenated codes based on iterative decoding convergence," in *2nd Int. Symp. Turbo Codes and Related Topics*. Citeseer, 2000.
- [60] M. Tuchler, R. Koetter, and A. C. Singer, "Turbo equalization: principles and new results," *IEEE Trans. Commun.*, vol. 50, no. 5, pp. 754–767, 2002.
- [61] C. Hermosilla and L. Szczecinski, "Exit charts for turbo receivers in mimo systems," in *IEEE Int. Symp. Signal Process. Appl.*, vol. 1, 2003, pp. 209–212.
- [62] H. Chen and A. Haimovich, "Exit charts for turbo trellis-coded modulation," *IEEE Commun. Lett.*, vol. 8, no. 11, pp. 668–670, 2004.
- [63] G. Liva and M. Chiani, "Protograph ldpc codes design based on exit analysis," in *IEEE Glob. Telecommun. Conf.*, 2007, pp. 3250–3254.
- [64] P. K. Vitthaladevuni and M.-S. Alouini, "A recursive algorithm for the exact BER computation of generalized hierarchical QAM constellations," *IEEE Trans. Inf. Theory*, vol. 49, no. 1, pp. 297–307, 2003.
- [65] Q. Li, J. Zhang, L. Bai, and J. Choi, "Performance analysis and system design for hierarchical modulated bicm-id," *IEEE Trans. Wireless Commun.*, vol. 13, no. 6, pp. 3056–3069, 2014.
- [66] R. Mears, L. Reekie, I. Jauncey, and D. N. PAYNE, "High-gain rare-earth-doped fiber amplifier at 1.54  $\mu\text{m}$ ," in *Opt. Fiber Commun. Conf.* Optical Society of America, 1987, p. WI2.
- [67] R. A. Linke and A. H. Gnauck, "High-capacity coherent lightwave systems," *J. Lightw. Technol.*, vol. 6, no. 11, pp. 1750–1769, 1988.

- [68] K. Kikuchi, “Coherent optical communication systems,” *Opt. Fiber Telecommun. VB*, pp. 95–129, 2008.
- [69] G. Charlet, “Coherent detection associated with digital signal processing for fiber optics communication,” *Comptes Rendus Physique*, vol. 9, no. 9-10, pp. 1012–1030, 2008.
- [70] H.-M. Chin, D. Charlton, A. Borowiec, M. Reimer, C. Laperle, M. O’Sullivan, and S. J. Savory, “Probabilistic design of optical transmission systems,” *J. Lightw. Technol.*, vol. 35, no. 4, pp. 931–940, 2016.
- [71] A. Dumenil, E. Awwad, and C. Méasson, “Low-complexity polarization coding for PDL-resilience,” in *IEEE Eur. Conf. Opt. Commun.*, 2018, pp. 1–3.
- [72] A. Dumenil, E. Awwad, and C. Measson, “Rate optimization using SO (4) transforms for PDL mitigation,” in *Eur. Conf. Opt. Commun. IET*, 2019, pp. 1–4.
- [73] M. Karlsson, “Four-dimensional rotations in coherent optical communications,” *J. Lightw. Technol.*, vol. 32, no. 6, pp. 1246–1257, 2014.
- [74] T. A. Eriksson, T. Fehenberger, P. A. Andrekson, M. Karlsson, N. Hanik, and E. Agrell, “Impact of 4d channel distribution on the achievable rates in coherent optical communication experiments,” *J. Lightw. Technol.*, vol. 34, no. 9, pp. 2256–2266, 2016.
- [75] J. Hou, P. H. Siegel, L. B. Milstein, and H. D. Pfister, “Capacity-approaching bandwidth-efficient coded modulation schemes based on low-density parity-check codes,” *IEEE Trans. Inf. Theory*, vol. 49, no. 9, pp. 2141–2155, 2003.
- [76] G. Forney, R. Gallager, G. Lang, F. Longstaff, and S. Qureshi, “Efficient modulation for band-limited channels,” *IEEE J. Sel. Areas Commun.*, vol. 2, no. 5, pp. 632–647, 1984.
- [77] N. Palgy and R. Zamir, “Dithered probabilistic shaping,” in *IEEE Convent. Electr. Electron. Engineers*, 2012, pp. 1–5.
- [78] G. Kramer, “Probabilistic amplitude shaping applied to fiber-optic communication systems,” in *Proc. Int. Symp. on Turbo Codes and Iterative Inf. Proc.*, 2016.
- [79] M. P. Yankov, D. Zibar, K. J. Larsen, L. P. Christensen, and S. Forchhammer, “Constellation shaping for fiber-optic channels with QAM and

- high spectral efficiency,” *IEEE Photon. Technol. Lett.*, vol. 26, no. 23, pp. 2407–2410, 2014.
- [80] L. Beygi, E. Agrell, J. M. Kahn, and M. Karlsson, “Rate-adaptive coded modulation for fiber-optic communications,” *J. Lightw. Technol.*, vol. 32, no. 2, pp. 333–343, 2013.
- [81] T. Fehenberger, G. Böcherer, A. Alvarado, and N. Hanik, “Ldpc coded modulation with probabilistic shaping for optical fiber systems,” in *Optical Fiber Communication Conference*. Optica Publishing Group, 2015, pp. Th2A–23.
- [82] A. Ghazisaeidi *et al.*, “65Tb/s transoceanic transmission using probabilistically-shaped PDM-64QAM,” in *VDE Eur. Conf. Opt. Commun.*, 2016, pp. 1–3.
- [83] S. Chandrasekhar, B. Li, J. Cho, X. Chen, E. Burrows, G. Raybon, and P. Winzer, “High-spectral-efficiency transmission of PDM 256-QAM with parallel probabilistic shaping at record rate-reach trade-offs,” in *Eur. Conf. Opt. Commun.* VDE, 2016, pp. 1–3.
- [84] S. Zhang *et al.*, “Capacity-approaching transmission over 6375 km at spectral efficiency of 8.3 bit/s/Hz,” in *Opt. Fiber Commun. Conf.* Optical Society of America, 2016, pp. Th5C–2.
- [85] Q. Hu, F. Buchali, L. Schmalen, and H. Buelow, “Experimental demonstration of probabilistically shaped QAM,” in *Signal Process. Photon. Commun.* Optica Publishing Group, 2017, pp. SpM2F–6.
- [86] L. Schmalen, A. Alvarado, and R. Rios-Müller, “Performance prediction of nonbinary forward error correction in optical transmission experiments,” *J. Lightw. Technol.*, vol. 35, no. 4, pp. 1015–1027, 2017.
- [87] G. Liga, A. Alvarado, E. Agrell, and P. Bayvel, “Information rates of next-generation long-haul optical fiber systems using coded modulation,” *J. Lightw. Technol.*, vol. 35, no. 1, pp. 113–123, 2017.
- [88] T. Fehenberger, A. Alvarado, G. Böcherer, and N. Hanik, “On probabilistic shaping of quadrature amplitude modulation for the nonlinear fiber channel,” *J. Lightw. Technol.*, vol. 34, no. 21, pp. 5063–5073, 2016.
- [89] G. Tzimpragos *et al.*, “A survey on FEC codes for 100 G and beyond optical networks,” *IEEE Commun. Surveys Tuts.*, vol. 18, no. 1, pp. 209–221, 2014.

- 
- [90] A. Bennatan and D. Burshtein, “On the application of LDPC codes to arbitrary discrete-memoryless channels,” *IEEE Trans. Inf. Theory*, vol. 50, no. 3, pp. 417–438, 2004.
- [91] Y. Fang, G. Bi, Y. L. Guan, and F. C. Lau, “A survey on protograph LDPC codes and their applications,” *IEEE Commun. Surveys Tuts.*, vol. 17, no. 4, pp. 1989–2016, 2015.
- [92] E. ETSI, “Digital video broadcasting (dvb); second generation framing structure, channel coding and modulation systems for broadcasting, interactive services, news gathering and other broadband satellite applications,” *Part II: S2-Extensions (DVB-S2X)*, pp. 22–27, 2005.
- [93] E. Pisek, D. Rajan, S. Abu-Surra, and J. R. Cleveland, “Capacity-approaching TQC-LDPC convolutional codes enabling power-efficient decoders,” *IEEE Trans. Commun.*, vol. 65, no. 1, pp. 1–13, 2016.
- [94] R. Laroia, N. Farvardin, and S. A. Tretter, “On optimal shaping of multi-dimensional constellations,” *IEEE Trans. Inf. Theory*, vol. 40, no. 4, pp. 1044–1056, 1994.
- [95] H. Méric, “Approaching the Gaussian channel capacity with APSK constellations,” *IEEE Commun. Lett.*, vol. 19, no. 7, pp. 1125–1128, 2015.
- [96] J. J. Boutros, U. Erez, J. Van Wousterghem, G. I. Shamir, and G. Zémor, “Geometric shaping: low-density coding of Gaussian-like constellations,” in *IEEE Inf. Theory Workshop*, 2018, pp. 1–5.
- [97] Z. Wang, A. Patapoutian, R. C. Venkataramani, and G. I. Shamir, “Universal modulation coding for a data channel,” Mar. 10 2015, US Patent 8,976,474.
- [98] F. Jardel, T. A. Eriksson, C. Méasson, A. Ghazisaeidi, F. Buchali, W. Idler, and J. J. Boutros, “Exploring and experimenting with shaping designs for next-generation optical communications,” *J. Lightw. Technol.*, vol. 36, no. 22, pp. 5298–5308, 2018.
- [99] J. Van Wousterghem, J. J. Boutros, and M. Moeneclaey, “Construction of Circular Quadrature Amplitude Modulations (CQAM),” in *IEEE Int. Conf. Sci. Electr. Eng.*, 2018, pp. 1–5.
- [100] G. Böcherer and R. Mathar, “Matching dyadic distributions to channels,” in *IEEE Data Compres. Conf.*, 2011, pp. 23–32.

- 
- [101] T. Fehenberger, D. S. Millar, T. Koike-Akino, K. Kojima, and K. Parsons, “Multiset-partition distribution matching,” *IEEE Trans. Commun.*, vol. 67, no. 3, pp. 1885–1893, 2018.
- [102] G. Böcherer, P. Schulte, and F. Steiner, “High throughput probabilistic shaping with product distribution matching,” *arXiv preprint arXiv:1702.07510*, 2017.
- [103] T. Fehenberger, D. S. Millar, T. Koike-Akino, K. Kojima, and K. Parsons, “Parallel-amplitude architecture and subset ranking for fast distribution matching,” *IEEE Trans. Commun.*, vol. 68, no. 4, pp. 1981–1990, 2020.
- [104] A. Maalaoui, C. Poulliat, and I. Andriyanova, “Geometric versus Probabilistic Shaping for Circular-QAM with Nonbinary LDPC Codes,” in *IEEE Int.Symp. Inf. Theory*, 2022, pp. 396–401.
- [105] Y. C. Gültekin, W. J. van Houtum, A. G. Koppelaar, F. M. Willems, J. Wim *et al.*, “Enumerative sphere shaping for wireless communications with short packets,” *IEEE Trans. Wireless Commun.*, vol. 19, no. 2, pp. 1098–1112, 2019.